Tampere University

DUC LE

Advances in Antennas and High-Frequency Material Characterization for Wireless Body-Area Networks

Tampere University Dissertations 569

Tampere University Dissertations 569

DUC LE

Advances in Antennas and High-Frequency Material Characterization for Wireless Body-Area Networks

ACADEMIC DISSERTATION
To be presented, with the permission of
the Faculty of Medicine and Health Technology
of Tampere University,
for online public discussion
on 18th of March, 2022, at 12 o'clock.

ACADEMIC DISSERTATION
Tampere University, Faculty of Medicine and Health Technology
Finland

Responsible supervisor and Custos	Professor Leena Ukkonen Tampere University Finland	
Supervisor	University Lecturer Toni Björninen Tampere University Finland	
Pre-examiners	Associate Professor (Tenure Track) Ping Jack Soh University of Oulu Finland	Professor Sima Noghanian University of Manitoba Canada
Opponent	Associate Professor Paolo Nepa University of Pisa Italy	

Cover design: Roihu Inc.

ISBN 978-952-03-2328-8 (print)
ISBN 978-952-03-2329-5 (pdf)
ISSN 2489-9860 (print)
ISSN 2490-0028 (pdf)
http://urn.fi/URN:ISBN:978-952-03-2329-5

PunaMusta Oy – Yliopistopaino
Joensuu 2022

ACKNOWLEDGMENTS

This research work has been conducted in WISE Lab (Wireless Identification and Sensing Systems Lab) at Tampere University. This worked is funded by Academy of Finland, in part by HPY Research Foundation of Elisa and in part by Nokia Foundation Grant. The financial support is gratefully acknowledgement.

I wish to express my deepest gratitude to my supervisor Dr. Toni Björninen and Professor Leena Ukkonen for their guidance, encouragement and excellent provision of the research facilities during my studies. My sincerest appreciation goes also to Professor Lauri Sydänheimo for the enlightening and inspiring discussion. My sincere gratitude goes to Dr. Roy B. V. B. Simorangkir and Dr. Abu Sadat Md. Sayem for persistent guidance and excellent collaboration in the Optically Transparent Flexible Robust Circularly Polarized Antenna research. Thanks also go to Dr, Yari Kangas for the inspiring lectures on antennas, passive circuits and electromagnetic model.

During my doctoral study, I am indebted also to numerous colleagues for their support, co-operation and contributions. Special thank are reserved to Shahbaz Admed for collaboration in the research on forearm antenna based quasi-Yagi configuration and wearable circular polarization antenna research. I wish to thanks Shubin Ma for the guidance of using equipment at the lab for the circular polarization RFID tag antenna measurement and your ideas for the wearable antennas. For the support in the material characterization, I wish to thank Nikta Pournoori for her support and collaboration. I would like to extend my gratitude to the whole WISE lab member for pleasant atmosphere working environment.

Most of all I would like to express my deepest gratitude to my family's members for their unconditional love and best wish and endless support. I also wish to thank my friends for all the moments spent together which have been essential counterweight for the research work.

Tampere, February 2022

Duc Le

ABSTRACT

The development of the personal body-centric communication system is an essential part of the novel generation of wireless communication systems and one of the communication technology challenges. The versatility of body-centric communication revolutionizes healthcare by allowing continuous and in-all-conditions human health monitoring and human-centered authentication. Recently, with the extra-low power consumption and low-complexity backscatter communications, the passive ultra-high-frequency (UHF) radio-frequency identification (RFID) technology has been considered a promising approach for the wireless body area network.

An inevitable part of this system is the wearable antenna, which plays a critical role in ensuring the efficient wireless link of the signal in the presence of the wearer. The wearable antenna should be fabricated with textile materials and equipped with various radiation configurations to enhance robustness and the operation's versatility for long-term use. The difficulty of the wearable antenna development is to obtain the property information of the unknown textile substrate and conductor. To address the above-mentioned challenges, this thesis starts with the novel textile material characterization method to single out the relative permittivity and loss tangent of the substrate and bulk conductivity of the conductor. Unlike conventional approaches, our method simply applied the testing structure of the microstrip line composed of the textile material and simple data processing with the least square estimation. Then, a variation of the textile wearable antenna development with a low-profile planar in geometry is proposed in the next part of the thesis. The headgear RFID tag and forearm RFID reader antennas were developed based on quasi-Yagi configurations and periodic surface to obtain a directive pattern along the body surface. Another type of antenna configuration developed in this thesis is the circular polarization patch antenna for the wearable RFID tag. This type of antenna significantly reduced the polarization mismatch between the reader and the tag; hence, the detection capability and radiation efficiency are remarkably upgraded. The promising performance of the antennas was rigorously analyzed in simulation and verified with on-body measurement.

CONTENTS

ABBREVIATIONS

AMC	Artificial Magnetic Conductors
AR	Axial Ratio
CCW	Counterclockwise
CP	Circular Polarization
CW	Clockwise
EBG	Electromagnetic Bandgap
EM	Electromagnetic
EMC	Electromagnetic Compatibility
EPDM	Ethylene Propylene Diene Monomer
FSS	Frequency Selective Surfaces
HFSS	High Frequency Structure Simulator
LCP	Liquid Crystal Polymer
LHCP	Left-Hand Circular Polarization
MRI	Magnetic Resonance Imaging
PIFA	Planar Inverted-F Antenna
RF	Radio Frequency
RFID	Radio Frequency Identification
RHCP	Right-Hand Circular Polarization
SAR	Specific Absorption Rate
SIW	Substrate Integrated Waveguide
SWA	Surface Wave Antenna
SWA	Surface Wave Antennas
TEM	Transverse Electromagnetic
UHF	Ultra High Frequency
WBAN	Wireless Body Area Network

ORIGINAL PUBLICATIONS

Publication I Duc Le, Ye Kuang, L. Ukkonen, T. Björninen, "Microstrip transmission line model fitting approach for characterization of textile materials as dielectrics and conductors for wearable electronics," *The International Journal of Numerical Modelling: Electronic Networks, Devices and Fields*, vol. 32, no. 6, p. 2582, Feb. 2019.

Publication II Duc Le, L. Ukkonen, T. Björninen, "Dual-ID headgear UHF RFID tag with broadside and end-fire patterns based on quasi-Yagi antenna," *Proc. IEEE Asia-Pacific Microwave Conference*, pp. 10–13, Singapore, Dec. 2019.

Publication III Duc Le, L. Ukkonen, T. Björninen, "A Dual-ID RFID tag for headgear based on quasi-Yagi and dipole antenna," *IEEE Antennas Wireless Propag. Lett*., vol. 19, no. 8, pp. 1321–1325, Jun. 2020.

Publication IV S. Ahmed, Duc Le, L. Sydänheimo, L. Ukkonen, T. Björninen, "Wearable metasurface-enabled quasi-Yagi antenna for UHF RFID reader with end-fire radiation along the forearm," *IEEE Access*, 6 pages, vol. 9, pp. 77229–77238, 2021.

Publication V Duc Le, L. Ukkonen, T. Björninen, "Circularly polarized corner-truncated and slotted microstrip patch antenna on textile substrate for wearable passive UHF RFID tags," *European Conference on Antennas and Propagation*, pp. 15–20, Copenhagen, Denmark, Mar. 2020.

Publication VI D. Le, A. Shahbaz, T. Björninen, L. Ukkonen, T. Björninen, "A small all-corners-truncated circularly polarized microstrip patch antenna on textile substrate for wearable passive UHF RFID tags," *IEEE Journal of Radio Frequency Identification,* pp. 106–112, vol. 5, no. 2, Apr. 2021.

AUTHOR CONTRIBUTIONS

Publication I Duc Le conducted and simulated the testing samples for the material characterization method. Duc Le, Ye Kuang, and T. Björninen wrote the manuscript. Co-authors reviewed the text and provided feedback.

Publication II Duc Le conducted the simulation. Duc Le and T. Björninen evaluated the results. Duc Le wrote the manuscript with the consultant from T. Björninen and L. Ukkonen.

Publication III Duc Le conducted the simulation and experiment. Duc Le wrote the manuscript. The rest of the authors reviewed the text and provided feedback.

Publication IV S. Ahmed and Duc Le conducted the simulation and measurement of the antenna and wrote the manuscript. L. Ukkonen and T. Björninen reviewed the text and provided feedback.

Publication V Duc Le conducted the antenna simulations and measurements. Duc Le and T. Björninen analyzed the results. Duc Le and T. Björninen wrote the manuscript.

Publication VI Duc Le developed the antenna and implanted the measurement together with A. Shahbaz. D. Le wrote the manuscript. T. Björninen supervised the research. All authors reviewed the text.

1 INTRODUCTION

1.1 Wearable Antennas in WBANs

The technological advancement in wireless communication devices has progressed in the modern healthcare system [1]–[4]. As a powerful tool for healthcare and medicine, wireless body area networks (WBANs) have been used in real-time medical applications to improve the quality of life. By enabling wireless continuous biofeedback data [5][6], WBANs allow the wireless monitoring of the physiological signals of a large number of patients via embedded sensor networks. These body-centric systems offer a great deal of potential through the medical treatment's combination of time savings, inconspicuous integration, and enhancement of the user's experience while still being comfortable for long-term use. In these systems, the wearable antennas have been considered as an irreplaceable section in the reliable transmission and reception of the radio signals within the wearable body area networks [7][8]. However, the comprehensive everyday deployment of wearable antennas requires addressing several design issues. These antennas operate close to the surface of the human body, which is a harsh environment introducing, e.g., stretching, twisting, and bending [9][10]. Therefore, the antenna should be small, low-profile, lightweight, flexible, unobtrusive, and compatible with textile manufacturing for wireless wearable devices. Additionally, the wearable antennas should provide advanced functionalities such as multiple radiations, coupling mechanisms, and reconfigurability to operate at various frequency bands, such as MedRadio at 401–406 MHz, the worldwide ISM bands centered at 2.45 GHz and 5.8 GHz, GPS at 1575.42 MHz, and UHF RFID bands at 866 MHz and 915 MHz.

Additionally, retaining low levels of specific absorption rate (SAR) and acceptable antenna radiation characteristics is challenging. Furthermore, the impact of unexpected interaction of the body, which is considered lossy tissue, on the radiation efficiency is also critical. To deal with that issue, the multilayer antenna containing the ground plane and the periodic surface between the antenna and the body surface have garnered a tremendous amount of interest in both academia and industry.

1.2 Scope and Objective of the Thesis

One of the significant challenges in developing the wearable body area networks is generating an efficient and reliable wireless communication link with the textile

wearable antennas unobtrusively integrated into the clothing without disturbing the wearer's movement. The efficient antenna development requires precise information on the electromagnetic properties of all materials the antenna composed of. However, in contrast to the conventional antenna design with the high-frequency laminates, the electromagnetic characteristics of the textile materials, such as relative permittivity and loss tangent of textile substrates and conductivity of the conductor, are not readily available, and their values are less homogeneous. Besides, the versatile passive ultra-high frequency radio-frequency identification technology (UHF RFID) has been optimized for wireless body area systems and utilized for the wireless health application [11]–[21]. With extra-low power consumption and low-complexity backscatter communications, the wearable RFID tags and readers with flexible and lightweight antennas have been gaining more attention in recent years for identification and sensing of the functionalities [22]–[25].

For the first objective of this thesis, we propose a reliable characterization method for the textile substrate and conductor based on the model fitting of the transmission line in the range of frequency from 0.2 GHz to 3 GHz [Publication I]. Our methodology extracted the material RF properties from the best fit data based on the least square estimation sense. Our approach also combines the simplification of the testing structures and ease of the data processing; hence, it is applicable for wearable antenna development with textile materials.

Another major target of this thesis is to develop versatile, robust, and efficient antenna structures for wireless health with state-of-the-art RFID-based antenna technologies. The far-field UHF RFID is chosen as the target system to develop antennas for off-body applications since these balances the operating distance, antenna footprint, and tissue impact on the antenna radiation. As an advancement, we equip multifunction features with multilayer-based structures. All of the proposed antennas are developed with planar geometry; hence, most of them can be integrated into textile materials. There are three novel approaches for the antennas:

1. A dual-ID RFID tag based on wearable quasi-Yagi and dipole antenna headgear is developed with the periodic surface to mitigate the coupling of antenna and body tissue [Publication II] [Publication III]. With an end-fire beam from the quasi-Yagi antenna configuration, the RFID tag can transmit the identification data to the reader in front of the user's head. We also reuse the reflector as the dipole that provides a broadside pattern of the wearer's head.

2. The far-field RFID reader antenna is optimized to attach to the forearm with a directive radiation pattern with a high realized gain [Publication IV]. Furthermore, thanks to the quasi-Yagi antenna configuration, the reader antenna easily detects the tags by pointing the user's hand toward them.
3. The circular polarization tag antenna with a compact size and high read range for wearable application is proposed in Publications [V] and [VI]. With the CP configuration, the antenna can upgrade the polarization efficiency, and thereby, the peak detection range is improved.

2 REVIEW OF THE LITERATURE

In the wireless communication system, the antenna is responsible for transmitting and receiving the electromagnetic waves. The first experiment about the transmission of the electromagnetic wave between two antennas was conducted by Heinrich Hertz in 1888 [27]. The form of the antenna has been dramatically developed to multiple configurations from the conventional antenna, like monopoles, loop, and patch, to the recent watch-type chip antenna [28]. Modern antennas are also equipped with unique radiation properties, including multi-band and wideband, directive radiation pattern, wearable, implantable circular polarization, reconfigurability, and omnidirectional radiation pattern.

This section outlines the antenna fundamentals, wearable antenna, and operation principle of the passive far-field UHF RFID system. First, in the antenna fundamentals, we overview the basic antenna radiation properties, such as input impedance, antenna radiation, and antenna polarization. Next, the multilayer wearable antennas, e-textile antennas, metasurface-enabled antennas, and surface wave antennas are discussed in the wearable antenna section. Then, some of the latest textile material characterization is briefly introduced in the next section. The last section focuses on the fundamentals of the RFID communication system.

2.1 Antenna Fundamentals

Impedance matching

The impedance of an antenna is defined as the voltage-to-current ratio the antenna presents at its input terminal [29]. The structure and materials of the antenna and its surroundings determine the input impedance. Its real part depends on the dissipation of electromagnetic energy within the antenna, its near-field region, and the total amount of energy leaving the antenna as radiation.

The imaginary part is determined by the reactive near-field interaction between the antenna and its surroundings. Thus, the antenna impedance is a frequency-dependent quantity that is also strongly influenced by the operating environment of the antenna.

In a wireless communications system, the antenna is always interfaced with other modules. The impedances at both sides of the interface determine how efficient power is transferred across it. According to the principle of complex conjugate impedance matching, the power transfer is maximized when the two impedances are complex conjugates of each other [29]. Considering the wireless communications system as the source, with the impedance of Z_S and the antenna with the impedance of Z_A connected to it as a load, the power transfer efficiency across the interfaces is given by [29]

$$\tau = \frac{4\mathrm{Re}(Z_S)\mathrm{Re}(Z_A)}{|Z_S + Z_A|^2}. \quad (2.1)$$

The unique maximum of τ is $\tau = 1$, which is achieved under the complex conjugate matching condition: $\mathrm{Re}(Z_A) = \mathrm{Re}(Z_S)$ and $\mathrm{Im}(Z_A) = -\mathrm{Im}(Z_S)$. Because equation 2.1 is symmetric relative to Z_S and Z_A, it is also true when the antenna is considered a source that delivers power to the wireless communications system, as expected from the circuit analysis principles. Moreover, the equation applies to any circuit interface and not only when it involves an antenna.

Antenna radiation

The antenna radiation regions can be divided into two main areas, namely near field and far field. The near-field region is categorized as a reactive and radiating field region according to the distance and operating frequency of the antenna, as shown in Figure 1. At the reactive near-field region, the electric and magnetic fields are out of phase by 90^0 which causes the domination of the reactive effect. The radius of the reactive region is approximated as [29]

$$R_1 < 0.62\sqrt{\frac{D^3}{\lambda}}, \quad (2.2)$$

where D is the maximum antenna dimension (m), and λ is the wavelength (m).

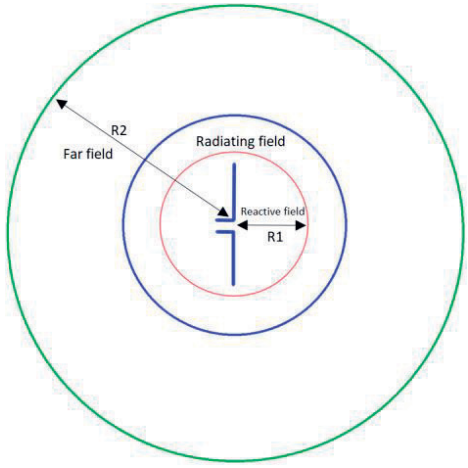

Figure 1. Antenna field regions.

The radiated effect dominates the radiating field region between the reactive and far-field regions. Lastly, the far-field area is far from the antenna, where the magnetic and electric fields are in phase. The radius of the far-field region is approximated as

$$R_2 = \frac{2D^2}{\lambda}. \quad (2.3)$$

The radiated fields are observed at a spherical coordinate system (θ, φ, ρ) and the corresponding Cartesian coordinates (x, y, z). It is supposed that the antenna is set up in the Cartesian coordinates (x, y, z) with volume V. The time-harmonic antenna current density **J** is represented in another Cartesian coordinate system (x, y, z), and the time-harmonic antenna current density **J** is expressed in the Cartesian coordinate system (u, v, w). Then, the normalized antenna power pattern $F(\theta, \varphi)$ on a spherical shell around the antenna is illustrated with [30]

$$\mathrm{F}(\theta, \varphi) = \frac{|Q(\theta,\varphi)|^2}{max|Q(\theta,\varphi)|^2}, \tag{2.4}$$

where $$|Q(\theta, \varphi)| = \int_v \mathbf{J}(u, v, w) e^{j\frac{2\pi f}{c} v(\theta,\varphi)}\, du\, dv\, dw, \tag{2.5}$$

and $$(x-u)^2 + (y-v)^2 + (z-w)^2 = \underset{(u,v,w)\in V}{Max}(u^2 + v^2 + w^2). \tag{2.6}$$

The antenna directivity $D(\theta, \varphi)$ is defined as the power density ratio at one specific direction to the radiated power density over the whole radiation pattern of an antenna. The following equation is the well-known expression of directivity [30],

$$\mathrm{D}(\theta, \varphi) = \frac{\mathrm{F}(\theta,\varphi)}{\frac{1}{4\pi}\int_0^{2\pi}\int_0^{\pi} \mathrm{F}(\theta,\varphi)\sin\theta d\theta d\phi}. \tag{2.7}$$

Another parameter to evaluate the functional performance of the antenna is the radiation efficiency (e_{rad}). This parameter shows the ratio of the accepted power by antenna (P_{acc}) and the radiated power by antenna (P_{rad}).

$$e_{rad} = \frac{\mathrm{P}_{rad}}{\mathrm{P}_{acc}};\ \mathrm{P}_{rad} = \frac{\eta}{8\lambda^2}\int_0^{2\pi}\int_0^{\pi} |\mathrm{Q}(\theta, \varphi)|^2 \sin\theta d\theta d\phi. \tag{2.8}$$

It is noted that the e_{rad} in equation (2.8) omitted the unexpected impacts of the possible impedance mismatch between the antenna and the generator. The gain of antenna $\mathrm{G}(\theta, \varphi)$ is equal to the results of directivity $\mathrm{D}(\theta, \varphi)$ multiplied by radiation efficiency e_{rad}.

$$\mathrm{G}(\theta, \varphi) = e_{rad}\mathrm{D}(\theta, \varphi) \tag{2.9}$$

The realized gain G_R is the gain of the antenna taking the loss due to an impedance mismatch between the antenna and the source. The antenna's realized gain is given by

$$G_R = G(1 - |s_{11}|^2), \tag{2.10}$$

where G and s_{11} are the simulated gain and reflection coefficient of the antenna.

The antenna's polarization is defined as the polarization of the transmitted waves in the direction of the radiated electric fields from the antenna.

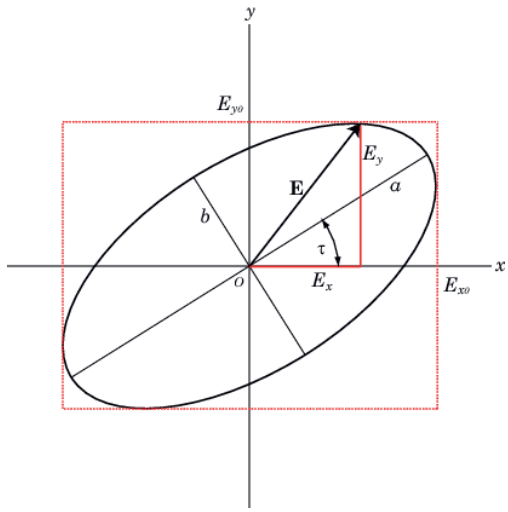

Figure 2. Polarization ellipse.

The electric field propagating along the z-axis can be described as the vector sum of two orthogonal components, vertical and horizontal and components expressed as

$$\mathrm{E} = E_x\hat{x} + E_y\hat{y} \tag{2.11}$$

We can rewrite them as

$$\mathrm{E} = E_x(\hat{x} + \hat{\rho}_L\hat{y}) \text{ , } \hat{\rho}_L = \frac{E_y}{E_x} \tag{2.12}$$

When the electric field is viewed along the propagation direction, as shown in Figure 2, the tip of the electric field vector traces out an ellipse with the electric field vector rotating clockwise (CW) or counterclockwise (CCW). In Figure 2, τ is the tilt of the polarization ellipse measured from the x-axis to the maximum power of the E-field. The axial ratio (AR) is the ratio of the major and minor semiaxes of the ellipse. The circular polarization is the special case where the semiaxes are equal, i.e. the polarization ellipse reduces to a circle. In this case, CW rotation of the electric field vector corresponds with the left-hand circular polarization (LHCP) and CCW with right-hand circular polarization (RHCP) as indicated in Figure 3.

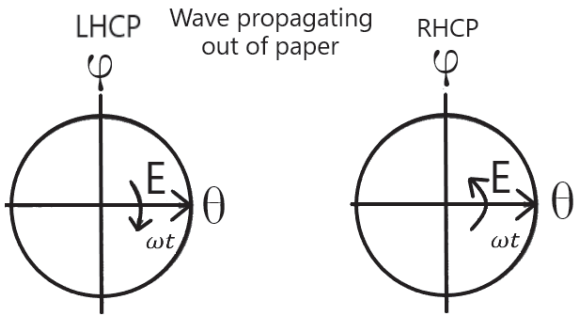

Figure 3. Handedness of the circular polarization.

Finally, the antenna is linearly polarized when the polarization ellipse approaches a line, i.e. when the major semiaxis is much larger than the minor semiaxis.

Analogous to equations (2.11) and (2.12), the electric field vector of the EM wave can also be given as a combination of the left and right hand circularly polarized components E_L and E_R as

$$\mathrm{E} = E_L + E_R. \tag{2.13}$$

It can be rewritten as

$$\mathrm{E} = E_L + \gamma E; \quad \gamma = \frac{E_R}{E_L}, \tag{2.14}$$

where γ is the circular polarization ratio. The relationship between the axial ratio and polarization components can be expressed as

$$AR = \begin{cases} \frac{E_{max}}{E_{min}} = \frac{|E_L|+|E_R|}{|E_L|-|E_R|} = \frac{1+|\gamma|}{1-|\gamma|} & LHCP \\ \frac{E_{max}}{E_{min}} = \frac{|E_R|+|E_L|}{|E_R|-|E_L|} = \frac{|\gamma|+1}{|\gamma|-1} & RHCP \end{cases} \tag{2.15}$$

$$AR\ (dB) = 20 \log \frac{E_{max}}{E_{min}} \tag{2.16}$$

In the ideal case of circular polarization, the AR = 0 due to $E_{max} = E_{min}$. In contrast, linear polarization provides infinite AR. The antenna polarization is an essential factor in antenna-to-antenna communication. The transmission power between receiver and transmitter can be maximized when the polarization is matched. In contrast, whenever there is a polarization mismatch in antennas, electromagnetic (EM) power is lost, leading to faulty transmission and poor signal reception.

2.2 Wearable Antennas

Recently, wearable antennas and electronic technology have undergone rapid growth in various fields of modern applications, ranging from health monitoring, patient tracking, smart houses, and battlefield survival, which facilitate and upgrade the human's life with a wide range of applications: medical, RFID, satellite, mobile home, television, and Zigbee [31]–[32]. A slim, compact, and lightweight structure and low production cost are crucial characteristics of a wearable antenna. In this section, we will discuss the challenges related to developing wearable antennas. Next, some low-profile and high-efficiency antenna structures such as metasurface-enabled antennas, textile, electro-textile antennas, surface wave antenna (SWA), and antennas in far-field UHF RFID systems will be introduced.

2.2.1 Wearable Development Challenging and Requirement

Unlike in the wireless portable devices, the antennas in the wearable devices are in much closer contact with the human body, requiring unobtrusiveness and seamless cloth integration. Therefore, there are several challenging factors that we need to consider in wearable antenna development. Firstly, the wearable antennas have to balance the minimization of the human body's interaction and the robustness of the radiation properties. Besides, the wearable antenna should obey the regulations of healthcare, which will be discussed in detail below. On top of that, the primary distinction of the wearable antenna is often made of textile materials to ease the cloth integration and to make the wearer feel comfortable. Finally, the hardware of the wearable antenna should be compact and low-profile so that it can be worn in various locations on the human body.

Interaction of human tissue

The interaction of the human tissues with the EM wave propagation of the wearable antenna modifies the radiating properties of the wearable antenna. It results in several unwanted consequences, for instance, unwanted power absorption, the unfortunate shifting of operating frequency, and the undesirable deformation of radiation pattern compared to those measured in the air [33]-[35]. Secondly, the body's movement may significantly destruct the antenna structure, leading to modification of the input impedance and decreasing radiation efficiency [36].

Safety regulation

The electromagnetic wave transmitted and received by the antenna is absorbed by the human body, which may cause side effects such as heating up. Hence, one of the significant difficulties of developing a textile wearable antenna is achieving the

radiating specification and adhering to the health and safety damage requirements. The radiation power of the antenna should not be over the qualified specific absorption rate (SAR) or the power absorbed per unit mass index. The SAR index can be expressed as [37]

$$\frac{P}{\rho} = \frac{\sigma \mathrm{E}^2}{2\rho} = \frac{J^2}{2\rho\sigma} \tag{2.12}$$

where P is the power loss density (W/m^3), E is the electric field strength (V/m), J is the current density (A/m^2), ρ is the mass density (kg/m^3), and σ is the conductivity (S/m). The measured SAR of the antenna should obey the SAR standard of IEEE C95.1-2005 with a maximum value of 2 W/kg for the 10-g averaged, and the EEE C95.1-1999 standard restricts the 1-g averaged SAR to be less than 1.6 W/kg.

This research developed a wearable RFID reader antenna with the quasi-Yagi configuration shown in Publication III. We calculate the SAR index (SAR_{max}) based on the transmission power ($P_{t,max}$), the power fed to the RFID reader antenna, which causes SAR_{max} on the skin. The equation to calculate $P_{t,max}$ is [38]

$$P_{t,max} = \frac{1.6\,W/kg\,(1-|S_{11}|^2)P_{test}}{SAR_{max}}, \tag{2.13}$$

where S_{11} is the reflection coefficient of the antenna. P_{test} is the power available from the numerical test source that we set to 1 W.

Material selection

In the wearable antenna development, besides the design requirements of a typical antenna, the needs of the textile wearable antennas should be small size, low profile, lightweight, and easy to inconspicuously integrate and operate reliably for an extended period without restricting the user's activity. More importantly, the antenna should be made with a flexible, stretchable, and stable material that conforms to the human body. Therefore, several textile and flexible materials have been used to develop the wearable antenna, as in Table I.

Ref	Material (substrate/conductor)	Characteristic
[39]	cotton/conductive yarn	Textile
[40]	leather/conductive threads	Textile
[41]	jeans/flexible copper sheets	Textile
[42]	wood felt/nylon	Textile
[43]	commercial papers/copper sheet	Flexible
[44]	latex/silver nano-particle ink	Flexible

[45]	polydimethylsiloxane (PDMS)/silver nanowires	Flexible

Size restriction

As the wearable antennas are developed to be worn on the body surface, the total size of the antenna should be significantly miniaturized to fit some parts of the body, such as the arms, hands, or head. The standard techniques to compact the overall geometry of the antenna are folding and meandering the signal plane of the wearable antennas. In research [46], the wearable antenna with a rectangular Planar Inverted-F Antenna (PIFA) is developed on the flexible substrate. Also, the authors applied the folding and meandering techniques at the signal plane of the antenna to increase the electrical length and decrease the resonance frequency. Furthermore, the slots and stubs can be utilized for the wearable patch antenna optimization and tuned on the signal plane to reduce the antenna size [47]. In [72], the wearable antenna combines the non-conductive leather materials for the substrate and the copper fabric for the conductor; meanwhile, the miniaturization techniques are based on the rectangular slits and the short pins that connect the signal and ground plane.

2.2.2 Textile and Electro-Textile Antennas

Nowadays, a broad diversification in wearable antenna development is conceivable thanks to the intelligent utilization of the electro-textile materials that provide ease of integration into garments. The electro-textile antenna comprises two main elements: electrically conductive fabrics or electro-fabrics, applied for the radiating plane and the grounding parts, and dielectric materials used for the insulating layer between the radiating and ground planes. The most common type of electro-textile antenna is the microstrip structure because of its low profile and low volume, which can be integrated into the cloth without being visible. In addition, the design's simplicity, stability, miniaturization ability, and comfort can be an added advantage of the electro-textile antennas. Furthermore, with an entire ground plane, the patch configuration can secure the antenna performance in the worn body environment, such as radiation pattern, efficiency, return loss, and low SAR index due to antenna-body isolation.

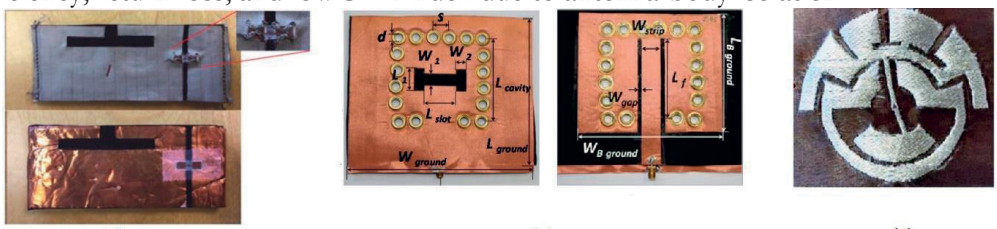

Figure 4. An E-textile RFID tag (a), wearable SIW antenna (b), and ultra-wideband antenna fabricated by the conductive E-thread (c).

The patch antenna for the UHF RFID tag is fabricated by flexible materials, conductive fabric conductors, and an Ethylene Propylene Diene Monomer (EPDM) substrate, as shown in Figure 4. The potential point of this antenna development project is the connection between the conducting plane and the RFID IC, particularly when embroidered with lightweight and highly flexible conductive yarn [47]. The conducting plane shape was cut by either scissors or a high-precision cutter called Summa Cut D60R and then adhered to the substrate. It offers simplification for integrating into the cloth and the comfort of several parts of the human body.

One of the novel antenna structures for off-body applications is a substrate-integrated waveguide (SIW) antenna [48], as shown in Figure 4. b; the SIW is known as the rectangular waveguide-like configuration in an integrated planar structure [49]. The main feature of the SIW construction structure is conducting vias embedded in the substrate that is sandwiched between the signal and ground planes. The SIW structure enables integration of the components, namely active and passive components, and even antenna, in the same substrate. Research [50] introduced the circularly polarized cavity-backed wearable antenna with SIW technology. The benefits of this structure are a smaller footprint compared to the classical SIW cavity and the rectangular antenna shape that allows manipulation of the resonance frequency.

Furthermore, the on-body quarter-mode substrate–integrated waveguide antennas with textile fabrication for WLAN/WBAN applications was presented in [51]. With the quarter-mode typology and the coaxial feeding technique, the size of the wearable antenna was reduced by 75%. Moreover, the antenna conserves the moderate gain and efficiency during on-body testing since the ground plane of the SIW antenna structure prevents an increase in permittivity and loss tangent due to the human body.

Another example of the electro-material ultra-wideband antenna fabricated by the conductive E-thread with conformality, flexibility, and robustness is illustrated in Figure 4. (c) [52]. The conducting textile surface was formed by metal-coated polymer E-fibers, 0.12 mm in diameter, which is automatically embroidered by the embroider programmable machine. This layer of textile conducting is easily integrated with cloth, and its behaviours and characteristics are identical to fabric with low visibility. Hence, by employing the embroidered e-textile conductor, we can maintain the RF performance of the antenna without changing the comfort and style of the cloth.

2.2.3 Metasurface-enabled Surface-wave Antennas

The surface wave antennas (SWA) are commonly used to provide the surface wave that propagates across the corrugated metasurface. The metasurface structure is commonly shaped by a regular texture of small unit cells printed on a grounded slab with or without shorting vias [53]–[58]. The initial concept of the surface wave antenna was also introduced in [59]. Some antenna configurations can produce the surface wave that is horn, dipole array, or pillbox with high gain and fan radiation patterns [60]. Compared to conventional surface wave antenna structure, the latest development is more attractive with low-profile conformal geometry, which is desirable in modern wireless communication systems [61]. The fundamental advancement of SWA is achieved by guiding the EM waves along thin ground with periodic patches. That structure is also called the artificial ground plane, which includes, for example, frequency-selective surfaces (FSS), soft/hard surfaces, electromagnetic bandgap (EBG) structures, and artificial magnetic conductors (AMC).

2.2.3.1 Complex Artificial Ground Plane Characterization

The two-dimensional periodic structure of a complex artificial ground plane is shown in Figure 5. This configuration is more straightforward than the mushroom-like EBG structure, thanks to the removal of the vertical vias between the periodic patches and the ground plane [61]. The operation frequency of the artificial ground plane is directly determined by gap g, width W, dielectric permittivity, and the thickness of the substrate h.

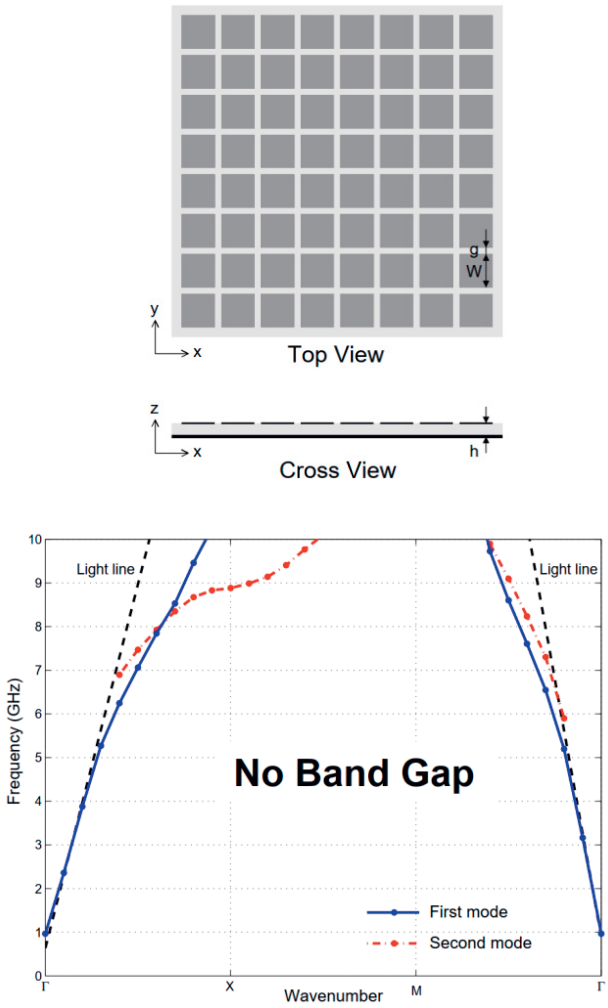

Figure 5. Structure of the artificial ground plane (left side) and the wavenumber versus frequency (right side) [61].

The finite-difference time-domain (FDTD) method is used to model the electromagnetic properties of the structure. The phase reflection of the artificial ground plane is consistent with those of the mushroom-like EBG structure for the incident waves. It declines from 180^0 to -180^0 as the increasing of the frequency. Since the shorting pin is removed, there is no surface wave bandgap at the operating frequency. However, the first surface wave mode has a wide range of frequencies.

2.2.3.2 Dipole Fed Surface Wave Antenna

The combination of the low-profile dipole antenna and the artificial ground plane is demonstrated in Figure 6. Since the dipole antenna operates as the transducer rather than the radiator, it is not essential to have the length exactly half a wavelength, and the total height of the antenna is 0.02λ. According to [62], this antenna can exhibit the monopole-like radiation pattern with a broadside radiation pattern and the directivity of 5 dBi. The firm surface wave is excited when the dipole is positioned to this artificial ground. The configuration of the periodic patches loaded on the ground provides no bandgap for the surface waves. The bandwidth of S11<-10 dB is 6%.

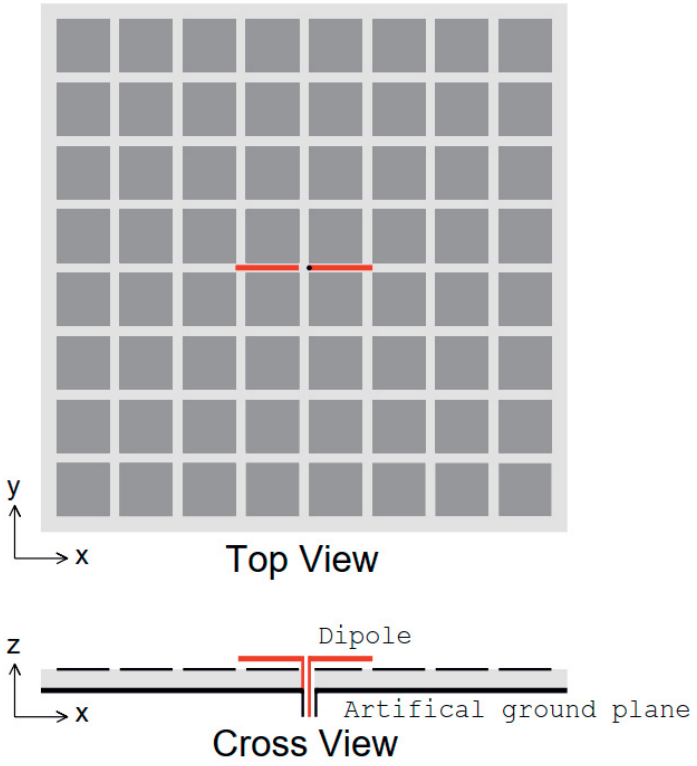

Figure 6. Horizontal dipole antenna on the artificial ground plane [62].

2.2.4 Wearable Metasurface-enabled Surface-wave Antennas

A cross-sectional view of a typical wearable metasurface-enabled antenna is illustrated in Figure 7. The first layer of the antenna is the radiating plane which is isolated to the periodic surface by a substrate. The last layer of the antenna is the ground plane made of high-conductivity materials, usually copper or silver inks.

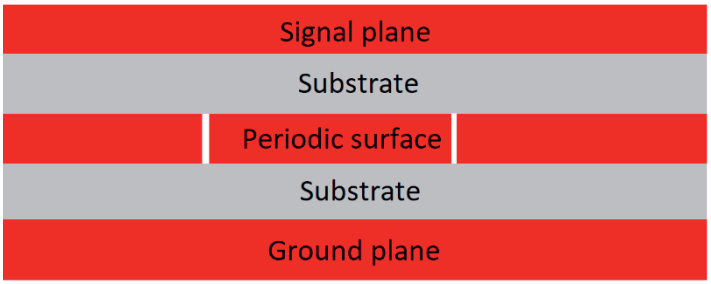

Figure 7. Cross view of the wearable metasurface-enabled antenna.

The Artificial Magnetic Conductor (AMC) produces the in-phase reflection characteristic while maintaining a low antenna profile and mitigating the coupling between the antenna and the human body. In the previous study [63], the wearable and flexible antenna was developed based on the combination of the monopole antenna and the AMC surface, as in Figure 8. Recently, AMC surfaces have become a popular method to upgrade the radiation behavior of wearable antennas [64][65], whereas the electromagnetic bandgap (EBG) was developed to minimize the detuning of the antenna operating frequency and to decline the specific absorption rate (SAR) while wearable upgrading the antenna gain. In wearable applications, the target of the EBG is to assist the launching waves for all incident angles on the antenna plane and all polarization states to obtain radiation patterns with high directivity on the antenna surface. Additionally, it remarkably upgrades the performance of antenna radiation efficiency, gain, and directivity while maintaining a small profile [66]–[71].

The flexible substrate is the flexible vinyl material, and the flexible polyimide Kapton is used for the conductor. The configuration of the AMC is optimized based on the Jerusalem cross, which enhances the antenna gain by 3.7 dB, reduces 64% of SAR at 2.45 GHz, and maintains the total size of the antenna: $65.5 \times 65.5 \times 3.2$ mm^3 $\approx$ $0.53\lambda \times 0.53\lambda \times 0.026\lambda$.

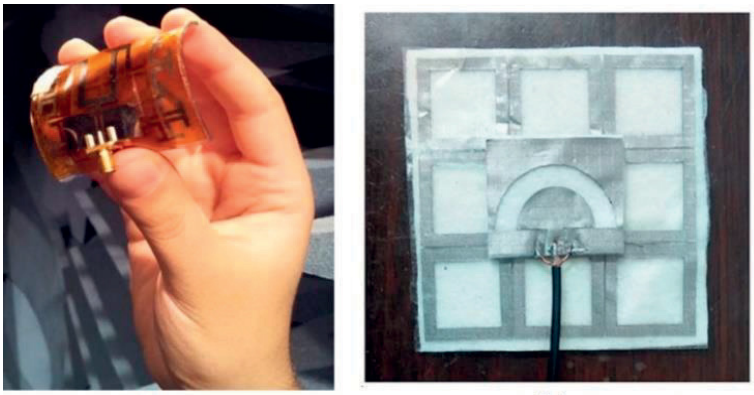

Figure 8. Flexible monopole antenna on the AMC surface (a) [72] and circular ring slot antenna on the periodic surface (b) [66].

The use of the periodic surface in textile materials for the wearable antenna is also investigated in research [69]. The circular ring slot antenna was integrated with a grid with 3 × 3 rectangular ring-shaped unit cells, as seen in Figure 8. The antenna is made of the wood felt substrate and nylon conductive textile materials, and the total size is 81 × 81 × 4 mm^3, with an operating frequency of 2.45 GHz. In the on-body measurement condition, the antenna achieved a high gain of 7.3 dBi, and the bandwidth of the −10 dB reflection coefficient is 14.7%. Furthermore, by applying the AMC layer, the antenna reduces the SAR index per 1 gram of tissue by 95% in comparison with the standalone circular ring slot antenna. The performance validation was also conducted by attaching the antenna in various human body positions, such as the legs, arms, and upper arm.

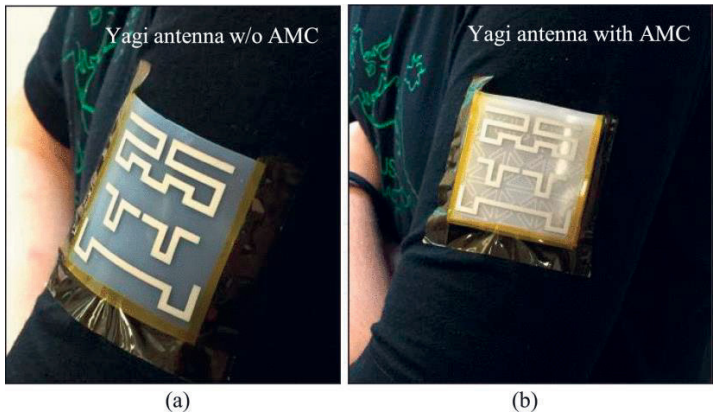

Figure 9. Yagi–Uda antenna without (a) and with (b) the AMC surface on the upper arm [44].

The combination of the Yagi–Uda antenna and the AMC surface to generate the end-fire radiation pattern along the antenna plane is demonstrated in the research [44]. The Yagi–Uda antenna is printed on the flexible latex substrate and installed under the AMC

surface to reduce the human body's interaction with the antenna's properties. Besides, this surface supports the launching wave for all angles; hence, it maintains the end-fire radiation pattern with high directivity along the human chest. Although the oversize of the antenna is only $50 \times 50 \times 9.5$ mm^3 $\approx 0.15\lambda \times 0.15\lambda \times 0.07\lambda$ as in Figure 9. , it provided a gain of 0.1 dBi in the end-fire direction.

Overall, the periodic surface has been used to isolate the radiating plane of the antenna with lossy materials as the body tissue, which significantly enhances the antenna's performance. Mainly, with the periodic surface, the wearable antennas aim for higher gain, radiation efficiency, and directivity, and lower SAR index compared to the case of a standalone antenna on the body surface. Besides, that surface also manipulates the launching waves to propagate along the antenna surface. Hence, it can maintain the radiation pattern of some antennas providing directive beams, namely quasi-Yagi antennas. With those reasonable offers, the periodic surface has become a good component for developing wearable antennas.

2.3 Methods of Material Characterization

As discussed in the above sections, the materials of the wearable antenna integrated into garments possess the low profile, flexibility, light weight, and stretchable characteristics to be comfortably worn by humans without preventing the movement of humans. Hence, the high-conductivity electron materials, namely, copper foil, Nickel fabric, and copper fabric, and low-conductivity materials, namely, EPDM and PDMS, are good options for the conductor and substrate, respectively. However, one of the challenges in antenna development is to require knowledge of the material electromagnetic properties, namely, permittivity and loss tangent of the substrate and conductivity of the conductor because most of the conventional characterization method does not apply to the textile materials [73]-[78]. The material property measurement with the cavity resonators and dielectric resonator methods provide high accuracy characterization for low-loss material. However, the characterization inaccuracy of this method is from many factors such as air gaps between a sample and metallic parts at the connection, computational inaccuracies, and dimensional uncertainties of the samples [72]. The research [76] also includes a simple method of dissipation factor estimation for the dielectric materials based on the reflection coefficient of the printed transmission lines. However, the characterization outcomes are susceptible to the uncertainty of the measurement equipment (VNA) and the losses from the SMA connectors.

A characterization method for high-density textile materials based on a new matrix-pencil two-line way with a frequency range from 1 to 10 GHz was presented in [79]. This characterization method extracts frequency-dependent relative permittivity of the

substrate by the matrix-pencil technique, which reduces the perturbations caused by geometry uncertainties and inhomogeneities of the microstrip transmission line structure. The outcome of the characterization estimation of the method is rigorously assessed by comparing the measurement and simulation reflection coefficient of the copper-based and Flectron-based patch antennas using the calculated parameters. However, the characterization method shows the errors when applied to the textile materials with a lower density due to the high degree of material inhomogeneities and the air gap between the conductor and substrate of the microstrip line. Besides, for the textile substrate for wearable antenna application, this characterization technique strictly requires identical conductive materials for the test structure because the estimation outcomes are sensitive to the conductivity of the conducting plane.

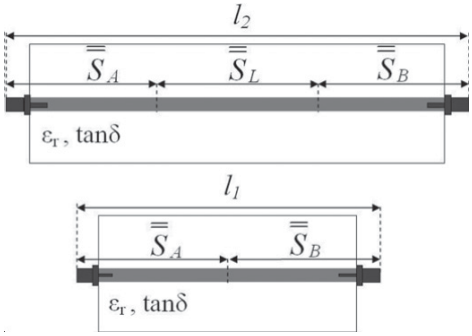

Figure 10. Two microstrip lines with different lengths l1 and l2 [44].

In this thesis, we introduced an applicable technique derived from the model fitting of simulation and measurement data to single out the frequency-dependent relative permittivity and loss tangent of the non-conductive line substrate and the bulk conductivity of the strip conductor [Publication I]. The main idea of our material characterization approach is to utilize the fitting data of the simulated numerical and measured transducer gain of the transmission line being tested by least square estimation. It provides approachability for users, ease of data analysis, and sufficient accuracy for wearable electronic development. It is important to note that this method is appropriate to estimate the electromagnetic properties of the unknown textile substrates and conductive materials for developing wearable microwave devices. We used the estimated data to construct the textile low-pass filters for further assessment, and we found consistency between the numerical model and measurement results. The validation results show that our proposed characterization method is appropriate to optimize the textile antennas and microwave components.

2.4 Operation Principle of a Passive Far-Field UHF RFID System

Radio frequency identification (RFID) technology was originally developed to wirelessly detect and automatically identify the items attached with the electronic RFID tags. The identification mechanism is based on the electromagnetic interaction between the tags and the dedicated reader. An RFID system can be classified as a near-field and far-field system based on the operating mechanism. The near-field system operates within a short range and relies on the EM near-field coupling mechanism. In contrast, the far-field system is based on EM wave propagation and therefore provides a substantially longer range. In practice, the far-field or long-range RFID systems are more common because they can balance the energy efficiency, low cost, and high detection range. Recently, by combining the small and low-cost passive RFID tags and the use of propagating electromagnetic waves at ultra-high frequencies (UHF) for activating and transferring the data of the tags, the RFID systems can identify a large number of the objects with extended range. Thanks to those advantages, the development of RFID-based sensors for biomedical application have been drawing attraction, for example, batteryless wireless sensor networks (WSN) and wearable and implantable sensors based on wireless body area networks (WBAN). These systems can be employed to track people or body movement monitoring and bio-medical sensing with wearable tags [80]-[87]. This section will overview the operation principles and performance characteristics of a far-field RFID system.

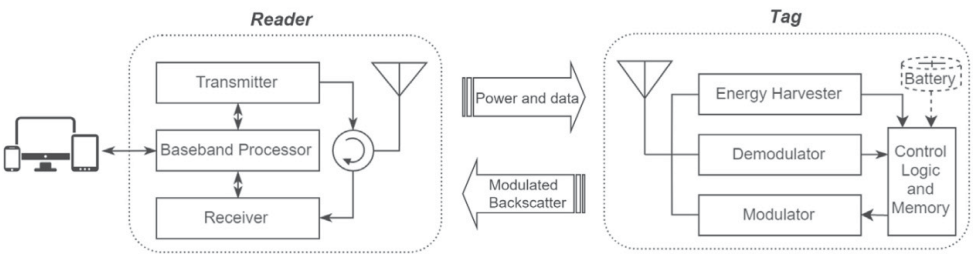

Figure 11. Main elements and operating mechanism of a passive UHF RFID system.

The readers, tags, and a system for data management are the main elements of the RFID system, and Figure 11. illustrates its main sections and operation principles. The RFID reader wirelessly powered the RFID passive tags by transferring the electromagnetic wave, and the tag-to-reader data link is rooted in modulated antenna scattering. A host computer controls the reader with data storage software consisting of a based band professor, a transmitter, and a receiver. The passive RFID tag contains only two main components: an RFID microchip (RFID IC) and an antenna. According to the EPC C1G2 standard, the RFID systems operate in a half-duplex style where the reader triggers initial communication [161]. More specifically, the

antenna is in charge of continuously capturing the energy from the reader. While waiting for a response from the RFID tag, the reader maintains transmission of the unmodulated carriers. Once the harvesting energy is sufficient to activate the semiconductor on-chip rectifier, the rest of the logic circuit of the IC is powered. However, the tags never send the data to the reader spontaneously; it only responds by modulating the request information in scattering by the impedance switching scheme when it receives the new requesting signal from the reader to record the data of on-chip memory. When the reader receives the amplitude or phase-shifted response from the tag, it can be decoded and stored in the data management system for further processing.

Forward power transfer and backscatter

This section demonstrates the communication characteristics between the RFID reader and the tags. The forward link, also called the reader-to-tag link, is defined as the power transmission from the reader antenna to the tag, determining the interrogation range between these components. In this section, we will discuss the link budget and the strategy to maximize the interrogation.

Forward link

The RFID reader transmits the electromagnetic waves to its far-field area or an interrogation region covering the tag position in the forward link. With the distance r between the reader and the tag, the power density of the RFID reader can be calculated by the result of the reader antenna gain (G_{tx}) and the power density of an isotropic antenna $\left(\frac{P_{tx}}{4\pi r^2}\right)$ as equation

$$S_t = \frac{P_{tx}G_{tx}}{4\pi r^2} \tag{2.13}$$

The power received by the RFID tag from the reader can be defined with the Friis' equation as [162][161]

$$P_{tag} = S_t A_{eff,tag}\chi_{pol} = P_{tx}G_{tx}G_{tag}\frac{\lambda^2}{(4\pi r)^2}\chi_{pol} \tag{2.14}$$

where λ is the wavelength of the operating frequency. χ_{pol} is the polarization loss between the reader antenna and the tag antenna. $A_{eff,tag}$ is the effective aperture in the direction of an incoming wave from the reader antenna.

According to the regulation for UHF RFID [88], the power output from the reader P_{tx} is restricted by the regional EIRP limit in Europe. Especially $P_{tx}G_{tx}$ cannot be over 3.25 W. Consequently, to maximize the operation of the forward link, the tag antenna should be rigorously optimized to balance a decent gain G, a high power

transfer efficiency τ, and proper impedance matching between the tag antenna and RFID IC.

Read range

The read range of the tag antenna is influenced by several factors, namely, surrounding environment, reader antenna, distance, and operation frequency. As discussed previously, the interrogation distance is limited by the power delivered from the reader to the tag IC. With high sensitivity (−80 dB), the reader can receive and process the signal from the tag as the power absorbed by the IC that is higher than the IC's power-on threshold P_{th}. The maximum interrogation range can be calculated from the Friis equation of the forward link budget by replacing the P_{ic} with P_{th} as

$$r_{forward} = \frac{\lambda}{4\pi}\sqrt{\frac{\chi_{pol}P_{tx}G_{tx}G_{tag}\tau}{P_{th}}} \tag{2.16}$$

In some cases, the sensitivity of the reader is low, and the backscattering power from the tag is dedicated to being detected by the reader. As a result, the interrogation range is restricted in the reverse link. In this case, the power intensity of the backscattered wave should be enhanced by modifying the tag modulation scheme.

3 MATERIALS AND METHODS

3.1 Microstrip Transmission Line

The microstrip line is a microwave transmission line with planar configuration formed by the strip conductors and a layer of isolating dielectric material commonly referred to as the line substrate. This type of transmission line supports the quasi-TEM (transverse electromagnetic) wave propagation toward the typical direction of the cross-sectional plane.

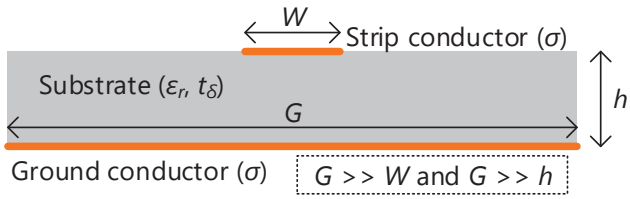

Figure 12. Cross-sectional view of a microstrip transmission line.

Due to the uncomplicated planar geometry, the microstrip line is widely used to form transmission line components and interconnections in microwave circuits [89]. The geometry of the microstrip line is specifically described in Figure 12. . The strip conductor width (W), the substrate thickness (h), and the substrate relative permittivity (ε_r) are determinants for the characteristic impedance (Z_0) of the line, and the phase shift of the signal experience per unit length. The thickness (t) and conductivity (σ) of the signal plane conductor and the substrate loss tangent (t_δ) are decisive to the signal attenuation per unit length.

As the electromagnetic field of the quasi-TEM wave carried by the line exists partly in air and partly in the line substrate, there is no closed-form field solution for it. Consequently, the design of the microstrip transmission line is based on approximate numerical formulas that enable the finding of an appropriate width-to-height ratio for a given line substrate to achieve the targeted characteristic impedance or vice versa and the designing of a line section with a given length relative to the wavelength of the signal in the line structure. To achieve this, the relative permittivity of the line substrate must be known. Similarly, the estimation of the signal attenuation, which is typically done with numerical simulators, requires all the material parameters as inputs: ε_r, t_δ, and σ.

Typically, the dielectric materials that present a sufficiently low attenuation per unit length to be considered as a substrate to a microstrip line are materials where the dominant source of EM energy loss arises from the polarizability, i.e., the continuous

re-orientation of the dipolar molecules due to the electromagnetic field associated with the wave propagation. With this assumption, using the notion of the complex relative permittivity ($\tilde{\varepsilon}_r$) that stems from the analysis of the time-harmonic electromagnetic fields using the complex phasor notion, we have [89]

$$\widetilde{\varepsilon_r} = \varepsilon' - j\varepsilon'' = \varepsilon'\left(1 - j\frac{\varepsilon''}{\varepsilon'}\right) \tag{3.1}$$

where j is the imaginary unit and $\varepsilon' = \varepsilon_r$ is the real physical value of the relative permittivity and $t_\delta = \frac{\varepsilon''}{\varepsilon'}$. Based on the dielectric relaxation phenomenon, the frequency dependency of the complex relative permittivity can be established through the Svensson/Djordjevic model [90]-[92] as

$$\widetilde{\varepsilon_r}(f) = \varepsilon_\infty + a\ln\frac{f_H + jf}{f_L + jf} \tag{3.2}$$

where f_L and f_H are defined as the low frequency and high frequency of the model. Through this model, the information of the relative permittivity and loss tangent at a given central frequency f_0 allows the estimation of their values at a range frequency around it through the following steps. Firstly, by comparing equations (3.1) and (3.2), we compute the constant a as

$$a = -\varepsilon_{r0}t_{\delta 0}\mathrm{Im}\left(\ln\frac{f_H + jf_0}{f_L + jf_0}\right), \tag{3.3}$$

where $\varepsilon_{r0} = \varepsilon_r(f_0)$ and $t_{\delta 0} = t_\delta(f_0)$. As a result, the constant ε_∞ can be computed from equation (3.2), and the $\varepsilon_r(f)$ and $t_\delta(f)$ can be solved from equation (3.2) as

$$\varepsilon_r(f) = Re\left(\widetilde{\varepsilon_r}(f)\right) \quad \text{and} \quad t_\delta(f) = -\frac{\mathrm{Im}\left(\widetilde{\varepsilon_r}(f)\right)}{\mathrm{Re}\left(\widetilde{\varepsilon_r}(f)\right)}. \tag{3.4}$$

3.1.1 Conductor Model

According to Maxwell's model of electromagnetism, the current density decays exponentially with the distance from the surface. This means that increasing the thickness of a conductor beyond a certain value brings little difference to how the current density is distributed across the cross-section, and thus, the energy loss can be estimated based on the surface layer only. Considering a thin conductor that carries the same total current, this means that current density remains high within the whole layer and increases exponentially as the layer becomes thinner. This current packing leads to increased energy loss due to the material's finite conductivity. To assess the layer thickness with respect to this phenomenon, the skin depth (δ) is defined as the distance over which the current density has declined by a

factor of $1/\exp(1) \approx 0.3679$ from its value at the surface. For a good conductor, the skin depth is approximated as [89][93]

$$\delta = \sqrt{\frac{2}{\omega\mu\sigma}}, \tag{3.5}$$

where ω is the angular frequency, μ is the magnetic permeability, and σ is the bulk conductivity of the material.

In this research, we have employed the two-sided skin effect model that assumes that the current is directed on the two planar conducting strip surfaces having a width much larger than the thickness [90]. This assumption holds true, especially for the strip and ground conductors of a microstrip line, as normally $t \ll W \ll G$, so that the loss contribution from the vertical sides of the conductor is negligible. Further, to consider the skin effect at two dominant faces of the conductor, it can be divided into two equal layers, both having a thickness of $t/2$, each modelling thin sheets in parallel. The surface impedance of each thin sheet is then given by [93]

$$Z_s = \frac{(1-j)}{\delta\sigma}\cot\left((1-j)\frac{t}{2\delta}\right). \tag{3.6}$$

This allows the efficient and accurate numerical estimation of the conductor loss that considers the impact of the finite thickness of the conductor without resorting to a full-wave EM field solver.

Considering the power loss factor of a (microstrip) transmission line of a given length *d*, defined as the ratio of the power available from the output terminal of the line to the power delivered to its input terminal, given by $e^{-2\alpha d}$, where α is the attenuation constant (in units [1/m]) determined by the cross-sectional geometry and the EM properties of the materials involved. In terms of the general theory of two-port microwave networks, this power fraction is the maximum power gain ($G_{\max}$) of the system that can be realized under the simultaneous complex conjugate impedance matching at the input and output terminals of the system. It can be computed directly from the two-port network parameters through the formula [89]

$$G_{max} = \frac{|S_{21}|}{|S_{12}|}\left(K - \sqrt{K^2 - 1}\right), \tag{3.7}$$

where *K* is given by

$$K = \frac{1-|S_{11}|^2-|S_{11}|^2+|\det(\mathbf{S})|^2}{2|S_{12}S_{21}|}. \tag{3.8}$$

The scattering parameters or S-parameters are commonly used, as they are readily extracted from the standard microwave measurements by the vector network analyzer (VNA). Thus, considering the equality $G_{\max} = e^{-2\alpha d}$, we can directly

compute the power loss factor of the whole line from the simulated and measured S-parameters as G_{max}.

Within the scope of this thesis, we use a microstrip transmission line as a test structure to estimate the dielectric properties of the line substrate as well as the conductivity of the strip and ground conductors through data fitting by using the simulated G_{max} as the model function dependent on the material properties to be fitted to the measured result.

3.2 Modelling of The Properties of The Human Body

Nowadays, computational modelling has played an essential role in the research of electromagnetics [94][95], medicine development [96], and injury biomechanics [97][98]. In this research work, since the antennas operating on the body surface have been developed for wearable application, the numerical model of the human body needs equipment to illustrate the unexpected interaction of human tissue on EM wave propagation on the antenna. In other words, the inhomogeneous body model can provide crucial information about the human tissue on the antenna radiation parameters [99][100]. In addition, the model is used to predict the absorbed EM energy by the body tissue or the specific absorption rate (SAR). According to the guideline of the IEEE C95.1-1999 and IEEE C95.1-2005 standard, the SAR cannot exceed 1.6 W/kg for 1 g of tissue and 2 W/kg for 10 g of tissue, respectively [101][102]. Based on this parameter, tissue safety can be evaluated when developing an antenna for wearable or implantable applications.

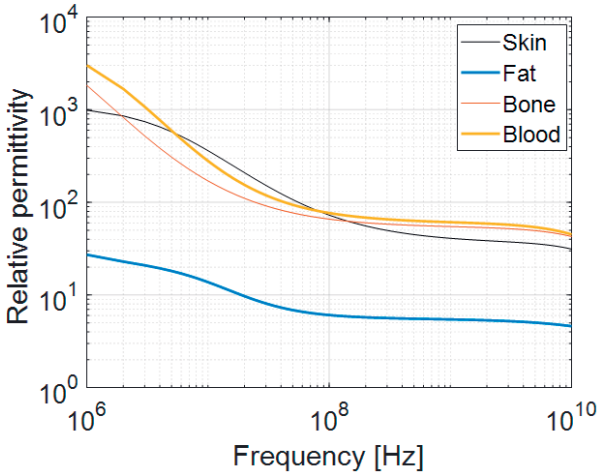

Figure 13. Relative permittivity of human tissue types.

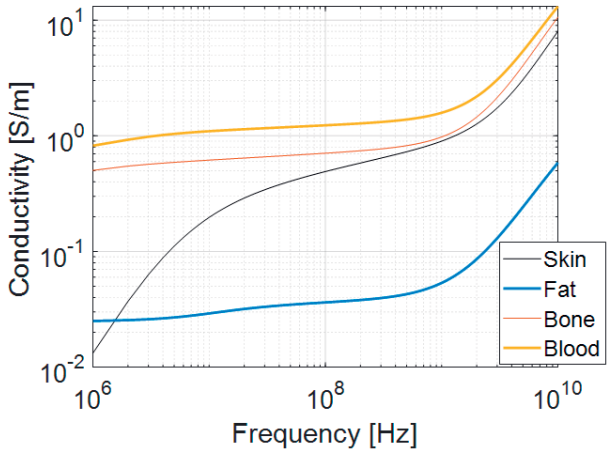

Figure 14. Conductivity of major tissue types.

In general, the dielectric properties are the intrinsic parameters that determine the EM behavior of the electric field in that material. Thus, in this research, it is important to obtain knowledge of human tissue's relative permittivity and conductivity. That procedure provides information to predict the interaction between the biological tissues and EM waves. The relative permittivity of the human tissue is impacted by various phenomena, namely, the penetration and propagation characteristics of the EM waves into the living environment, the interaction between human tissue and EM waves, and the effects of the interaction on the tissues (heating or depolarization of cell membranes). Figure 13. and 14 demonstrate the relative permittivity and loss tangent of the skin, fat, bone, and blood, which are tissues close to the wearable antennas. The data of the electromagnetic properties were provided by the IT'IS tissue dielectric databases [103] based on Gabriel's measurements and the four-term Cole-Cole dielectric relaxation model [104].

At 900 MHz, the skin depth of the tissue is 1 cm, and the amplitude of the electric field and magnetic field declines by 1/e. This means that if the wave propagates in 3 cm of the tissue, only 1% of the energy is left. Table I shows the electrical properties of the skin and other parts of the human body [103]. Overall, the conductivity and relative permittivity of human tissue are higher than common electronics materials. The anatomical model of the human body consists of a multilayer of several tissues, i.e., bone, fat, and skin with complex thickness. In practice, it is difficult to precisely estimate the size and dimension of these tissues to model in the simulation environment. Hence, we model the body as a simplification body with cuboid and cylinder objects in this research scope. The skin is the primary material since it is the nearest tissue to the wearable antenna and among the lossiest of materials (σ = 0.855 S/m and ε_r = 41.85 at 915 MHz [103]).

TABLE I.

ELECTRICAL PROPERTIES OF INDIVIDUAL TISSUE LAYERS AT 915 MHZ

Tissue	σ (S/m)	ε_r
Skin	0.8555	41.587
Fat	0.050242	5.4673
Muscle	0.93146	55.114
Bone	0.13926	12.486

3.3 Geometry of The Human Model

In HFSS simulation software, the modelling of the human body geometry is constructed by the embedded CAD tools. The model of the human tissue can be classified as the canonical or simplified and anatomical models. The anatomical model extracts the adult human body in a high accuracy of 1 mm and a high revolution of the medical data of the tissues with 300 muscles, organs, and bones. The example of the anatomical model of the full body and the head is shown in Figure 15. The human model is developed with two main methods: magnetic resonance imaging (MRI) or cryosection. The anatomical model is developed from the Virtual Population project based on the MRI scan of the whole body. Meanwhile, data of the Visible Human Project were optimized by the high-accuracy scanning figures of cryosections. The human anatomical model is commonly used in the antenna simulation since this model accurately predicts the unexpected interaction of the tissue to the EM wave propagation and radiation of the antenna. Hence, by applying the anatomical model, the prediction results from the simulation of wearable and implantable antennas can be matched to the measurement data, which helps to optimize the antenna geometry to meet the specification. However, there are some disadvantages to this modelling. Firstly, running a microwave device simulation with this model usually requires a long time due to the high resolution of the details. Furthermore, since the anatomical models contain the medical graphics of a particular scanned individual, it is challenging to modify the single sections of the model, making it difficult to study the anatomical variability.

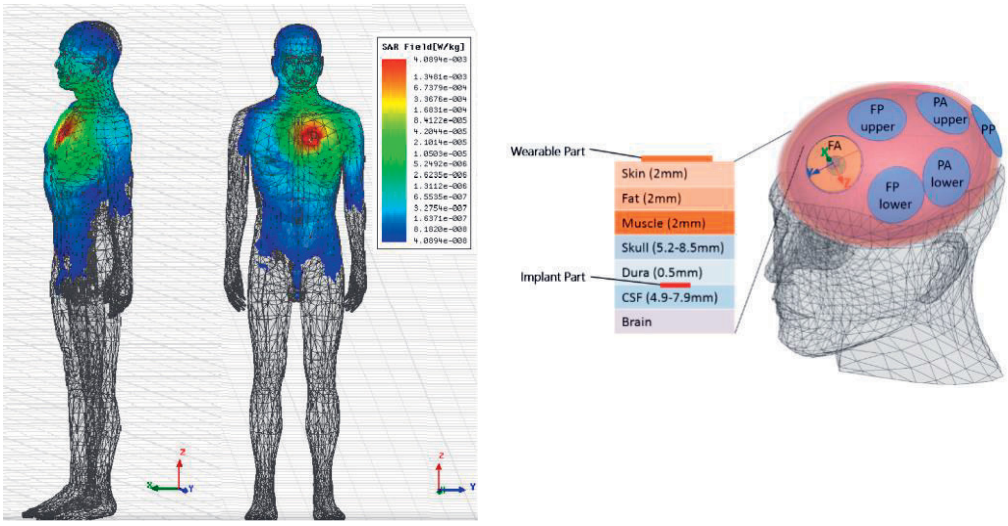

Figure 15. Anatomical models of body (left side) and head (right side) [105]-[106].

Another form of the human model is canonical, which simplifies human body sections as geometry primitives such as cuboid, spherical or cylindrical. For example, the cylinder is used for modelling the forearm [Publication IV], the cuboid model can be used for the back in [Publication VI], and the spherical model is made for the human head. In terms of material characteristics, the canonical model can be made of single or multilayer tissue to approximate the human body better. The canonical model can be made by a single layer of skin for wearable antenna development [107]. The advantage of the canonical model is the simplified structure that enhances the speed of the simulation and reduces the consumption of the computational resources. In addition, the canonical model offers adjustability in analysing the influence of the tissue's geometry variation on the microwave device performance. However, because the canonical body model simplifies the human tissue by modelling the main tissues close to the antennas, this may impact the accuracy of simulation outcomes, radiation efficiency, directivity, and impedance matching [108].

In this thesis work, to obtain an optimal balance between the computational resource and the accuracy of the antenna simulation outcomes, we first attached the wearable antenna on the canonical human body model with the skin. This approach allows us to study the influence of each element of antenna geometry on performance. For example, we simultaneously run the sweeping of the L-slots and the truncated corner for the circular polarization patch antenna on the cuboid model to the minimize axial ratio and maximize the radiation efficiency [Publication V] [Publication VI]. Next, once the antenna simulation has been done, we validated the final results of the antenna properties with the anatomical model of the male. With this simulation

strategy, the simulation period can be reduced, and the high accuracy of the antenna performance prediction can be achieved.

3.4 Experimental Characterization of UHF RFID Tags

The measurement of the RFID tag is conducted in the anechoic chamber to avoid the interruption of unexpected signals and the multipath propagation renderings. The measurement is based on the ramping of transmitted power; hence, neither tag nor reader antenna needs to be changed during measurement. This measurement strategy improves repeatability and accuracy. The main idea of ramping power is to adjust the transmission power by the reader to the tag. The smallest response power of the tag to the reader is defined as the threshold power (P_{th}) of the tag. In terms of RFID measurement instruments, we used the Voyantic Tagformance RFID measurement system [109] that provides the measurement channel characterization to compensate for the possible multipath effects. This measurement system also considers the link loss factor (L_{iso}) from the transmit port of the reader to the input port of a hypothetic isotropic antenna placed at the tag's location. The equation showing the relationship between the power delivery from the transmit port of the reader to the IC (P_{tag}) and the link loss factor (L_{iso}) is given as

$$P_{tag} = \chi_{pol} G_{r,tag} L_{iso} P_{th} \Rightarrow G_{r,tag} = \frac{P_{ico}}{\chi_{pol} L_{iso} P_{th}}, \tag{3.15}$$

The measured read range of the tag with the multipath compensation and antenna properties for wearable applications in particular.

$$d_{tag} = \frac{\lambda}{4\pi} \sqrt{\frac{P_{tx} G_{tx}}{L_{iso} P_{th}}} \tag{3.16}$$

The axial ratio of the UHF RFID tag antenna on the body surface is conducted in the anechoic chamber, as shown in Figure 17. We rotated the RFID reader antenna 360° in the z-axis with a step of 10°. Compared to the conventional method that captures the AR by rotating the tag [Publication V], our latest approach yields improved accuracy while considering the antenna on the body as the whole antenna platform [Publication VI]. Next, we used the maximum and minimum attainable read range $d_{tag,max}$ and $d_{tag,min}$ from the radiation measurement to calculate the corresponding maximum and minimum polarization efficiency Γ_{+LIN} and Γ_{-LIN} between the RFID tag and the linear polarization reader antenna given by

$$\frac{\Gamma_{+LIN}}{\Gamma_{-LIN}} = \left(\frac{d_{tag,max}}{d_{tag,min}}\right)^2 = \left(\frac{1+|\gamma_{tag}|}{1-|\gamma_{tag}|}\right)^2, \tag{3.17}$$

where γ_{tag} is the circular polarization ratio of the tag antenna [103]. The equation to calculate the axial ratio is given by [103]

$$A_{tagRH} = \frac{|\gamma_{tag}|+1}{|\gamma_{tag}|-1} \quad \text{and} \quad A_{tagLH} = \frac{1+|\gamma_{tag}|}{1-|\gamma_{tag}|} \tag{3.18}$$

where A_{tagRH} and A_{tagLH} are the axial ratios of the right-hand and left-hand circular polarization antenna. The corresponding polarization efficiency when the circular polarization RFID reader antenna is given as

$$\Gamma_{RHC} = \frac{1}{1+|\gamma_{tag}|^{-2}} \text{ and } \Gamma_{LHC} = \frac{1}{1+|\gamma_{tag}|^{2}} \tag{3.19}$$

where Γ_{LHC} and Γ_{RHC} are the left- and right-hand circular polarization reader antenna (LHCP and RHCP), respectively. With this information, we can estimate the attainable read range of the tag when using an ideal RHCP reader antenna as

$$d_{tag,RHC} = d_{tag,max}\sqrt{\frac{\Gamma_{RHC}}{\Gamma_{+LIN}}} = d_{tag,min}\sqrt{\frac{\Gamma_{RHC}}{\Gamma_{-LIN}}}, \tag{3.20}$$

where $\Gamma_{\pm LIN}$ is computed from equation (3.19). While the attainable read range of the RFID tag measured by the LHCP reader antenna can be estimated as

$$d_{tag,LHC} = d_{tag,max}\sqrt{\frac{\Gamma_{LHC}}{\Gamma_{+LIN}}} = d_{tag,min}\sqrt{\frac{\Gamma_{LHC}}{\Gamma_{-LIN}}}, \tag{3.21}$$

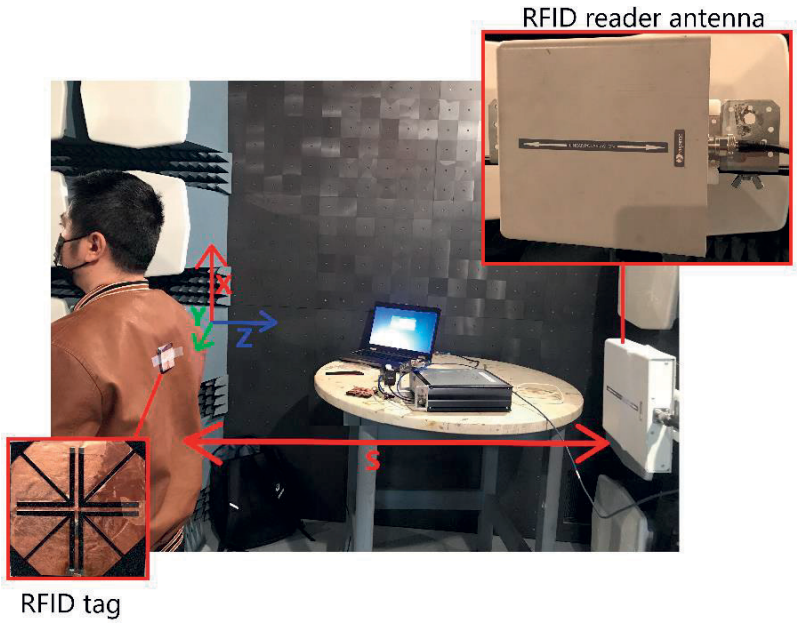

Figure 16. Measurement setup for the circular polarization patch UHF RFID tag.

4 RESULTS AND DISCUSSION

4.1 Textile Material Characterization by Microstrip Transmission Line Model Fitting

As discussed in Subsection 2.2.1, the major challenge in developing the antennas and microwave circuits is to acquire the electronics information of the substrate and conductor. In the wearable RF device development, the initial requirement is to comprehend the relative permittivity and loss tangent of the flexible textile substrate and the bulk conductivity of the conductor. Although much research reported the RF characterization method based on resonators and waveguides [73]–[78], these strategies do not apply to the unknown textile materials because the accuracy of the characterization outcomes is relatively dependent on the manufactured validating structures. This research proposed a high-efficiency characterization method for textile materials that stem from the numerical model fitting. Our approach accurately estimates the frequency-dependent relative permittivity and loss tangent of the substrate of the non-conductive line and the bulk conductivity of the fabric conductor. Moreover, the RF characterization's results were stringently validated with testing RF passive circuit optimization, such as passive microwave circuits. One example is the low-pass filters, which are relatively sensitive to the properties of the substrate and conductor materials. The excellent consistency of the modelling outcomes and measured data from the final validation results confirmed the precise prediction of the proposed textile materials. With the ease of applying and simplifying data processing, our proposed characterization method is appropriate to flexible materials for progressing wearable electronics.

4.1.1 The Method and Results

The main strategy of the textile material characterization is to extract the material properties, namely, the relative permittivity ε_r, loss tangent t_δ, and bulk conductivity σ based on the best-fit data of measured and simulated maximum transducer gain G_{max} of the microstrip lines. The G_{max} is the chosen parameter to find the best-fit data because it is sensitive to the material properties and the critical element to evaluate the performance of an RF device. The simulated maximum transducer gain is swept over a given interval in the numerical model, and the extract G_{max} corresponds to the simulated

scattering matrices S_{sim} over the frequency range from 400 MHz to 3 GHz. The sum of the squared residuals illustrates the sum of the relationship between the simulation and measurement data (S_{mes}) as

$$E(\epsilon_{r0}, t_{\delta 0}, \sigma) = \sum_{n=1}^{N} \left(G_{max}\left(S_{sim}^{(n)}\right) - G_{max}\left(S_{mes}^{(n)}\right) \right)^2, \quad (4.1)$$

where n is the number of frequency points. Our proposed method implementation contains two steps. Firstly, we constructed the microstrip lines made by the copper foil conductor and the unknown textile substrate material. Then we predict the relative permittivity and loss tangent by G_{max} that provide minimum $E(\varepsilon_{r0}, t_{\delta 0})$. Secondly, with the consistent approach, we approximate the bulk conductivity of the textile conductor of the line constructed by the substate with estimated ε_{r0} and $t_{\delta 0}$. Now, the conductivity is extracted by the corresponding G_{max} where the minimum $E(\sigma)$ exists.

In this research, we numerically estimated substrate properties of several substrates, namely, textile cell-rubber foam ethylene-propylene-diene-monomer (EPDM) [110], Arlon AR1000 high-permittivity laminate [111], and FR4 circuit board [112]. Next, we estimate the bulk conductivity of two conductive fabrics: nickel- and copper-plated fabric (LessEMF) [113] and copper-plated fabric (LessEMF) [114].

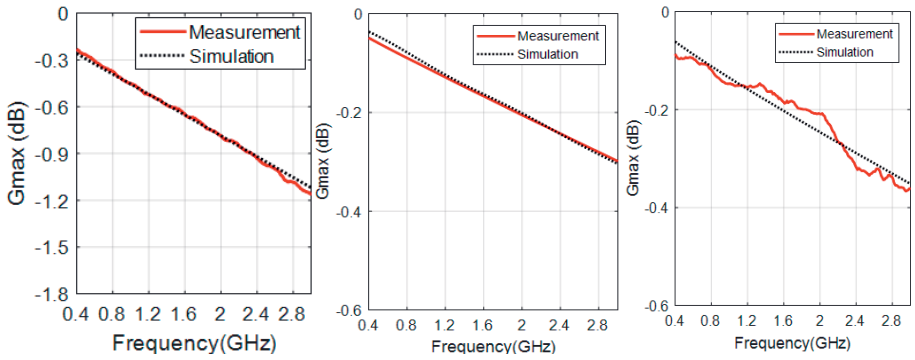

Figure 17. Agreement between simulated and measured maximum transducer gain of the lines generated by AR1000 (left), EPDM (centre) with copper foil, and FR4 with NCPF (right) [Publication I].

Finally, we performed the least square estimation method as equation (4.1) to single out the best-fit data by MATLAB in the frequency range of 400 MHz to 3 GHz. That frequency range covered a wide range of wireless communication bands for the wearable applications MedRadio at 401–406 MHz, the worldwide ISM band centered at 2.45 GHz, GPS at 1575.42, and UHF RFID bands at 866 MHz and 915 MHz. Figure 17. shows the excellent agreement of the simulated maximum transducer gain from the numerical model with those from the measurement in the whole range of the frequency, thanks to the least-square estimation. There is a small fluctuation of the maximum

transducer gain of the transmission lines with the FR4 substrate and NCPF conductor. This issue may be from manufacturing errors, such as the air gap between the conductor and substrate. Table II demonstrates the estimated RF characteristics of the textile substrate and conductor materials with a center frequency of 1 GHz. Overall, findings in relative permittivity and loss tangent of FR4 and AR1000 are parallel to those of the manufacturing datasheet [110][111]. Due to the slight difference in the substrate thickness of our circuits and those from the manufacture, our estimation for the permittivity is slightly higher than the provided data. Our method also provides a good estimation for the relative permittivity of textile substrate EPDM of 1.54 fitting in the range of 1.24-1.78 reported in [115]. The obtained value for the bulk conductivity of the conductor is 0.7×10^5 [S/m] and 2.6×10^5 [S/m] for the nickel- (NCPF) and copper-plated fabric (CPF), respectively.

TABLE I

Properties of the test lines [Publication I]

Step 1: Estimation of the dielectric properties.						
	Thickness [mm]	Conducto-r	Conductor thickness [μm]	Conduct-ivity [MS/m]	Strip width [mm]	Strip length [mm]
FR4	1.5848	Plated copper	35	58	6	65
AR1000	0.127	Plated copper	35	58	6	65
EPDM	3	Adhered copper foil	40	58	6	65
Step 2: Estimation of the conductivity.						
	Conductor thickness [μm]	Substrate (FR4) thickness [mm]	Estimated ε_r at 1 GHz	Estimat-ed substrat-e t_δ at 1 GHz	Strip width [mm]	Strip length [mm]
NCPF	76	1.5848	4.43	0.017	3	65
CPF	73	1.5848	4.43	0.017	3	65

TABLE II

The estimated material parameters [Publication I]

Dielectric properties				
	Estimated values		Reference values	
	ε_r at 1 GHz	t_δ at 1 GHz	ε_r at 1 GHz	t_δ at 1 GHz
FR4	4.43	0.017	4.3…4.4 [119]	0.019 [116]
AR1000	12.99	0.003	10 [117]	0.0035 [118]
EPDM	1.534	0.01	1.24 - 1.78 [115]	
Conductivity [S/m]				
NCPF	0.7×10^5	CPF	2.6×10^5	

The variation of relative permittivity and loss tangent corresponding to the frequency of 400 MHz to 3 GHz is illustrated in Figure 18. Although we usually use the constant value for the substrate properties in microwave development, our estimation method shows that the substrate properties gradually vary as the frequency increment.

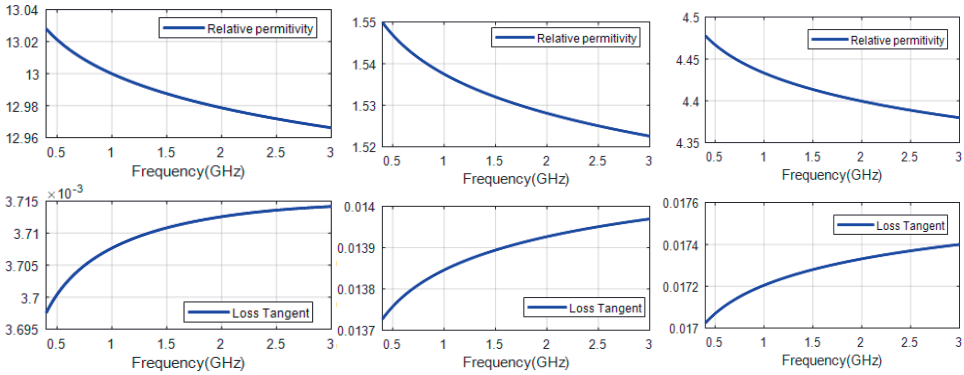

Figure 18. Relative permittivity and loss tangent of various substrate materials, namely, AR1000 (left), EPDM (center), and FR4 (right) [Publication I].

4.2 Estimated Material Parameter Validation by a Textile Low-Pass Filter

This section focuses on validating the characterization outcomes by applying the estimated material properties to optimize the RF passive circuits, such as low-pass stub filters (LPSF) and low-pass stepped impedance filters (LPSIF). The low-pass

filter is chosen as the testing candidate due to its high sensitivity to the material characteristics and the simplification of fabrication.

The low-pass stub filter with third-order topology is developed for the 50 Ω system impedance system with a 1.5 GHz passband at a maximum of 1 dB signal attenuation, and a stopband −10 dB at 2.2 GHz as Figure 19. The filters were manufactured as 3 samples, namely, SF1, SF2, and SF3. The SF1 sample combines the FR4 substrate and copper, and SF2 and SF3 are made of the EPDM with adhered CPF and CNPF, respectively. Its PCB layout is demonstrated at the top right corner of Figure 19. We also fabricated three different versions for low-pass stepped impedance filters with the passband corner frequency with 3 dB attenuation at 1 GHz and stopband starting frequency with more than 15 dB attenuation at 2 GHz. SIF1 combines the FR4 and Copper, and SIF2 and SIF3 are manufactured by the EPDM substrate and the CPF and CNPF, respectively.

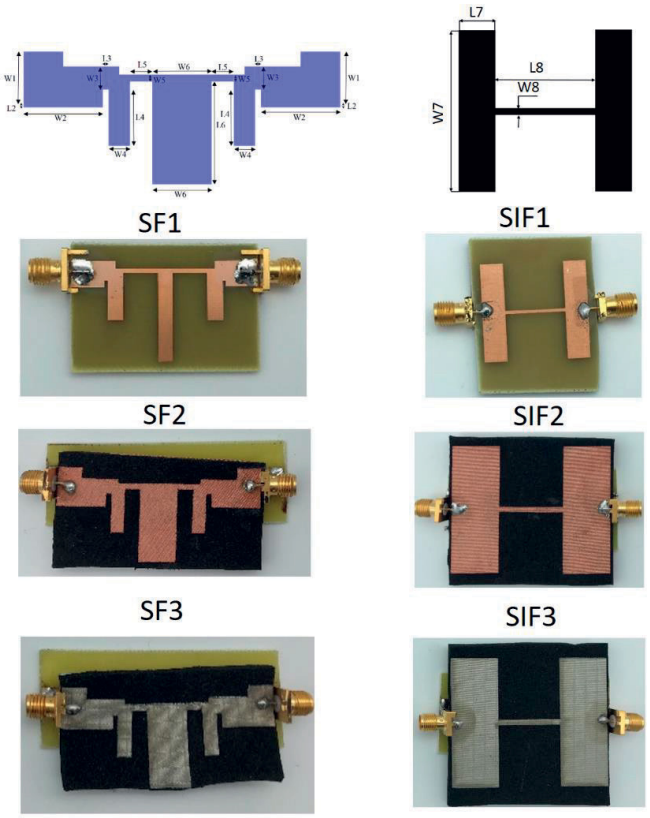

Figure 19. Layout and fabricated samples of the low-pass filter. Low-pass stub filter: SF1, SF2, and SF3. Low-pass stepped impedance filter: SIF1, SIF2, and SIF3 [Publication I].

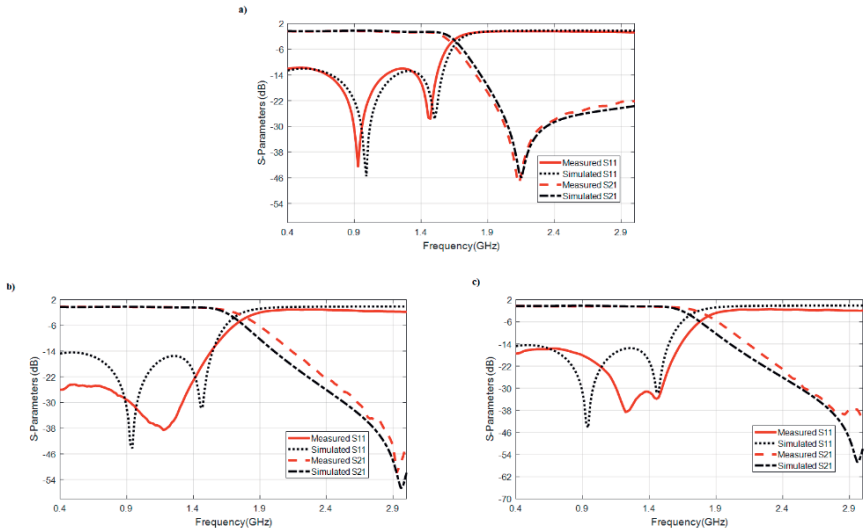

Figure 20. Comparison of the simulated and measured S-parameters of the low-pass stub filters. Top: SF1, bottom left: SF2, bottom right: SF3 [Publication I].

The low-pass filter layouts were optimized and tuned in Keysight ADS. The geometry of the low-pass stub and stub impedance filters are reported in detail in TABLE III and TABLE IV, respectively.

TABLE III

LOW-PASS STUB FILTER GEOMETRICAL PARAMETERS

Symbol	Dimension (mm)		
	SF1	SF2	SF3
W1	7.8	9.2	9.2
W2	7.7	13.8	13.8
W3	5.67	4	4
W4	4.88	3.7	3.7
W5	0.8	1.2	1.2
W6	3.71	10.3	10.3
L2	1.091	0.5	0.5
L3	0.7	1	1
L4	8.6	9.8	9.8
L5	7.8	3.8	3.9
L6	20.66	17.9	17.9

TABLE IV

LOW-PASS STEPPED IMPEDANCE FILTER GEOMETRICAL PARAMETERS

Symbol	Dimension (mm)		
	SIF1	SIF2	SIF3
W7	25	43	43
W8	1	2	2
L7	15	21	21
L8	1	2	2

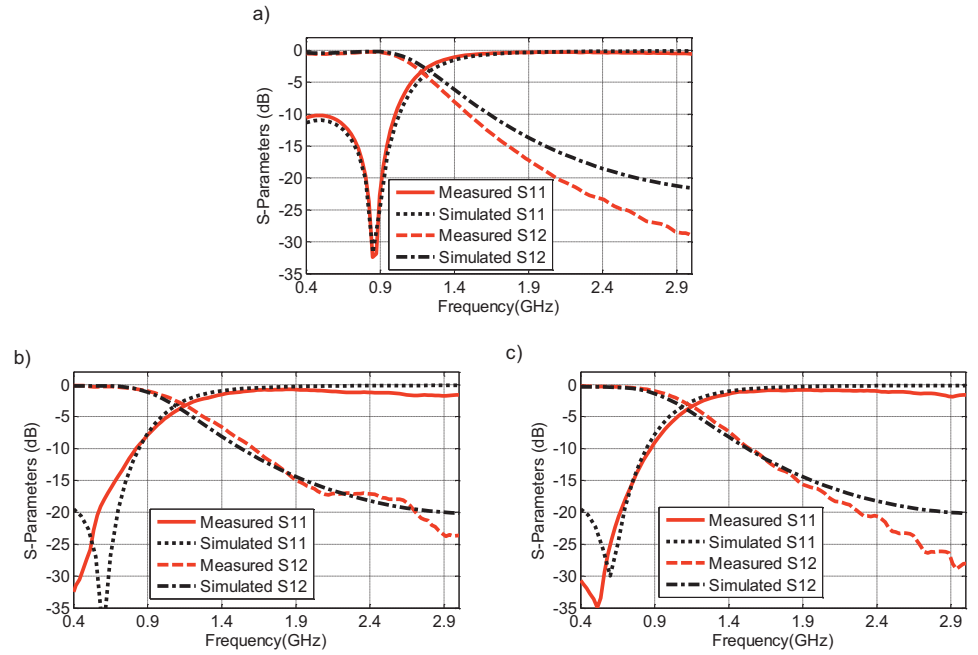

Figure 21. Comparison of the simulated and measured S-parameters of the stepped impedance filters. Top: SIF1, bottom left: SIF2, bottom right: SIF3 [Publication I].

By employing the estimated material parameters, the LPSF and LPSIF provided excellent agreement between the simulated and measured S11 and S21, as shown in Figure 20. and Figure 21. , respectively. Overall, both filters meet the operation specification with a low reflection coefficient at the bandpass and high attenuation at the stopband. Although a minor difference between modelled and fabricated samples can be observed at the stopband, it is likely from the negligible variation of the width of the lines and the effects of electrical transition between the calibration phase reference plane of VNA and the point where the SMA connectors contact the line. In conclusion, the good agreement between measurement and simulation data of validating low-pass filters assure the efficiency and applicability of our proposed material property estimation to the wearable microwave devices.

4.3 Dual-Mode Quasi-Yagi / Dipole Antenna for a RFID Headgear

Wireless communication technology has been increasingly important to medicine, healthcare, and body-area electrical systems. As part of the research, the passive UHF RFID technology has been found compelling to both wearable and implantable sensors [85][86][13][14][87]. Here, the integration of sensing

functionalities to the RFID tags provides low-power backscattering communications for the sensor readout. However, the RFID tags are most commonly single-layer structures based on dipole or slot antennas that cannot decouple human tissue interaction to the EM radiation. As discussed in Subsection 2.2.1, the major challenge in developing antennas for wireless wearable devices that operate close to the body is maintaining appropriate and stable electromagnetic performance. To solve that challenge, the multilayer antenna structures that include a ground plane have been proposed for wearable antenna development [120][163][164]. In addition, the small patch antenna for headgear application as military berets was also reported [152]. However, it is strenuous to direct the radiation pattern of the antenna along the body's surface with this approach since the antennas with ground planes typically exhibit a broadside radiation pattern. They radiate most of their energy to a solid angle that is approximately orthogonal to the antenna structure.

Nonetheless, from the perspective of applications, radiation along the body surface is also essential. Previously, a monopole-like pattern antenna based on an ellipsis-shaped center-fed microstrip patch antenna was introduced for headgear [120]. However, this antenna was optimized to operate at 5.8 GHz, which is not compatible with the UHF RFID band with the center at 915 MHz. As a remedy, in this section, we introduce a wearable dual-ID RFID tag based on a quasi-Yagi antenna. The novel feature of the antenna is from the combination of the quasi-Yagi and dipole antenna on a signal plane and the periodic surface. With the assistance of the periodic surface, the surface wave can propagate along the antenna plane. This supports the end-fire radiation pattern with high directivity on the body surface, and the tag can achieve a high read range in front of the user head direction of the tag. Besides, thanks to the folding technique, the antenna structure fits to the male head, which was $0.25\lambda \times 0.25\lambda$ or 80 mm by 80 mm. In the simulation, the performance of the antenna was validated by the simplified and anatomical body models. Furthermore, the radiation properties of the fabricated antenna were verified on the anechoic chamber with the on-body environment.

4.3.1 Body Model and Antenna Configurations

To obtain high accuracy estimation for the radiation properties of the wearable antenna on the body surface, such as radiation pattern, directivity (D), radiation efficiency (e), and read range for the tag (d_{tag}), we optimized the antenna with a simplified polygonal cylinder. We verified the final antenna performance by the anatomical head model with details of human tissues, as illustrated in Figure 22. The full-wave electromagnetic solver ANSYS HFSS v.17 is used to process the estimation of the antenna properties.

Although the human body has a highly intricate internal structure, the anatomical head model [165] comprises 15 different tissue types and 58 separate tissue sections; we have used a homogenous filling for both models. However, our previous results have shown that the internal structures and tissue properties had an insignificant impact on the simulated radiation properties of wearable antennas. In contrast, the external shape of the model influenced the radiation properties more [89]. Thus, in this work, we have used models with a homogenous filling. Because the skin is the closest tissue material to the antenna, we assigned its EM properties (ε_r = 41.6, σ = 0.86 S/m at 915 MHz [103]) to the filling. The simplified polygonal cylinder model with a dimension of 300 mm × 90 mm was used in initial parametric studies. Next, the optimization was finalized using the ANSYS anatomical human head model of an adult male. In both models, the antenna was bent along the curvature with a radius of 22 cm. This way, we can save computational resources and time. Comparing the computational cost between the two models, the simplified model reduces the simulation time and size of the computation mesh by 33% and 30%, respectively.

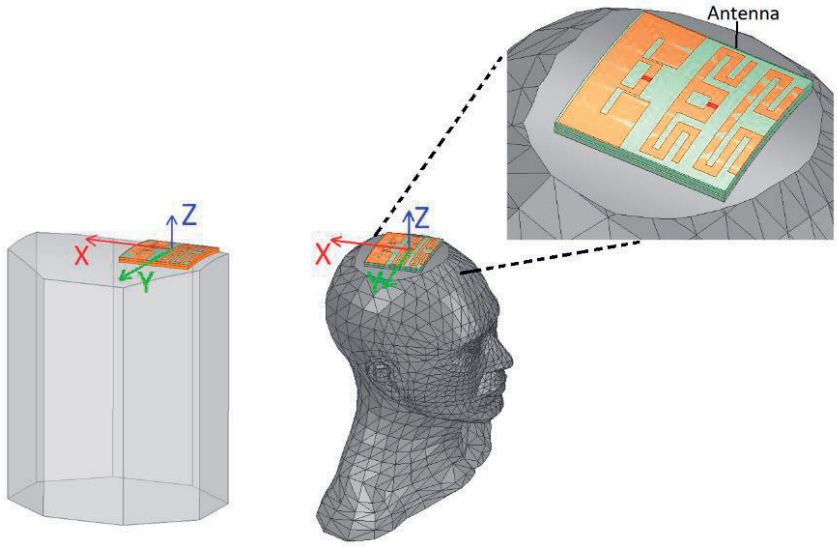

Figure 22. Simplified polygonal cylinder and anatomical body model [Publication III].

The first step of the antenna development is to consider the printed quasi-Yagi antenna [121], which is the planar version of the Yagi–Uda antenna initially developed in 1926 by H. Yagi and S. Uda [121]. The quasi-Yagi antenna is widely used in telecommunication and radar applications due to its high directivity and radiation efficiency, low profile, and simplification of fabrication. Because of these enormous advantages, we proposed this antenna configuration to produce an end-fire radiation pattern with high directivity along the top of the head surface. The antenna with multilayer geometry is inspired by previous research, where the

combination of the Yagi–Uda latex antenna and the AMC (artificial magnetic conductor) is made to generate the near-end-fire radiation pattern [123][124]. This research installed the printed quasi-Yagi antenna on the periodic surface which included a grid of unit cells. The configuration and the analysis of the unit cells and periodic surface will be discussed in the next section. The top view of the antenna, the implemented prototype, and exploded view of the wearable quasi-Yagi antenna are illustrated in Figure 23. According to the top peer-review prints on the quasi-Yagi antenna, the antenna, which mainly contains director, driver, and reflector elements, are folded to fit an adult's head; simultaneously, the antenna's operating frequency is maintained at the UHF frequency band. Overall, the total size of the antenna is 80 mm × 80 mm (or 0.25λ × 0.25λ, where λ is the wavelength at 915 MHz). As discussed in Subsection 2.1, unlike the typical 50 Ω antenna design, we connected the antenna with the RFID IC of NXP UCODE G2iL RFID microchip with the equivalent circuit as the parallel connection of the resistor R = 2850 Ω and the capacitor C = 0.91 pF as the model of frequency-dependent impedance. At 915 MHz, the estimated impedance of the RFID IC is approximately 12.8−*j*191 Ω. There is one interesting aspect in this research that we also attached the RFID IC to the reflector to reuse this element as the second RFID tag with a dipole configuration. Hence, the antenna can spontaneously generate the end-fire radiation pattern along the body surface and the broadside directivity upward from the user's head.

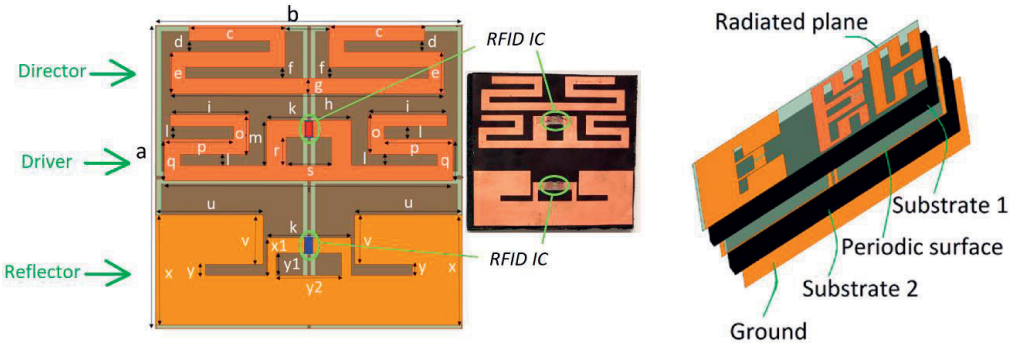

Figure 23. The top view (left side) and an implemented prototype (middle) and the exploded view of the quasi-Yagi (right side) [Publication III].

TABLE V
SIMULATED ANTENNA PARAMETERS

a	b	c	d	e	f	g	h	i	k	l	m
80	80	25	3	73	3	4	72	21	22	4	11
o	p	q	r	s	x	t	u	v	x1	y1	y2
12	18	11	7	12	29	75	28	13	10	6	17

In terms of simulation setup, we excited the input power in two ports and considered the antenna a two-port network. As shown in Figure 23. , Port 1 (red mark) is set up for the quasi-Yagi antenna to achieve end-fire directivity, while Port 2 (blue mark) is for the dipole with broadside directivity. Under perfect conjugate matching conditions, the coupling between two ports is −10 dB, which is not significantly high and non-negligible for the two-port antenna system. In the simulation, we used the frequency-dependent port terminations to account for the loading effect of the ICs, and the antenna array effects existed at general N-port RFID grids [125][89].

The fabricated signal plane of the antenna is shown in the middle of Figure 23. The tag antenna was patterned from 18 μm thickness copper printed on the 35 μm Polyethylene terephthalate (PET; ε_r = 3.2, σ = 0.003 S/m [126]) flexible substrate. The RFID IC was attached to the conductive proxy (Circuit Works CW2400). The maximum power transfer between antenna and RFID IC is secured when both components have the conjugate impedance matching at two ports. To deal with that issue, we tuned the size of the inductive matching loops constructed around the feeding points with parameters r and s for the quasi-Yagi driver and x_1 and y_1 for the second dipole antenna.

The exploded view with the layer-by-layer of the quasi-Yagi antenna is demonstrated in the right side of Figure 23. Overall, the proposed RFID tag antenna contains five layers. The first layer is the radiating plane made by flexible materials and stacked on the ethylene-propylene-diene-monomer (EPDM) rubber foam (ε_r = 1.53, σ = 0.01 S/m [Publication I]). The periodic surface is also composed of bendable materials as the conducting plane and sandwiched between two layers of EPDM. The last layer is the ground plane, which plays a key role in minimizing the human body's interaction with the radiating properties of the antenna, and the material of this layer is the flexible copper foils. Generally, all antenna elements are composed of lightweight, flexible, and bendable materials to secure the wearer's comfort.

4.3.2 Periodic Surface Optimization

The main function of the periodic surface is to assist the launching of the surface waves on the antenna plane within a specific frequency range. This improves the end-fire radiation pattern of the quasi-Yagi antenna [127][128]. Secondly, the metal layer that is part of the periodic surface helps to isolate the quasi-Yagi antenna (which does not include a ground plane) from the body. Hence, the gain, radiation efficiency, and radiation pattern of the antenna with the periodic surface are improved compared to the stand-alone antenna on the body. Since the quasi-Yagi antenna is formed by dipole-type elements, inserting a simple solid metal plate behind it to isolate it from the body would not be feasible since the current image phenomenon would deteriorate its efficiency [121].

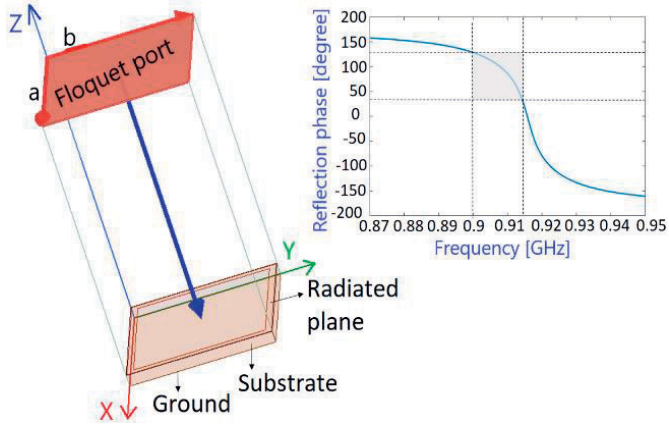

Figure 24. Floquet port simulation of the reflection phase of the periodic surface [Publication III].

The geometry of the periodic surface is illustrated in Figure 25. The periodic surface is made from the 2-by-2 grid of the square loop unit cells and isolated to the ground plane by the EPDM substrate. Like the signal plane, the material of the periodic surface is copper printed on the thin, flexible, and lightweight Polyethylene terephthalate. The unit cell is optimized by the Floquet port boundary condition [128] to obtain $90^0 \pm 45^0$ reflection phase response at the desired UHF RFID frequency region, centred at 915 MHz, as shown in Figure 24. Once the phase reflection value is achieved as the target, the unit cell geometry is tuned to minimize the total size of the periodic surface to fit the total size of the antenna and enhance the stability of the reflection phase concerning the direction of the reflection of the incident wave. As the unit cell geometry, we chose the square loop shape for research, which is suitable for bending vertically and horizontally [129]. The original design is optimized for a 9.5 GHz operating frequency; however, we tuned this unit cell configuration to 915 MHz without enlarging the total size of the periodic surface over the adult male head.

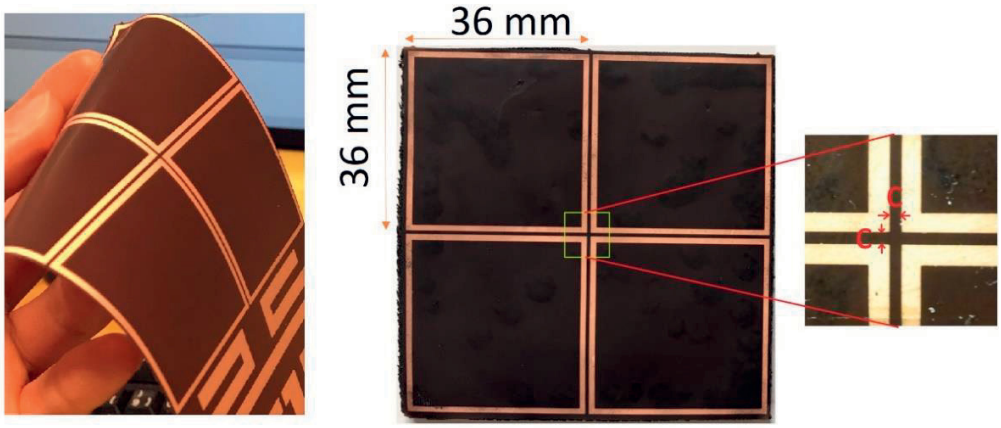

Figure 25. Fabricated prototype of the periodic surface [Publication III].

4.3.3 Simulation and Measurement Results

The directivity of the quasi-Yagi and dipole antennas is shown in Figure 26. At 915 MHz, the highest quasi-Yagi antenna directivity is 6 dBi at $\varphi = 180^0$ and $\theta = 45^0$, and dipole-based reflector antenna directivity is 5.8 dBi at $\varphi = 180^0$ and $\theta = 0^0$. At the same time, the quasi-Yagi antenna can provide approximately 4 dBi of directivity at the directive beam from the user's head.

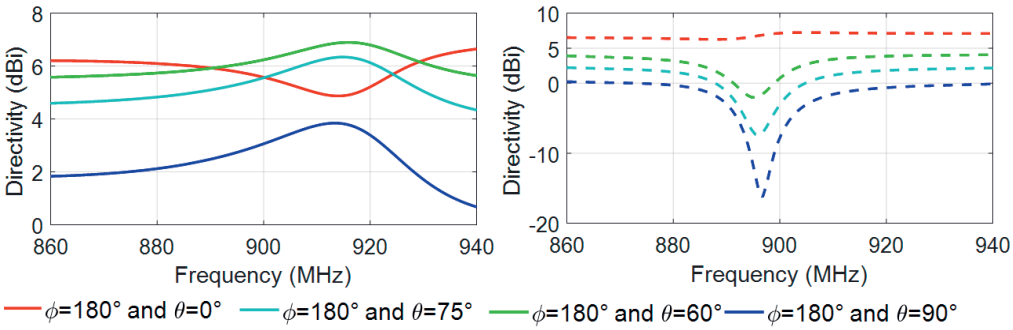

Figure 26. Directivity of the quasi-Yagi antenna (left side) and the dipole antenna (right side) [Publication III].

The impedance matching between the quasi-Yagi antenna and the dipole antenna with the RFID IC is illustrated in Figure 27. At 915 MHz, both antennas have good conjugated impedance matching with RFID IC, thanks to the cautious tuning of the inductive matching loop. In particular, the input impedance of the dipole is $16+j166$ Ω, and the quasi-Yagi antenna provided input impedance of $42+j192$ Ω, which leads to the corresponding power efficiency τ and reaches 75% for dipole and 74% for the quasi-Yagi.

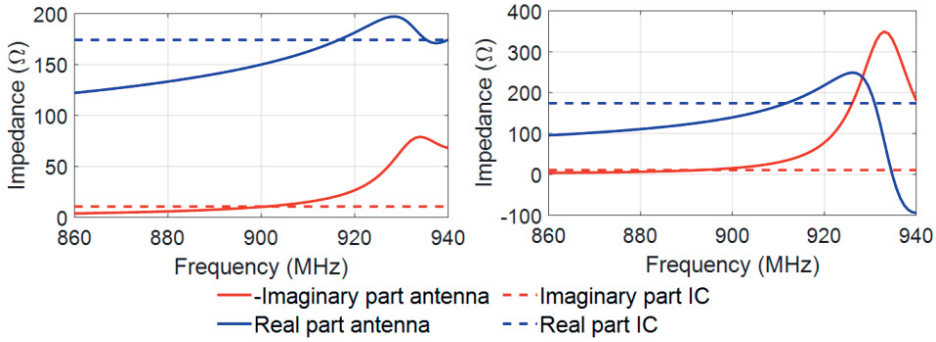

Figure 27. The impedance of the dipole antenna (left) and the quasi-Yagi antenna (right side) [Publication III].

As shown in Figure 28. , the quasi-Yagi antenna's radiation beam covers the region of $0^0 \leq \theta \leq 90°$, with the range of directivity being 4 dBi $\leq D \leq$ 6.2 dBi. On the other hand, the dipole-based reflector produces the directive beam upward from the wearer's head with the peak directivity of 7 dBi at $\varphi = 180°$, $\theta = -15°$.

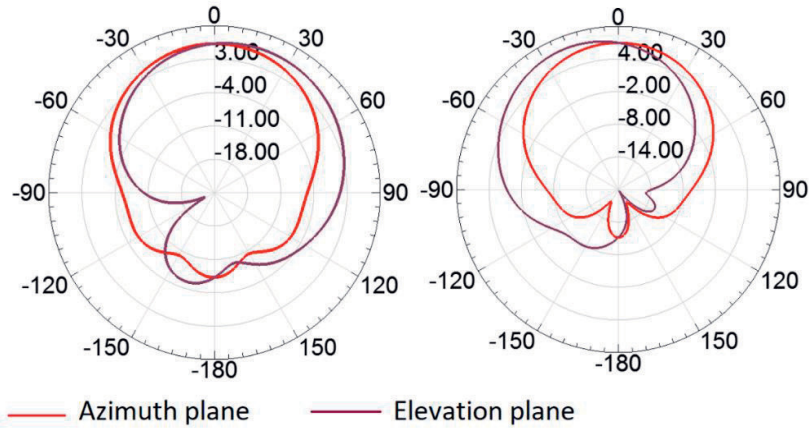

Figure 28. Directivity pattern of the quasi-Yagi antenna (left) and the dipole antenna (right side) [Publication III].

Figure 29. demonstrates the simulated current distribution of the quasi-Yagi antenna and dipole antenna at 915 MHz. The current flow is concentrated on the driven element and director in the quasi-Yagi antenna. Meanwhile, the current density is strong at the reflector in the dipole mode.

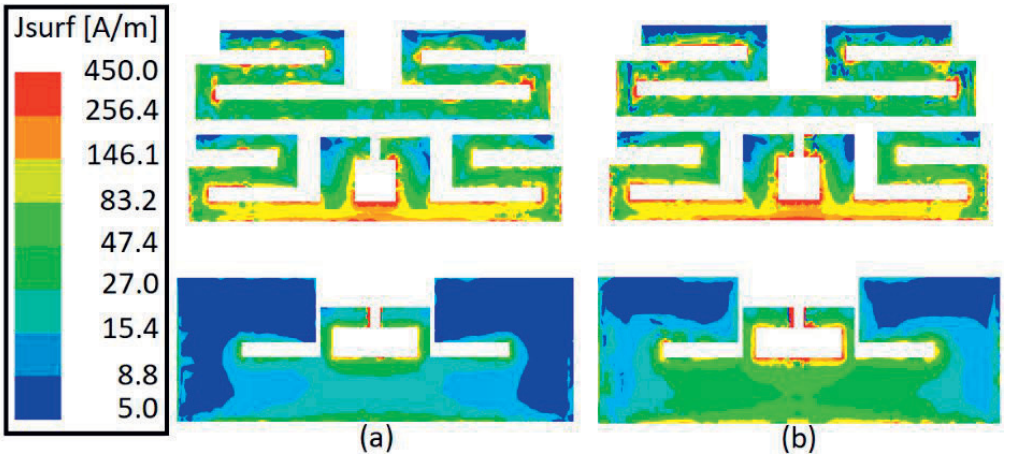

Figure 29. Surface current amplitude is visualized on the signal plane of the quasi-Yagi antenna when (a) the driven element (end-fire radiation mode) and (b) the reflector is excited (dipole radiation mode) [Publication III].

Measurement setup and results

The wireless measurement of the RFID tag antenna was conducted using the Voyantic Tagformance measurement system inside the anechoic chamber following the threshold power measurement technique outlined in Subsection 3.4. All of the measurement was implemented with the head-worn configuration. It is noted that the RFID tag is carefully aligned on the wearer's head to match the RFID reader and avoid the polarization mismatch. As shown in Figure 32. , the RFID tag is directly faced to the RFID reader to capture the read range of the quasi-Yagi antenna in the user's head direction. At the same time, the second measurement reader is positioned above the wearer's head to obtain the read range of the dipole antenna.

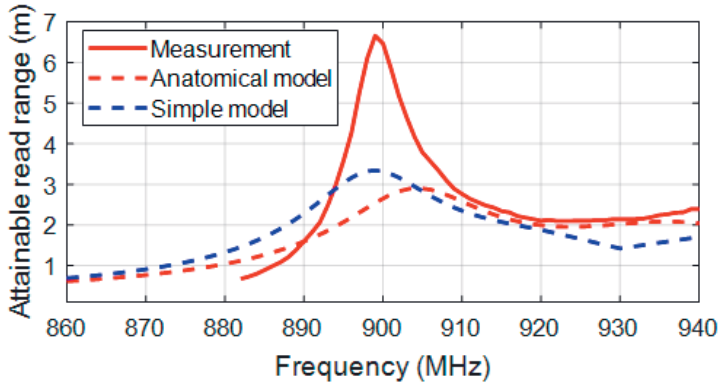

Figure 30. Read range of the tag in quasi-Yagi radiation mode [Publication III].

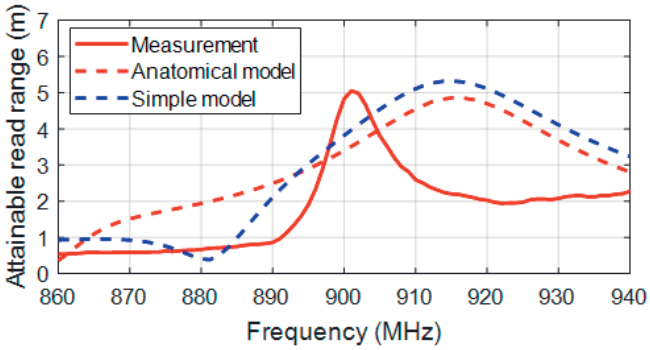

Figure 31. Read range of the tag in the dipole radiation mode [Publication III].

The comparison between the simulated and measured read range of the quasi-Yagi antenna and dipole antenna is indicated in Figure 30. and Figure 31. , respectively. To assess the accuracy of the simulation model, we compared the simulation read range to those of the anatomical head model and simplified the cylinder head model. At the UHF RFID frequency band, the simulated quasi-Yagi antenna with head models reaches a peak of 3 meters at around 900 MHz. Meanwhile, the highest measured read range is 6.8 meters in the line of sight of the user direction. The maximum detection range of the dipole antenna tag is 5 meters at 902 MHz, which was approximate to the simulation results. The movement of the body during measurement in the chamber may cause the difference of the measured and simulated peak read range of the RFID tag with dipole antenna configuration. Besides, the presence of the hair in the measurement is also a main reason of shifting the peak measured read range to 900 MHz.

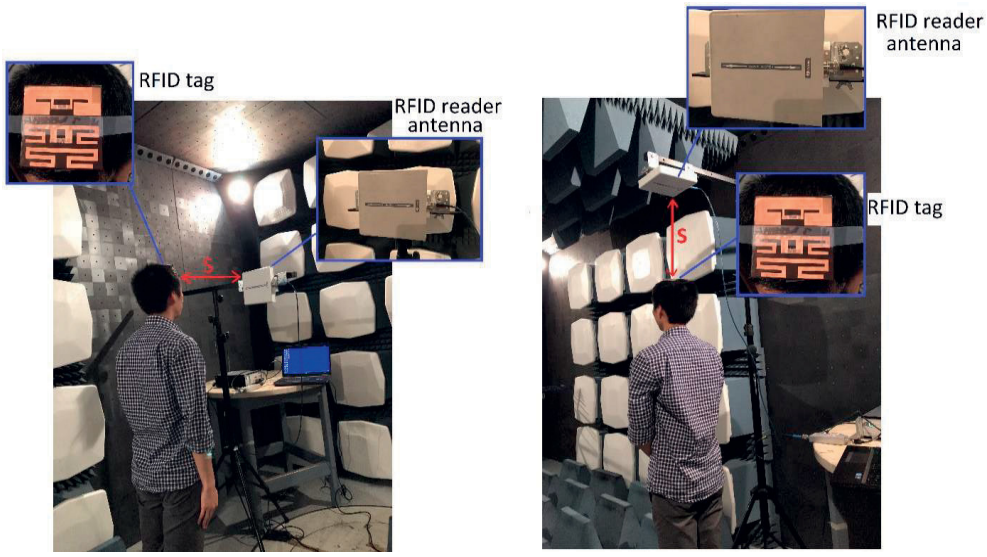

Figure 32. Read range measurement of the quasi-Yagi antenna (left) and the dipole antenna (right side) [Publication III].

Overall, the read range of both RFID tags is significant for identification applications. One of the most interesting aspects is that we successfully built up a dual-ID platform in one antenna structure that upgrades the versatility and spatial coverage of the system without enlarging the dimension of the antenna.

4.4 Forearm RFID Reader Antenna based quasi-Yagi Configuration

Recently, various research has been conducted to develop the efficient wearable RFID reader antenna [130][131][134][135]. Previously, the wearable readers wrapped around the wrist [135] and ankle [129] and attached to the gloved hand [131] have been introduced. However, most of these wearable antennas possess a radiation pattern that is orthogonal to the body surface. A wearable reader antenna with a quasi-Yagi configuration for the smart glove with an end-fire radiation pattern was reported [136]. This antenna operates at the near-field region, and the measured attainable tag read range was found to be only 0.33 m. Another study demonstrated a work gloves antenna with the slotted patch and a split ring resonator configuration for the RFID reader [24]. The antenna contained the ground plane suppressing the coupling of the antenna and the body. Hence, the radiation performance was remarkably upgraded, and the tag detection range was 3 meters. Nevertheless, this antenna pattern direction is outward from the body tissue. This section presents the adaptation of the wearable quasi-Yagi antenna on a periodic surface to establish a forearm UHF RFID reader that interrogates tags from the surrounding environment at the pointing direction of the arm.

Compared with the dual-ID headgear UHF RFID tag presented in Subsection 4.3, the reader antenna functions in a single-port configuration, which is matched to 50 Ω impedance, the curvature of the forearm is much larger than that of the head, and the form factor of the antenna is more limited by the width of the forearm than its length. As a result, the forearm antenna cannot be derived from the headgear tag antenna with minor modifications but requires completely new development. As a reader antenna, it also requires a different testing procedure.

4.4.1 Antenna configuration and simulation model

The proposed quasi-Yagi antenna with a low-profile and planar structure can be straightforwardly wrapped around the forearm. Besides, this form of antenna configuration can provide a directive beam along the body surface and assists the reader in detecting the UHF RFID tag toward the user's forearm. Furthermore, since

the antenna is set up on the body surface, that is, the lossy material that contains the negative impacts on the radiation properties, we mounted the quasi-Yagi antenna on the periodic surface to maintain the characteristics of the electromagnetic wave and end-fire radiation pattern of the antenna.

The antenna includes the reflector, driver, and director as the typical configuration of the quasi-Yagi antenna, as illustrated in Figure 33. The total size of the antenna is minimized to fit the restricted space of the forearm and maintains a 0.5λ electrical length of the antenna elements, thanks to the meandering and folding techniques. The length of the director and reflector are 243 mm (0.74λ) and 263 mm (0.8λ), respectively. The driven element is transformed into two loops. The first, with a radius r_1, is utilized to tune the impedance matching with the source, and the function of the second loop with r_2 is to enlarge the electrical length to 253 mm (0.77λ). As discussed in section 4.3.2, the periodic surface inhibits the unpredicted reaction of the body tissue on the antenna performance and assists the launching waves on the antenna plane, which helps the quasi-Yagi antenna maintain the end-fire radiation pattern. To provide comfort to the wearer and to ease the bending, we chose a configuration without a shorting pin between the signal and ground plane for the unit cells, which is suitable for generating surface-wave propagation on the antenna plane. The aim of the unit cell optimization is to achieve a 90°±45° phase reflection response at the UHF RFID frequency under Floquet port analysis[128]. This phase reflection response target also supports the conjugate matching between the antenna and 50 Ω input source. To consider the impacts of transformation of the unit cell shape when attached to the forearm, we bend the unit cell with the radius of an adult forearm of 46 mm, as in Figure 34.

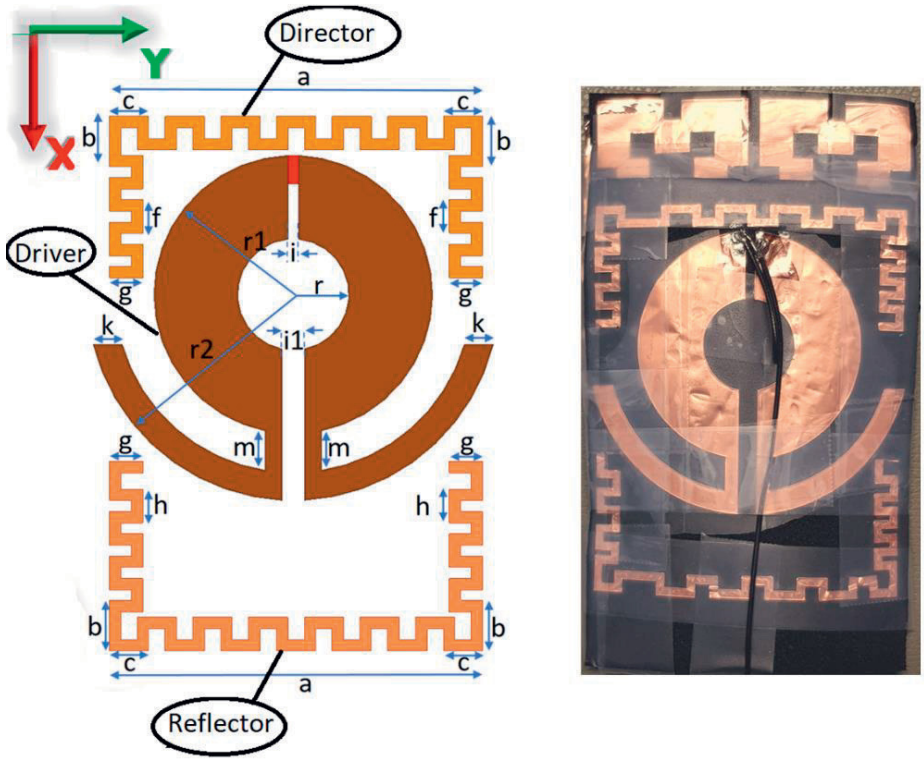

Figure 33. Antenna configuration with the geometrical parameters reported in millimeters (left side) and the fabricated antenna (right side) [Publication IV].

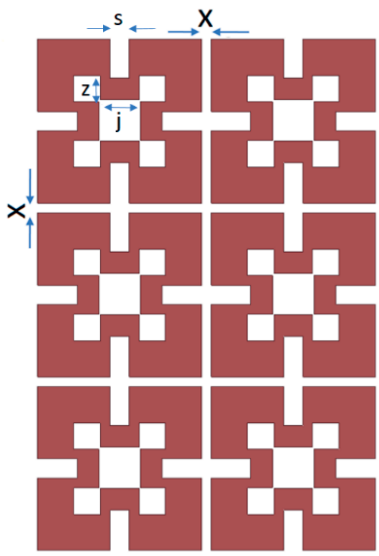

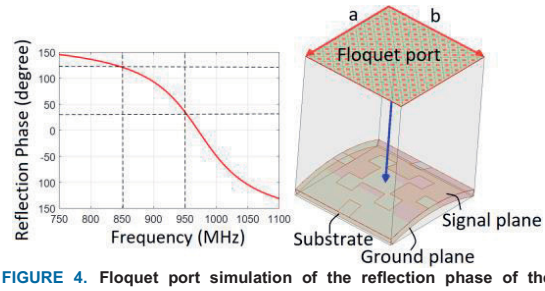

FIGURE 4. Floquet port simulation of the reflection phase of the

Figure 34. Reflection phase (left side), Floquet port simulation (middle), and periodic surface (right side) [Publication IV].

To obtain the operating frequency at 915 MHz, we folded the proposed unit cell from the initial design [129] to increase the electrical length, leading to a decrease in operating frequency, as shown in the right side of Figure 34. After that, to fit the total size of the quasi-Yagi antenna, we organized the unit cell to be 2-by-3 elements to shape the periodic surface. After optimizing the configuration of the quasi-Yagi antenna and the periodic surface, we set up the antenna on the forearm model, as in Figure 35. The homogenous forearm model is the simplification cylinder comprising skin with a radius of 46 mm and a length of 250 mm which is the closest tissue to the antenna and among the most EM power distortion materials ($\sigma = 0.855$ S/m and $\varepsilon_r = 41.85$ at 915 MHz) [103]. The structure of the antenna with 5 layers is also shown in Figure 35. with the exploded view. The first layer is the radiating plane made by the flexible copper foil with 35 μm thickness. The overall size of the antenna is $0.22\lambda \times 0.33\lambda$. The next layer is the proposed periodic surface isolated to the radiating plane and ground plane by the EPDM substrate. The last layer is the ground plane, which significantly minimizes the interaction of skin on the EM wave propagation.

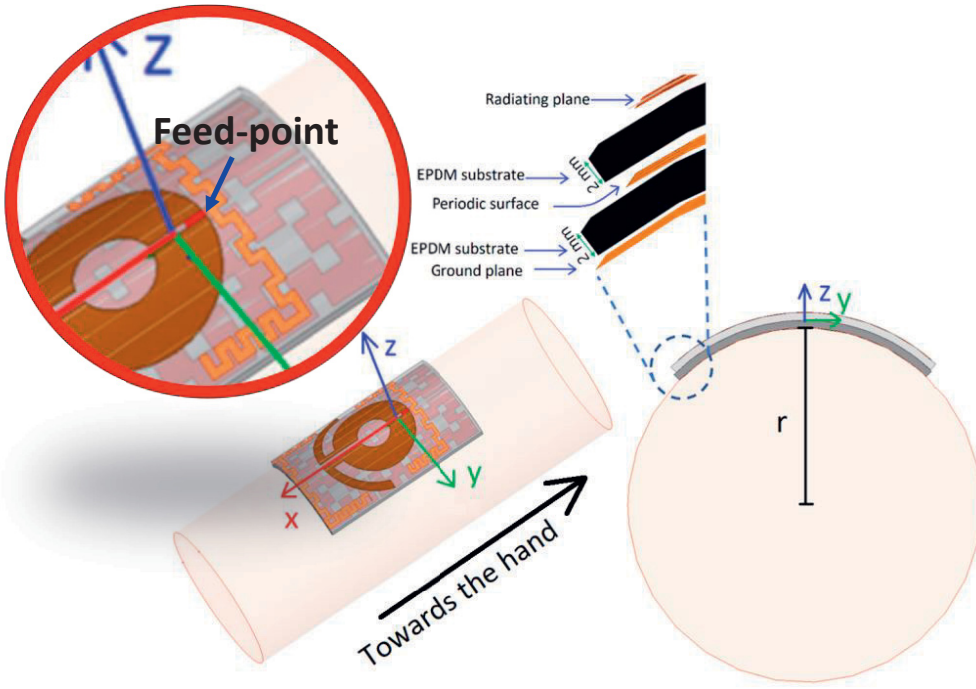

Figure 35. Wearable quasi-Yagi antenna attached to the forearm model (left side) and the exploded view of the antenna (right side) [Publication IV].

4.4.2 Evaluation of the Proposed Antenna Development Method

Simulation results

In this research, we co-optimize the radiating plane of the quasi-Yagi antenna and the periodic surface geometry to obtain the end-fire radiation pattern with the peak directivity toward the forearm and the impedance matching with 50 Ω input source at 915 MHz. The stable reflection coefficient or S_{11} of the quasi-Yagi antenna mounted on different forearm radius, 37.5 mm, 46 mm, and 55 mm, is demonstrated in Figure 36. Although the antenna geometry undergoes various transformations, the S_{11} maintains lower −10 dB at around 915 MHz. Interestingly, when the antenna is formed with 37.5 mm and 55 mm cylindrical radii, it shows a dual-band type of S11 response with a broader bandwidth compared with the nominal case of the 46 mm. It therefore maintains good impedance matching at 915 MHz also with different curvature radii.

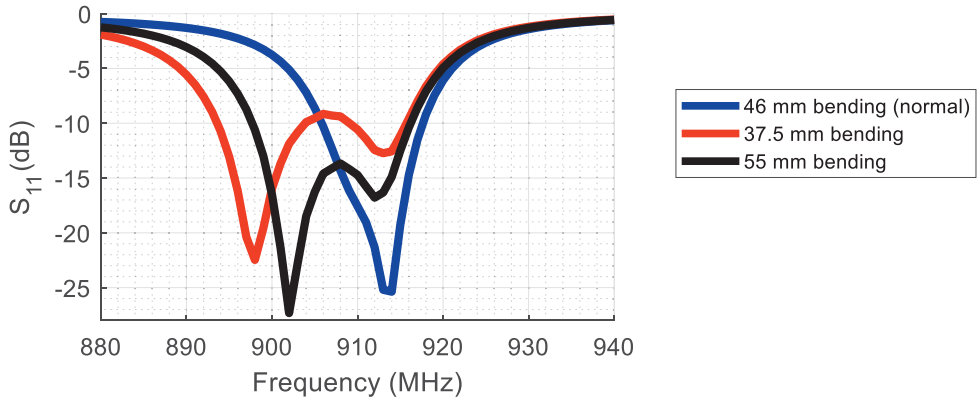

Figure 36. Reflection coefficient of antenna with different levels of bending [Publication IV].

The index $\Delta_{dir} = D_{arm} / D_{peak}$ is used to validate how close the antenna directivity in the direction forward D_{arm} from the forearm to the peak directivity of the antenna D_{peak}. The values of Δ_{dir} and D_{peak} in XZ and XY plane are shown in Figure 37. (a) and (b) with a comparison between the two cases, with and without the periodic surface. We expect to achieve as high D_{peak} as possible with Δ_{dir} close to 1. It can be seen that the peak of directivity and the Δ_{dir} reach the highest value at 915 MHz when the antenna attached to the periodic surface. In contrast, without a periodic surface, the peak of D_{peak} and Δ_{dir} are tending toward local minima near the targeted 915 MHz UHF RFID band. In Figure 37. (b), with the periodic surface, the gain of the quasi-Yagi antenna can improve to -5.1 dBi in the forearm direction. In the simulation results, we show the ratio of the gain Δ_{gain} in front of the quasi-Yagi antenna G_{front} ($\theta = 90°$, $\varphi = 180°$) and the backside G_{back} ($\theta = 90°$, $\varphi = 0°$), as in Figure 37. (c). At 915 MHz, Δ_{gain} obtains 5 dBi at 915 MHz.

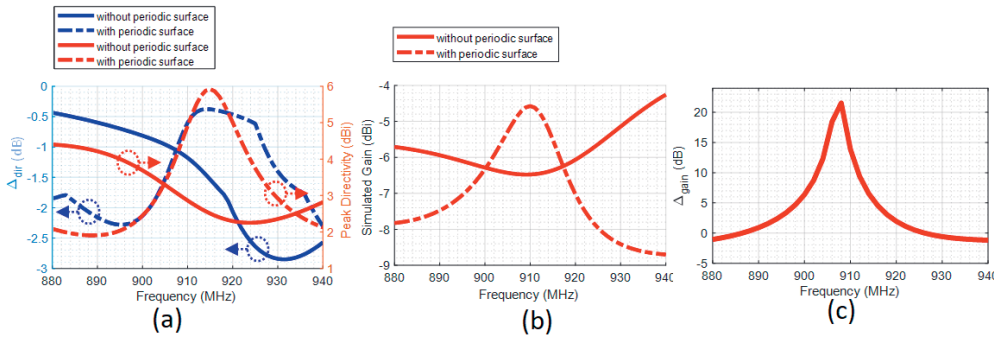

Figure 37. Peak directivity and delta (a), the antenna gain (b) and front-to-back ratio of the main and back lobes (c) [Publication IV].

The quasi-Yagi antenna's 3D directivity directive radiation pattern can be showed along the forearm (−X direction) in Figure 38. (c) with the peak directivity of −5.4 dBi. The 2D directivity pattern of the forearm reader antenna in the XZ and XY planes is shown in Figure 38. (a) and (b), respectively. We also consider the bending of the antenna with different radii to validate the antenna performance stability with different forearm sizes. Overall, the bending has insignificant impacts on the antenna properties, either in peak directivity or the reflection phase. However, it improves the end-fire radiation pattern by remarkably minimizing the back lope.

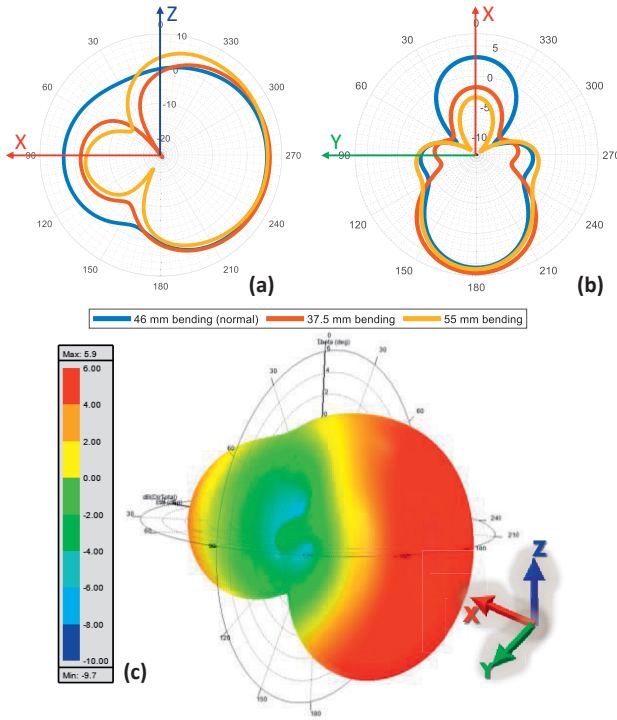

Figure 38. Directivity pattern in XZ (a), in XY plane (b), and 3D directivity pattern of the quasi-Yagi antenna [Publication IV].

In the wearable antenna development, the specific absorption (SAR) level should conform to the regulation of the US FCC, limiting the SAR to 1.6 W/kg averaged over 1 g of tissues. Transmission power ($P_{t,max}$) for the quasi-Yagi antenna is determined according to the maximum SAR as [137]

$$P_{t,max} = \frac{1.6\,W/kg\,(1-|S_{11}|^2)P_{test}}{SAR_{max}}, \tag{4.1}$$

where P_{test} is the available power from the test source, which we set to 1 W. The simulation results show that the maximum power that can transfer from the source is 41.2 dBm with the maximum SAR of 0.9 W/kg along with the tissue close to the antenna. In the RFID systems, the maximum power that we can transmit is 40.6 dBm with EIRP = 3.28 W, which is approximate to the limitation of SAR. Nevertheless, this output power should be lower to be suitable for the RFID reader components. In this research, we set the output power from the reader to 32 dBm. When we feed 1 W to the source and apply the periodic surface, the current distribution of the quasi-Yagi antenna concentrates at the director and reaches the peak at 49 A/m, as shown in Figure 39. . On the other hand, the current density permeates all antenna elements if we remove the periodic surface.

Figure 39. Current distribution of the quasi-Yagi antenna with and without periodic surface [Publication IV].

Measurement setup and results

In the beginning, since the measured impedance of the forearm reader antenna (8 + 9*j* Ω) mismatches the 50 Ω input port, as in the right side of Figure 40. , the power efficiency between the input source and the antenna cannot maximize at 915 MHz. To solve that issue, we applied the coaxial cable balun and impedance matching

between the forearm antenna and the input source, as shown in the lower right corner of Figure 42. (b). Firstly, the balun transforms the current mode of the driven element (balanced) of the quasi-Yagi antenna to a typical dipole antenna (unbalanced) [103]. Secondly, we constructed the impedance matching circuit with an L-matching configuration consisting of a parallel capacitor (10 pF) and a series capacitor (25 pF), as shown in Figure 40. That converts the original impedance of the antenna to 50 **Ω**, leading to a significant improvement in the antenna reflection coefficient at 915 MHz, as in Figure 41.

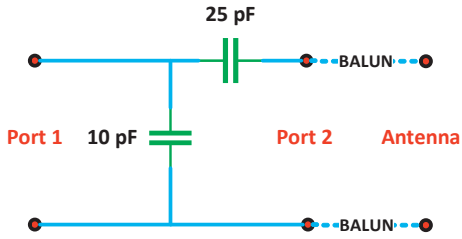

Figure 40. The impedance matching circuit and balun [Publication IV].

One of the most critical parameters of the forearm reader antenna is realized gain G_R, whose measurement setup is shown in Figure 42. (b). Unlike typical antenna measurement, we adopt the alternative approach for the wearable UHF RFID reader antenna attached on the body surface by applying a classical far-field antenna measurement with the analogous distance between the reference gain antenna and test RFID tag. The test UHF RFID tag is designed as Figure 42. (a), and its target is to reach the highest level of the realized gain ($G_{r,tag}$) at 915 MHz, as in Figure 41.

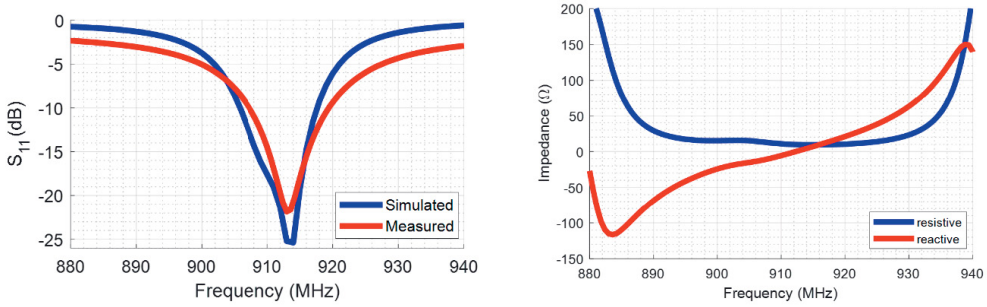

Figure 41. Reflection coefficient and input impedance of the antenna [Publication IV].

Figure 42. (b) shows that the wearable quasi-Yagi antenna was directly attached to the forearm of the wearer and pointed to the test RFID tag, consistent with the simulation scenario. The distance S between the reader antenna and RFID tag of 1 meter is inside of the far-field region. The threshold power of the test RFID tag (P_{rx}) was recorded by the RFID measurement Voyantic Tagformance system by the

forearm reader. This procedure assists in obtaining the realized gain of the antenna (G_R)

$$P_{rx} = G_R G_{r,tag} L_{cab} \left(\frac{\lambda}{4\pi s}\right)^2 P_{tx}, \tag{4.2}$$

where $L_{cab} = -1.1$ dB is the power loss factor of the cable connected from the antenna to the Tagformance reader, and P_{tx} is the transmission power from the reader. We compute the simulated realized gain by equation (4.3) and compare it with the measured realized gain.

$$G_R = G(1 - |s_{11}|^2), \tag{4.3}$$

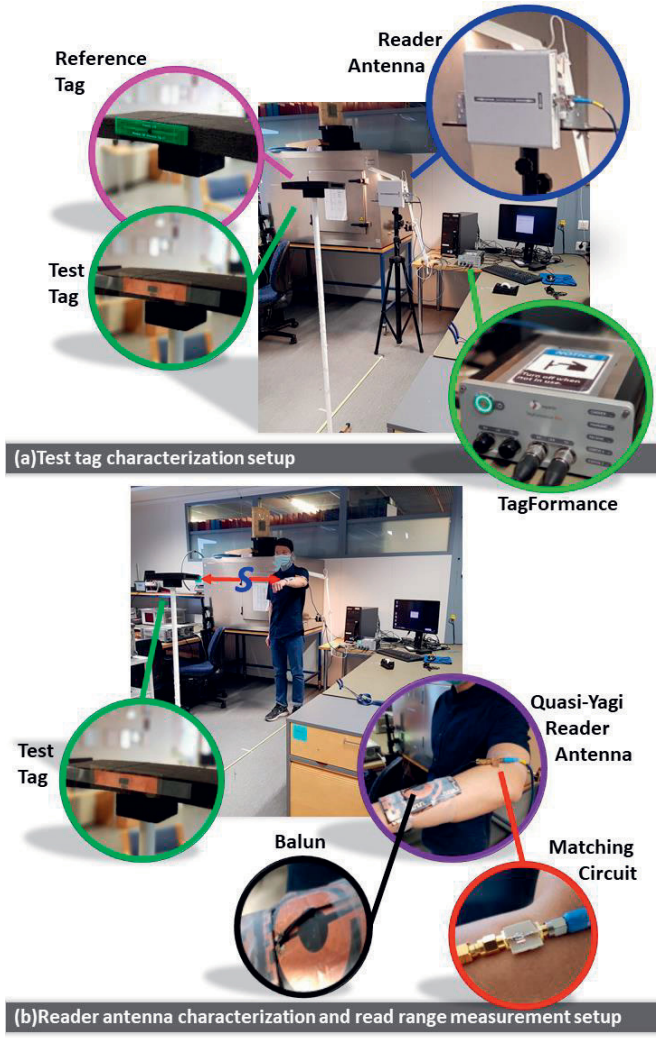

Figure 42. Measurement installation of the test tag and reader antenna gain [Publication IV].

Overall, the result in Figure 43. shows a good correlation of the increasing trend of the measured and simulated read range of the RFID tag. The constant relative difference of the read range level of 150 cm at 32 dBm because of realized gains of the tag and reader antennas is lower than those in the simulation.

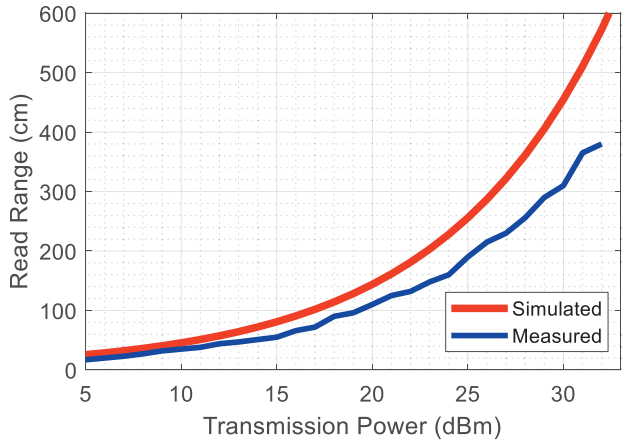

Figure 43. Read range of the RFID test tag [Publication IV].

The acceptable compliance between the simulation and measurement realized gain of the forearm reader antenna with the peak of −4.7 dBi at 910 MHz and −5.5 dBi at 915 MHz, as in Figure 44. Next, we adjust the distance between the reader and the RFID tag and continuously capture the response signal from the tag to measure the detection range of the RFID tag versus the variation of the transmission power of the reader.

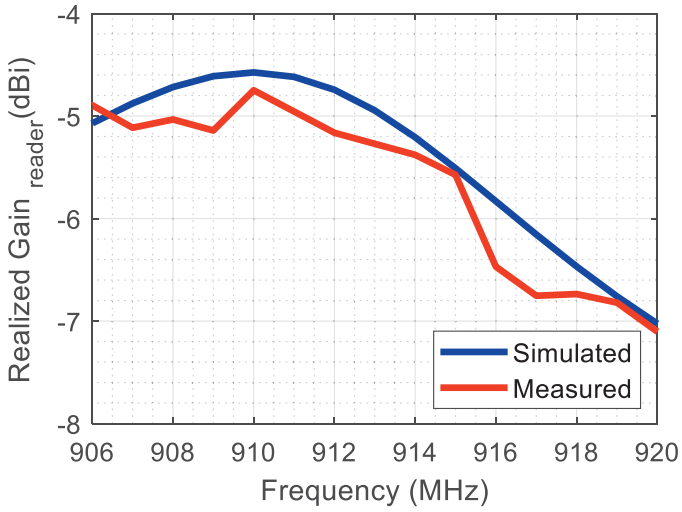

Figure 44. Realized gain of the forearm RFID reader antenna [Publication IV].

Through mindful co-optimization for the antenna signal plane and the periodic surface geometry, our proposed metasurface-enabled quasi-Yagi UHF RFID reader antenna can provide the end-fire radiation pattern with a directivity of 5.5 dBi in the pointing direction of the forearm. The antenna's ground plane decouples the antenna radiation and the human tissue and reduces the SAR value. In the office measurement environment, the forearm RFID reader antenna can detect the tag in an acceptable range of 3.8 meters by setting up the output power of the reader of 32 dBm (EIRP = 0.56 W) at 915 MHz.

Table VI summarizes and compares the performance of the contemporary antennas and the those of the proposed antenna. It is noted that we computed the detection range of RFID reader antenna with 25 dBm input power. We classified the antennas based on the pattern configurations as Type 1 and Type 2 which are a long body surface and off body direction, respectively. Although the antennas from research [131][132][133][152] provide high read range, our proposed antenna possesses highest read range among antennas type 2. However, the antenna [132] was originally developed to operate at 2.47 GHz which is not appropriate to RFID reader. Hence, its hypothetical read range is impacted by shorter wavelength.

TABLE VI

COMPARISON WITH THE CONTEMPORARY RESEARCH WORK

Ref.	Freq. (GHz)	Gain (dBi)	Size (mm)	Thickness (mm)	Relative size	Read range (m)*	RFID reader	Pattern type
[24][129]	0.866	4	80×62	4	0.23×0.18 λ_o	1.5	Yes	1
[130]	0.866	2	80×70	1.52	0.23×0.20 λ_o	1.45	Yes	2
[134]	0.880	5	63×65	--	0.18×0.19 λ_o	2	Yes	1
[131]	0.866	1.31	140×100	4	0.40×0.29 λ_o	2.3	Yes	1
[152]	0.915	10.9	360×360	5	1.19×1.1 λ_o	2.1	No	1
[44]	2.47	0.1	50×50	9.5	0.41×0.41 λ_o	1.29	No	2
[132]	0.860	1	90×49	4	0.25×0.14 λ_o	4.23	No	1
[133]	0.868	2.6	87×77	4	0.25×0.22 λ_o	2.76	No	1
Our work	0.915	5.5	67×108	4	0.20×0.33 λ_o	2	Yes	2

*Estimated read ranges (S_{max}) based on the test tag used in our work (P_{tc} = −18 dBm) and calculated by equation (5) assuming P_{tx} = 25 dBm.

4.5 Wearable Passive UHF RFID Tag with Circular Polarization

Recently, the industrial RFID system was deployed for a wide range of applications, such as access control, identification, item-level tracking, and wearable and implantable devices [138][139][140]. In these RFID systems, the linear polarization with single-layer dipole configuration is commonly used due to available miniaturization methods and mass production cost saving [141]-[143]. To improve the tag performance, much research has studied the circular polarization (CP) tag antenna since it can avoid cross-polarization and enhance the polarization efficiency [144]-[147]. However, the single-layer antenna configuration cannot avoid coupling between the antenna radiation and body surface; hence, the antenna structure with ground plane and the metallic coupling structures are preferred. This approach has been utilized to develop the 50 Ω wearable CP antennas for the GPS, 2.4 GHz ISM band applications, and UHF RFID [148]-[150]. Recently, the research related to the optimization for the CP antenna has attracted attention [151].

This research introduces the development of the small passive UHF RFID tag with the circular polarization based on the microstrip patch antenna configuration with all corners truncated. That approach significantly improves the power transmission efficiency and detection reliability between the RFID tag and reader. In terms of the antenna structure, the antenna was tuned by the combination of truncated corners and cross-and L-slots to maximize the read range and minimize the axial ratio at the operating frequency. The antenna substrate and conductor were fabricated by flexible and lightweight material to ensure comfort for the wearer. There are two versions of the CP patch UHF RFID tag antennas. The first antenna version applied the extra inducted loop to obtain the best impedance matching between the RFID IC and the antenna. The second version of the CP patch tag antenna was optimized for wearable applications without the matching loop. We directly tuned the input impedance of the antenna by the truncated corners and the size of the signal plane.

4.5.1 Antenna configuration and body model

4.5.1.1 Circularly polarized corner-truncated and slotted microstrip patch antenna with inductive matching loop

The CP patch antenna for the RFID tag was developed in the full-wave electromagnetic field solver HFSS (ANSYS High-Frequency Structure Simulator) based on the finite element method. The geometry of the proposed antenna is inspired by the compact circularly polarized square microstrip antenna introduced in [153], which comprises three layers: the radiating plane, substrate, and the ground

plane, shown in Figure 46. To obtain the circular polarization, we applied the truncated corners at the edges of the antenna signal plane as in Figure 45. [154], and the variation of its size determines the handedness of the circularly polarization [155][156]. In this research, the truncated corners are optimized to be symmetric and assist the antenna in aiming toward right-hand circular polarization. The antenna miniaturization is solely achieved thanks to the hexagonal slots and L-slots in the signal plane [157]. The main idea of these slots is to alter the current density of the radiating plane, leading to the modification of the effective capacitance and inductance of the antenna.

The total size of the proposed patch RFID tag antenna is 50 mm by 50 mm by 4 mm ($0.1525\ \lambda_0 \times 0.1525\ \lambda_0 \times 0.0091\ \lambda_0$, where λ_0 is the wavelength at the center frequency of 0.915 GHz); hence, it fits in various body areas, such as the back, upper arm, and thigh.

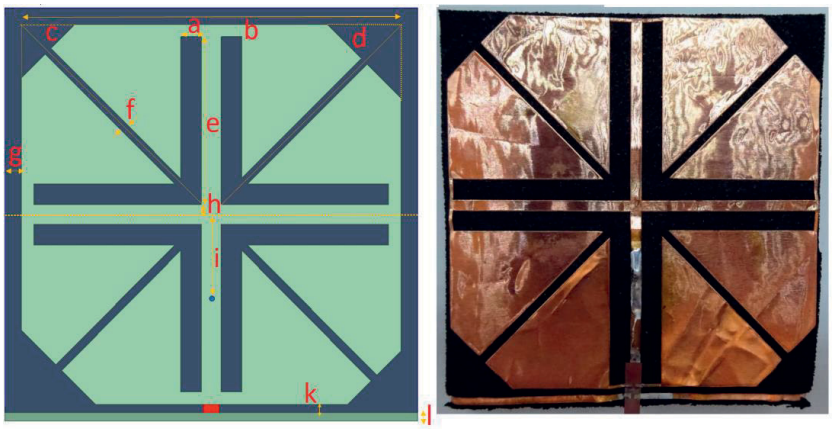

a	b	c	d	e	f	g	h	i	k	l
2.5	46	6	9	21	1.5	2	1	9	1	1

Figure 45. Antenna geometry and dimension of antenna reported in millimetres [Publication V].

The complex conjugate impedance matching between the antenna and RFID IC was obtained by combining the inductive feeding network technique motivated by the previous study of the mountable metal tag [158] and the short pin connecting the radiating and ground plane. Consistent with the quasi-Yagi antenna tag in Subsection 4.3, we mounted the (NXP UCODE G2iL; turn-on power −18 dBm) at the feeding point. The frequency-dependent impedance for the RFID IC is modelled as the equivalent parallel connection of the resistance R = 2850 Ω and capacitance C = 0.91 pF.

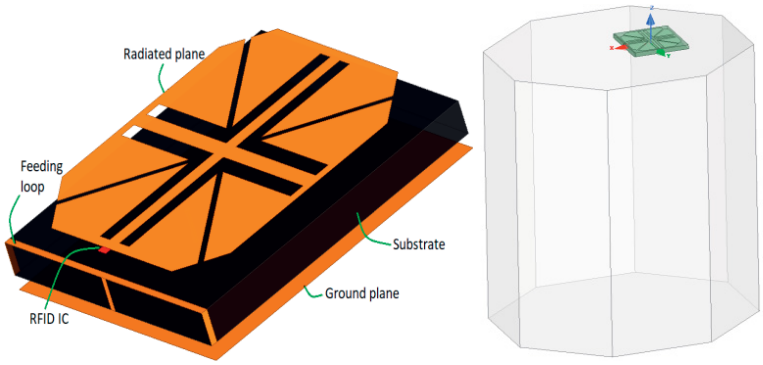

Figure 46. Exploded view of the CP patch antenna and the simplified human model [Publication V].

To evaluate the antenna performance on the body surface in the simulation, we employed the simplified polygonal cylinder with the skin, which is the main material (ε_r = 41.6, σ = 0.86 S/m). Then, the antenna is installed on the body model demonstrated on the right side of Figure 46.

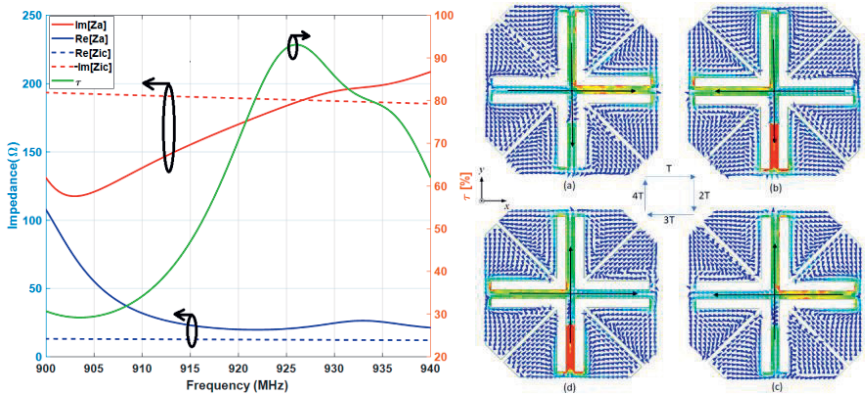

Figure 47. Input impedance and antenna-IC power transfer efficiency (left side) and the current distribution of the antenna at various phases (a) Phase = 10°, (b) Phase = 100°, (c) Phase =190°, (d) Phase = 280° at 932 MHz (right side) [Publication V].

The comparison of the RFID tag antenna with RFID IC and the power transfer efficiency is demonstrated in Figure 47. Thanks to the cautious tuning of the antenna elements, such as the short pin position and the inductive feeding loop, the best matching between IC and antenna can be obtained from 925 MHz to 932 MHz. This good impedance matching leads to the high-efficiency power transmission between the antenna and RFID IC at above 80%. Figure 47. also illustrates the current flow on the antenna surface at the lowest axial ratio frequency 932 MHz at a different phase, 10°, 100°, 190°, 280°. The handedness of the antenna polarization is right-

hand, and the current confirms that statement in the middle of the circular counterclockwise antenna rotation.

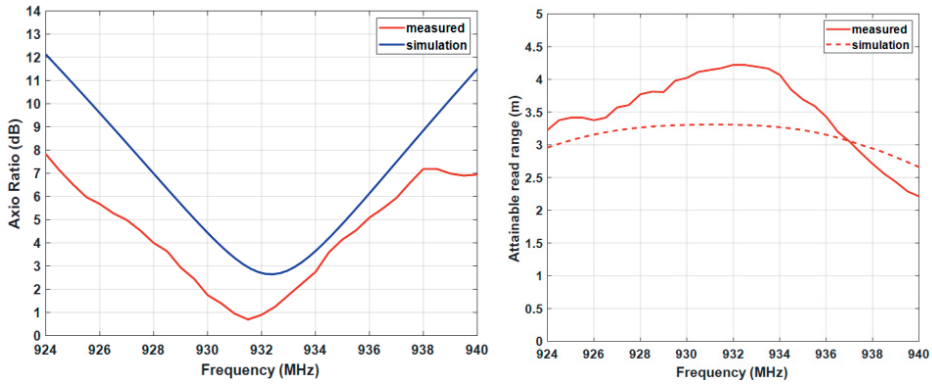

Figure 48. Axial ratio (left side) and the read range (right side) of the CP patch RFID tag [Publication V].

The measured axial ratio hits the lowest point of 0.7 dB at 932 MHz; meanwhile, the lowest value simulated axial ratio is 2.8 dB at 933 MHz, as Figure 48. The bandwidths of the simulated and measured AR are 5 MHz and 0.5 MHz, respectively. The differences between both results likely originates from the movement of the body during measurement.

4.5.1.2 A small circularly polarized microstrip patch antenna with truncated corners

This section introduces an upgraded version of the circularly polarized microstrip patch antenna that includes the simplified antenna signal plane and the operating frequency at the exact 915 MHz inner UHF RFID frequency band. We have used the simplified cuboid-shaped and anatomical human body models to provide higher accuracy antenna performance estimations in the simulation. We simplified the antenna geometry by completely removing the inductive feeding loop and tuning the impedance directly from the size of the truncated corner and short pin position. Furthermore, the robustness of antenna performance is evaluated by measuring the read range and AR at various body positions and different cloth thicknesses.

The cross- and the front views of the antenna with geometrical parameters reported in millimetres are shown in Figure 49. For the antenna resonance frequency at 915 MHz, we tuned the L slots length; the longer the slots, the lower the resonance frequency. This optimization technique was inspired by [159] for the 50 Ω two-corner truncated patch on the high relative permittivity laminate superstrate to obtain the resonance frequency at a lower frequency band. However, the drawback of this technique is that it significantly reduces the radiation efficiency, gain of the

antenna, and read range of the tag. In terms of AR optimization, we transformed the symmetrical corners to asymmetrical corners, balancing the low AR and high radiation efficiency for the antenna.

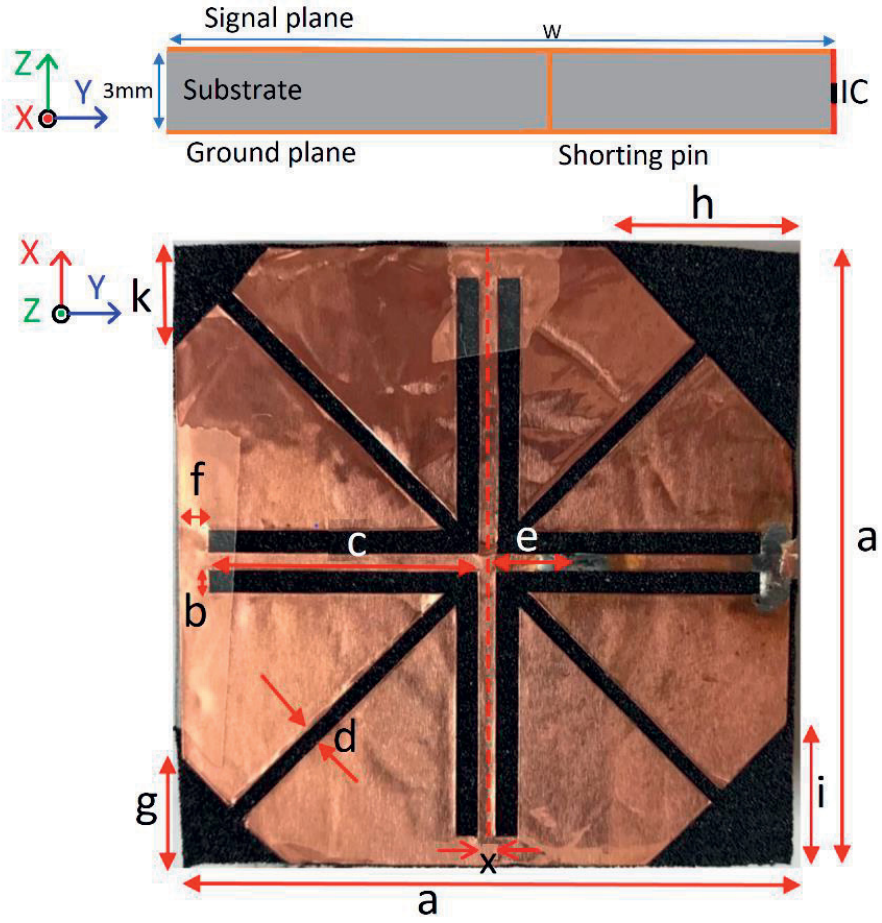

Figure 49. Cross- and front views of the CP patch antenna with the dimension in details [Publication VI].

The antenna performance is precisely evaluated by the anatomical and cuboid models with dielectric properties of the skin, as illustrated in Figure 50. First, the simplified cuboid shape is utilized to optimize the antenna's radiating properties, such as the read range, directivity, radiation efficiency, and axial ratio because it has a lower time and computer resource consumption. Then, the anatomical model verifies the outcome. Although the minor difference between the anatomical and simplified models is shown in Figure 51. , both models provide the highest power transmission efficiency of 98% between the antenna and RFID IC at 912 MHz, and the good impedance matching is achieved from 908 to 924 MHz in the range of

UHF RFID. The simulated current distribution of the CP patch antenna with the cuboid model at different feeding phases of 0°, 90°, 180°, and 270° at 915 MHz is depicted in Figure 52. The CP patch antenna maintains right-hand circularized polarization with the counterclockwise rotation of the current vectors at the cross-section in the z-direction [160]. According to the 2D directivity pattern, in the xz plane, the peak directivity of 6.7 dBi occurs at $\theta = 20°$ for the simplified cuboid model, and 5.4 dBi occurs $\theta = 15°$ for the anatomical model.

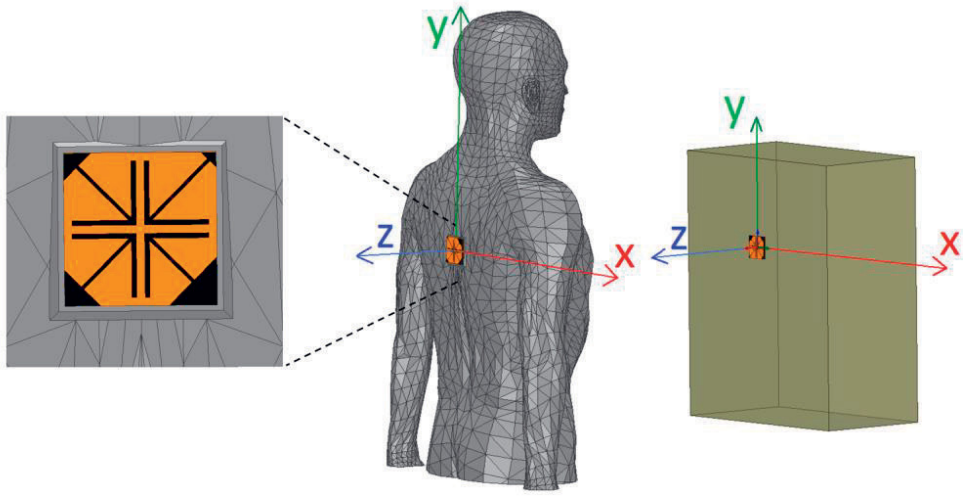

Figure 50. An antenna attached to the anatomical model (left) and simplified cuboid model (right) [Publication VI].

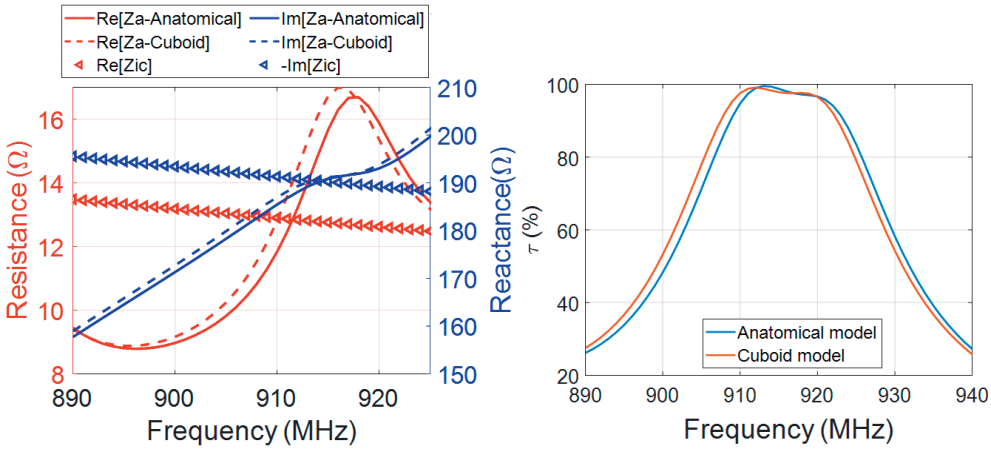

Figure 51. Complex impedance of antenna with anatomical and cuboid models (left side) and the power transmission efficiency (right side) of the CP patch RFID tag [Publication VI].

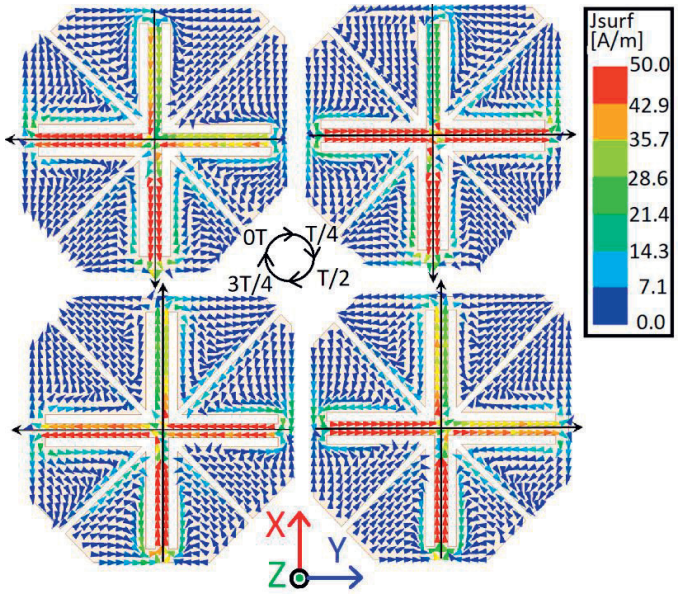

Figure 52. The current distribution on the signal plane of the CP patch antenna.

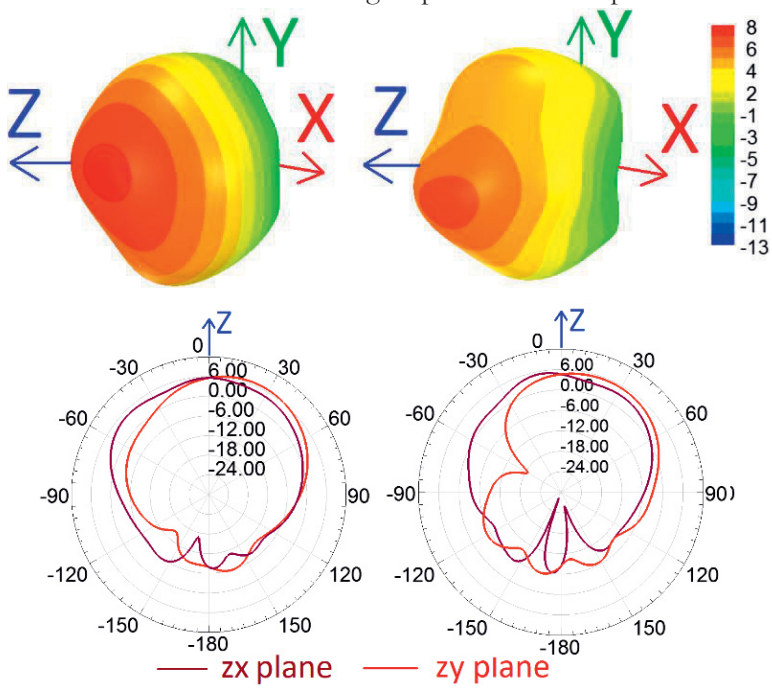

Figure 53. 3D (upper side) and 2D (lower side) directivity radiation pattern of the CP patch tag antenna [Publication VI].

The beam width of the directivity pattern of the antenna with the cuboid model is 76° and 118° in the xz and yz planes. The realistic anatomical model provides a corresponding value of 78° and 81° xz and yz planes. Overall, the estimation

difference of antenna impedance and radiation properties from both body models is slight. The coverage of the proposed tag in Figure 54. shows that when $\alpha \geq 0.4$, both models provide a similar read range prediction at the considered observation angles. For $\alpha = 0.5$, with consistent read range coverage estimation, we can conclude that the probability of obtaining a read range of longer than 2.3 meters is 50% with the RHCP reader.

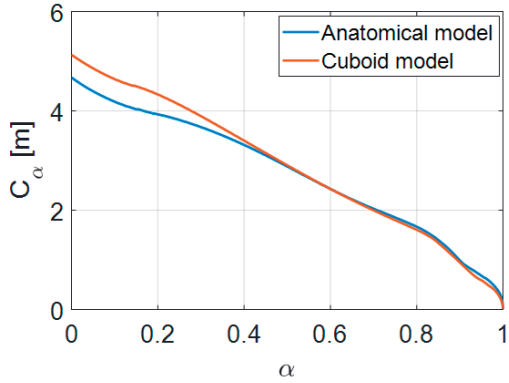

Figure 54. Read range coverage of the CP patch antenna tag at 915 MHz where θ = –90°…90° and φ = 0°…180° [Publication VI].

As described above, the performance of the proposed tag was measured on various parts of the body, such as the upper back, arm, leg, thigh, as well as on the winter coat. The axial ratio of the proposed CP tag is presented in Figure 55. With the first sample of the tag, the tag-operating frequency shifted downward compared to those of simulation. We applied the post-manufacturing method to tune the minimum axial ratio frequency to a closer expected frequency of 915 MHz to handle that issue. In particular, we increased the length of the L-slots from 2.6 mm to 3 mm to adjust the operating frequency from 897 MHz to 917 MHz with a minimum AR of 2.1 dB.

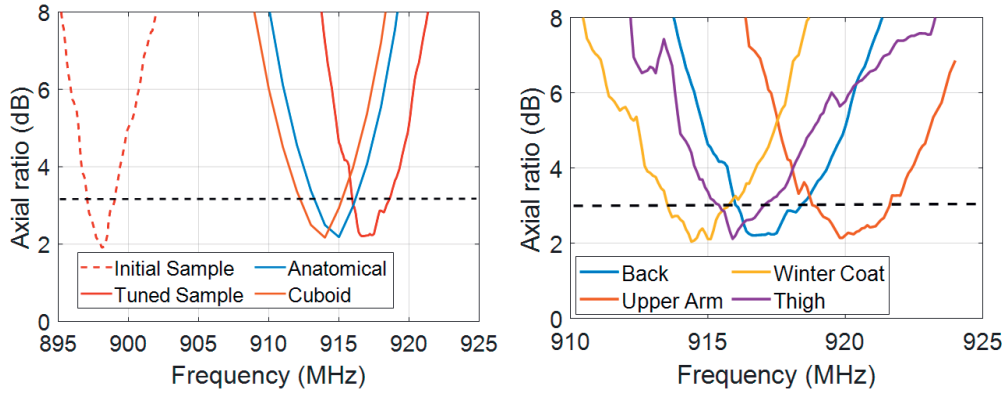

Figure 55. Comparison of simulated and measured AR (left side) and measured AR at various positions of the body [Publication VI].

In other testing scenarios, although there is a variation in the 3 dB AR frequency, the maximum frequency shift in the axial ratio was only 5 MHz. The read range of the tag from the numerical model and measurement is shown in Figure 56. The simulated read range at the z-axis direction varies from 4 m to 4.5 m, and the peak read range is 4.5 m and 5.2 m for anatomical and simplified models, respectively.

In the z-direction, the read range of the antenna is 5.8 m when attached to the back with a T-shirt. The read range levels show a small fluctuation from 5.5 m to 6 m in four different body-worn measurement configurations. It confirms that although the antenna is rigorously optimized on the optimal position of the upper back, it maintains the stability of the performance on other parts of the human body. That is an important aspect of the wearable application.

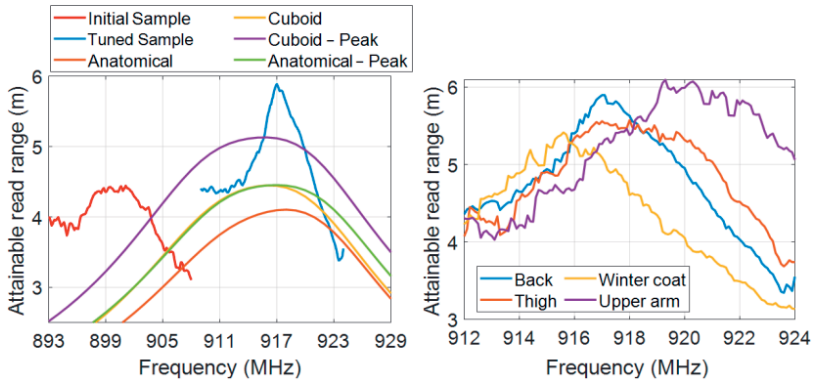

Figure 56. Comparison of the simulated and measured read range (left side) and the measured read range of the tag at various positions of the body (right side) [Publication VI].

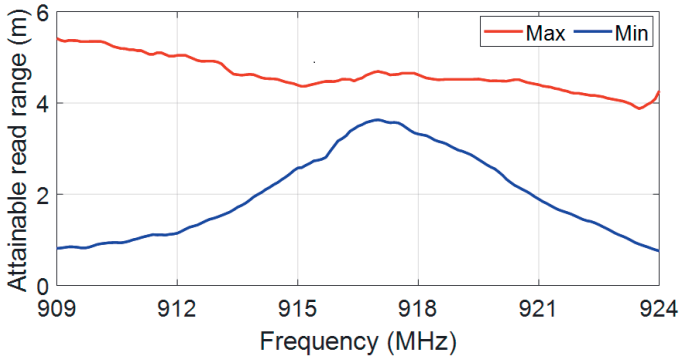

Figure 57. The measured read range of the tag when the reader antenna is a linear polarization [Publication VI].

When the read antenna is a linear polarization configuration, the read antenna fluctuates, corresponding to the polarization efficiency between the tag antenna and the reader antenna. In this case, we defined the read range d_{tag} of the tag in the range

from the minimum and maximum read range that correlates with the minimum (Γ_{-LIN}) and maximum (Γ_{+LIN}) polarization efficiency. Thus, as illustrated in Figure 57. , even the RFID system employs the linear polarization reader antenna, and the system can detect the tag with a reasonable range from 3.8 m to 4.5 m at 917 MHz. The measurement and simulation results validate the robustness and good detection reliability of the proposed RFID CP tag. The antenna features a high read range and

TABLE VII

COMPARISON WITH THE CONTEMPORARY RESEARCH WORK

Ref.	Antenna type	Gain (dBi)	Relative size	Read range (m)	Wearable application
[144]	Dipole	N/A	$0.1\times0.1\times0.001\ \lambda_0$	7	No
[167]	Patch	-7	$0.25\times0.25\times0.004\ \lambda_0$	2.8	No
[166]	Patch	N/A	$0.45\times0.45\times0.015\ \lambda_0$	8.4	Yes
[168]	Split ring	-9.6	$0.15\times0.15\times0.01\ \lambda_0$	2	Yes
[169]	Dipole on AMC	5	$0.78\times0.78\times0.0183\ \lambda_0$	15.7	Yes
Our work	Patch	-7	$0.15\times0.15\times0.012\ \lambda_0$	5.8	Yes

low axial ratio in the body-worn configuration at 915 MHz. The simulation results show that the antenna possesses broad beamwidth with a peak of 5 dBi, which allows good detection when the tag is not perfectly aligned to the reader. Finally, the antenna has a compact size of 5-by-5 cm on a low-permittivity textile substrate that enables seamless cloth integration.

Table VII demonstrates the comparison between our proposed antenna and those from previous research on the circularly polarized passive UHF RFID tags. The antenna gain and read range of the antenna of research, [166]and[169] are notably greater than our research work. Nevertheless, the size of those antennas is dramatically large to attach on some part of body such as upper arm and thigh, hence, it is only wearable at the front or back of the torso. Besides, the footprint of the presented antenna in research [144] and [168] is compatible to our research. However, these antennas were originally developed with single layer, hence, the performance of them is highly sensitive to the human tissue when attached on body surface. Overall, comparing previous research, our proposed antenna provides a favorable balance between performance and the size which is compact enough to be worn at different areas of body.

5 CONCLUSIONS

The major challenge in the broad deployment of wireless body area networks in medical practice is the difficulty of obtaining efficient and reliable body wireless links. To address this challenge, we concentrate on developing the most important part of the personal wireless communication system: the wearable antenna in this thesis.

Due to the absence of knowledge of textile material electrical properties for wearable antenna development, we introduced a novel characterization method for the textile method based on the fitting model with high accuracy and simplification of the data processing [Publication I]. Our strategy extracted the relative permittivity and loss tangent of the substrate and conductivity of the textile conductor from the best fit data of the maximum transducer gain by the least square estimation sense. The validation with the textile passive low-pass RF filters confirmed the applicability of our textile characterization method to the wireless communication circuit development.

In the next phase of research, a variety of antenna optimization approaches were proposed to fulfil the on-body wireless communication requirements based on the far-field UHF RFID system [Publication II]–[Publication VI]. Firstly, a low-profile headgear antenna on a periodic surface with high directivity and end-fire beam along the head's surface has been developed for the UHF RFID tag. According to the on-body measurement of the antenna prototype, our proposed tag antenna with quasi-Yagi configuration facilitates the high read range of 6 meters forward from the user's head. Interestingly, we utilized the reflector as another dipole with a broadside radiation pattern and a good detection range of 5 meters above the user's head. Hence, in one antenna platform, we can achieve a dual-ID RFID tag.

The wearable forearm RFID reader antenna has been optimized for biomedical application [Publication IV]. Thanks to folding and meandering techniques, the proposed antenna maintained a small footprint of only 67 mm × 95 mm × 5 mm with flexible and lightweight materials that provide comfort to the users. The unexpected interaction of the human tissue on the antenna radiation and SAR level

was significantly reduced by the presence of the periodic surface made of a 2-by-3 grid of unit cells with the ground plane. In the practical testing, we are able to detect the passive UHF RFID tag in the range of 3.8 meters with the reader's output power of 32 dBm (EIRP = 0.56 W) at 915 MHz.

At the final stage of the research, we introduced a circular polarization RFID tag antenna with a small dimension of only 50 mm × 50 mm × 4 mm for wearable applications [Publication V] and [Publication VI]. The signal plane of the antenna is

shaped by the four truncated corners and the L-and cross-slots, providing a low axial ratio and a high read range of 915 MHz. In the wireless measurement with the on-body condition, the proposed antenna provided a read range of above 5 meters and the axial ratio of 2 dB at the UHF RFID frequency band. The antenna radiation pattern is orthogonal to the body surface with a directivity of 6.7 dBi. According to the coverage analysis, there is a 50% probability that the antenna tag can be detected by the reader within the detection range of 2.3 meters.

To summarize, this research has provided novel approaches for improving the wearable designs and added value to further on-body wireless communication system development. The simulation and experiments of the antenna in this thesis have proved that there is a great possibility of employing the wearable textile antenna with multiple features on the body to replace the conventional rigid antennas in several applications in daily life.

5.1 Future Work and Perspectives

In the development of the textile material characterization, the improvement can be considered by employing multiple transmission lines. This approach reduces the errors from fabrication and increases the accuracy of the characterization outcomes. Besides, the electrical line-to-connector transition between the connector and the beginning of the transmission line should be considered to reduce the uncertainty. For the headgear and forearm antenna, developing more compact structures for the modern on-body system cannot be ignored. If the antenna's periodic surface and the signal plane are investigated further, the total size of the antenna is reduced. Besides, the antenna can be possessed in the circular polarization configuration to reduce the polarization mismatch. Although the CP patch antenna shows superiority in the antenna footprint and good detection range, the antenna should be equipped with an omnidirectional radiation pattern along the body surface, which would extend its use to on-body communications.

REFERENCES

[1] S. C. Mukhopadhyay, *Wearable Electronics Sensors: For Safe and Healthy Living*, vol. 15, Springer, 2015.

[2] A. Sabban, *Wideband RF Technologies and Antennas in Microwave Frequencies*, John Wiley & Sons, 2016.

[3] A. Sabban, *Low-visibility Antennas for Communication Systems*, CRC Press, 2015.

[4] A. Bonfiglio, and De Rossi, D. (Eds.). (2010). Wearable Monitoring Systems. Springer Science & Business Media.

[5] S. Movassaghi, M. Abolhasan, J. Lipman, D. Smith, and A. Jamalipour, "Wireless body area networks: A survey," *IEEE Commun. Surveys Tut.*, vol. 16, no. 3, pp. 1658–1686, 2014.

[6] J. A. Tsolis, W. Whittow, A. Alexandridis, and J. Vardaxoglou, "Embroidery and related manufacturing techniques for wearable antennas: Challenges and opportunities," *Electronics*, vol. 3, no. 2, pp. 314–338, May 2014.

[7] S. Lemey, S. Agneessens, and H. Rogier, "Wearable smart objects: Microwaves propelling smart textiles: A review of holistic designs for wireless textile nodes," *IEEE Microw. Mag.*, vol. 19, no. 6, pp. 83–100, 2018.

[8] P. Nepa and H. Rogier, "Wearable antennas for off-body radio links at VHF and UHF bands: Challenges, the state of the art, and future trends below 1 GHz," *IEEE Antennas Propag. Mag.*, vol. 57, no. 5, pp. 30–52, 2015.

[9] R. B. V. B. Simorangkir, Y. Yang, R. M. Hashmi, T. Björninen, K. P. Esselle, and L. Ukkonen, "Polydimethylsiloxane-embedded conductive fabric: Characterization and application for realization of robust passive and active flexible wearable antennas," *IEEE Access*, published online ahead of print, Aug. 2018.

[10] L. Song and Y. Rahmat-Samii, "A systematic investigation of rectangular patch antenna bending effects for wearable applications," *IEEE Trans. Antennas Propag.*, vol. 66, no. 5, pp. 2219–2228, 2018.

[11] A. Sani, M. Rajab, R. Foster, and Y. Hao, "Antennas and propagation of implanted RFIDs for pervasive healthcare applications," *Proceedings of the IEEE*, vol. 98, no. 9, pp. 1648–1655, September 2010.

[12] R. Lodato, V. Lopresto, R. Pinto, and G. Marrocco, "Numerical and experimental characterization of through-the-body UHF-RFID links for passive tags implanted into

human limbs," *IEEE Trans. Antennas Propag.*, vol. 62, no. 10, pp. 5298–5306, October 2014.

[13] R. C. Hadarig, M. E. de Cos, and F. Las-Heras, "UHF dipole-AMC combination for RFID applications," *IEEE Antennas Wireless Propag. Lett.* vol. 12, pp. 1041–1044, August 2013.

[14] M. A. S. Tajin and K. R. Dandekar, "Pattern reconfigurable UHF RFID reader antenna array," *IEEE Access*, vol. 8, pp. 187365–187372, October 2020.

[15] K. Ye, et al., "A novel textile dual-polarized antenna potentially used in body-centric system," I*EEE International Conference on RFID Technology and Applications (RFID-TA)*, pp. 77–80, Foshan, 2016.

[16] E. Moradi, L. Sydänheimo, G. S. Bova, and L. Ukkonen, "Measurement of wireless power transfer to deep-tissue RFID-based implants using wireless repeater node," *IEEE Antennas Wireless Propag. Lett.*, vol. 16, pp. 2171–2174, May 2017.

[17] J. J. Baek et al., "Design and performance evaluation of 13.56-MHz passive RFID for e-skin sensor application," *IEEE Microw. Wireless Compon. Lett.*, vol. 28, no. 12, pp. 1074–1076, December 2018.

[18] G. Scotti, S. Fan, C. Liao, and Y. Chiu, "Body-implantable RFID tags based on ormocer printed circuit board technology," *IEEE Sens. Lett.,* vol. 4, no. 8, pp. 1–4, August 2020.

[19] C. Miozzi et al., "A general-purpose configurable RFID epidermal board with a two-way discrete impedance tuning," *IEEE Antennas Wireless Propag. Lett.,* vol. 18, no. 4, pp. 684–687, April 2019.

[20] G. Scotti, S. Y. Fan, C. H. Liao, and Y. Chiu, "Body-Implantable RFID tags based on ormocer printed circuit board technology," *IEEE Sens. Lett.,* vol. 4, no. 8, pp. 1–4, August 2020.

[21] I. Bouhassoune, R. Saadane, and A. Chehri, "Wireless body area network based on RFID system for healthcare monitoring: Progress and architectures," *15th International Conference on Signal-Image Technology & Internet-Based Systems (SITIS)*, pp. 416–421, Sorrento, Italy, 2019.

[22] F. Lagha, S. Beldi, and L. Latrach, "Design of UHF RFID body-worn textile tag for wireless applications," *IEEE International Conference on Design & Test of Integrated Micro & Nano-Systems (DTS)*, pp. 1–4, Gammarth-Tunis, Tunisia, 2019.

[23] H. He et al., "Fabrication and performance evaluation of carbon-based stretchable RFID tags on textile substrates," *International Flexible Electronics Technology Conference (IFETC)*, pp. 1–5, Ottawa, ON, 2018.

[24] S. Ahmed et al., "Comparison of wearable E-Textile split ring resonator and slotted patch RFID reader antennas embedded in work gloves," *IEEE J. Radio Freq. Identif.*, vol. 3, no. 4, pp. 259–264, December 2019.

[25] R. K. Singh, A. Michel, P. Nepa, and A. Salvatore, "Glove integrated dual-band Yagi reader antenna for UHF RFID and bluetooth application," *International Workshop on Antenna Technology (iWAT)*, Bucharest, Romania, 2020, pp. 1–3.

[26] P. Hall, Y. Hao, "Antennas and Propagation for Body-centric Wireless Communications," 2nd ed. London / Boston: Artech House. 2012.

[27] J. C. Rautio, "Twenty three years: The acceptance of Maxwell's equations," *J. Appl. Computational Electromagn. Soc.*, vol. 25, no. 12, pp. 998–1006, Dec. 2010.

[28] S. Mandal, S. K. Mandal, R. Mahapatra, A. K. Mal, "Studies on on-chip antenna using standard CMOS technology," *Devices for Integrated Circuit (DevIC), IEEE*, pp. 471–475. 2017.

[29] C. A. Balanis, *Antenna Theory: Analysis and Design*. John Wiley & Sons, 2015.

[30] S. R. Elliot, "Antenna Theory and Design, an IEEE Classical Reissue," *Hoboken, NJ, John Wiley & Sons*, Inc. 2003.

[31] A. Sani, M. Rajab, R. Foster, Y. Hao, "Antennas and propagation of implanted RFIDs for pervasive healthcare applications," *Proceedings of the IEEE*, vol. 98, no. 9, pp. 1648–1655, September 2010.

[32] J. J. Baek et al., "Design and performance evaluation of 13.56-MHz passive RFID for e-skin sensor application," *IEEE Microw. Wireless Compon. Lett.,* vol. 28, no. 12, pp. 1074–1076, December 2018.

[33] M. E. B. Jalil, M. K. Abd Rahim, N. A. Samsuri, N. A. Murad, H. A. Majid, K. Kamardin, M. Azfar Abdullah, "Fractal koch multiband textile antenna performance with bending, wet conditions and on the human body," *Progress in Electromagnetics Research*, vol. 140, pp. 633–652, 2013.

[34] N. A. Elias, N. A. Samsuri, M. K. A. Rahim, N. Othman, "The effects of human body and bending on dipole textile antenna performance and SAR," *Asia Pacific Microwave Conference Proceedings*, pp. 34–36, IEEE, 2012.

[35] B. Hu, G. P. Gao, L. L. He, X. D. Cong, J. N. Zhao, "Bending and on-arm effects on a wearable antenna for 2.45 GHz body area network," *IEEE Antennas and Wireless Propagation Letters*, vol. 15, pp. 378–381, 2015.

[36] F. Boeykens, L. Vallozz, and H. Rogier, "Cylindrical bending of deformable textile rectangular patch antennas," *International Journal of Antennas and Propagation*, 2012.

[37] K. M. Jones, J. A. Mechling, J. W. Strohbehn, and B. S. Trembly, "Theoretical and experimental SAR distributions for interstitial dipole antenna arrays used in hyperthermia," *IEEE Trans. Microw. Theory Tech.*, vol. 37, no. 8, pp. 1200–1209, 1989.

[38] E. Moradi et al., "Backscattering neural tags for wireless brain-machine interface systems," *IEEE Trans. Antennas Propag.*, vol. 63, no. 2, pp. 719–726, Feb. 2015.

[39] X. Chen, S. Ma, L. Ukkonen, T. Björninen, and J. Virkki, "Antennas and antenna-electronics interfaces made of conductive yarn and paint for cost-effective wearable RFIDs and sensors," *IEEE MTT-S International Microwave Symposium (IMS),* pp. 827–830, 2017.

[40] Y. Hong, J. Choi, and J. Tak, "Textile antenna with EBG structure for body surface wave enhancement," *Electron. Lett.,* vol. 51, no. 15, pp. 1131–1132, 2015.

[41] S. Velan et al., "Dual-band EBG integrated monopole antenna deploying fractal geometry for wearable applications," *IEEE Antennas Wirel. Propag. Lett.*, vol. 14, pp. 249–252, 2015.

[42] G. P. Gao, B. Hu, S. F. Wang, and C. Yang, "Wearable circular ring slot antenna with EBG structure for wireless body area network," *IEEE Antennas Wirel. Propag. Lett.*, vol. 17, no. 3, pp. 434–437, 2018.

[43] S. Kim, Y. J. Ren, H. Lee, A. Rida, S. Nikolaou, and M. M. Tentzeris, "Monopole antenna with inkjet-printed EBG array on paper substrate for wearable applications," *IEEE Antennas Wirel. Propag. Lett.*, vol. 11, pp. 663–666, 2012.

[44] K. Agarwal, Y. X. Guo, and B. Salam, "Wearable AMC backed near-endfire antenna for on-body communications on latex substrate," *IEEE Trans. Components, Package. Manuf. Technol.*, vol. 6, no. 3, pp. 346–358, 2016.

[45] Z. H. Jiang, Z. Cui, T. Yue, Y. Zhu, and D. H. Werner, "Compact, highly efficient, and fully flexible circularly polarized antenna enabled by silver nanowires for wireless body-area networks," *IEEE Trans. Biomed. Circuits Syst.*, vol. 11, no. 4, pp. 920–932, 2017.

[46] M. M. Khan and T. Hossain, "Compact planar inverted F antenna (PIFA) for smart wireless body sensors networks," *Engineering Proceedings,* vol. 2, no. 1, p. 63, 2020.

[47] J . Virkki, Z . Wei, A . Liu, et al., "Wearable passive E-Textile UHF RFID tag based on a slotted patch antenna with sewn ground and microchip interconnections," *Int J Antennas Propag.* pp. 27–29, 2017.

[48] T. Djerafi, A. Doghri, K. Wu, "Substrate integrated wave-guide antennas," *Handbook of Antenna Technologies*, pp. 1–60, 2015.

[49] H. Uchimura, T. Takenoshita, and M Fujii, "Development of a laminated wave-guide," IEEE *Trans Microwave Theory Tech.*, vol 46, no. 12. pp. 2438–2443, 1998.

[50] R. Moro, S. Agneessens, H. Rogier, M. Bozzi, "Circularly-polarised cavity-backed wearable antenna in SIW technology," *IET Microwaves, Antennas & Propagation*, vol. 12 no. 1, pp. 127–131, 2017.

[51] D. Chaturvedi, and S. Raghavan, "Compact qmsiw based antennas for wlan/wban applications," *Progress in Electromagnetics Research,* vol. 82, pp. 145–153, 2018.

[52] A. Kiourti and J. L. Volakis, "Stretchable and flexible e-fiber wire antennas embedded in polymer," *IEEE Antennas* and *Wireless Propagat. Lett.*, pp. 1381–1384, 2014.

[53] M. Faenzi, et al., "Realization and measurement of broadside beam modulated metasurface antennas," *IEEE Antennas and Wireless Propagation Letters,* vol. 15, pp. 610–613, 2016.

[54] S. Pandi, C. A. Balanis, C. R. Birtcher, "Design of scalar impedance holographic metasurfaces for antenna beam formation with desired polarization," *IEEE Transactions on Antennas and Propagation,* vol. 63, no. 7, pp. 3016–3024, 2015.

[55] G. Minatti, S. Maci, P. De Vita, A. Freni, M. A. Sabbadini, "Circularly-polarized isoflux antenna based on anisotropic metasurface," *IEEE Transactions on Antennas and Propagation*, vol. 60, no. 11, pp. 4998–5009, 2012.

[56] G. Minatti, et al., "Modulated metasurface antennas for space: Synthesis, analysis and realizations," *IEEE Transactions on Antennas and Propagation* vol. 63, no. 4, pp. 1288–1300, 2015.

[57] R. S. Elliott, "Spherical surface wave antennas," *IEEE Tran. Ant. Propagat.*, vol. 4, no. 3, pp. 422–428, Jul. 1956.

[58] R. Hougardy and R. C. Hansen, "Scanning surface wave antennas—oblique surface waves over a corrugated conductor", *IEEE Trans. Antennas Propagat.,* vol. 6, no. 4, pp. 370–376, Oct. 1958.

[59] L. B. Felson, "Radiation from a tapered surface wave antenna," *IEEE Trans. Antennas Propagat.*, vol. 8, no. 6, pp. 577–586, Nov. 1960.

[60] R. S. Elliott, "Spherical surface wave antennas, " *IEEE Tran. Ant. Propagat.,* vol. 4, no. 3, pp. 422–428, Jul. 1956.

[61] Yang, F. and Rahmat-Samii, Y. (2009). Electromagnetic Band Gap Structures in Antenna Engineering. Cambridge, UK: Cambridge University Press, pp. 203–237.

[62] F. Yang, A. Aminian, Y. Rahmat-Samii, "A low profile surface wave antenna equivalent to a vertical monopole antenna," *Proceedings of the 2004 IEEE Antennas and Propagation Society International Symposium*, vol. 2, pp. 1939–1942, Monterey, CA, June 20–26, 2004.

[63] H. R. Raad, A. I. Abbosh, H. M. Al-Rizzo, and D. G. Rucker, "Flexible and compact AMC based antenna for telemedicine applications," *IEEE Trans. Antennas Propag.*, vol. 61, no. 2, pp. 524–531, 2013.

[64] K. N. Paracha, S. K. A. Rahim, P. J. Soh, M. R. Kamarudin, K. G. Tan, Y. C. Lo, M. T. Islam, "A low profile, dual-band, dual polarized antenna for indoor/outdoor wearable application," *IEEE Access*, vol. 7, pp. 33277–33288, 2019.

[65] A. Alemaryeen, S. Noghanian, "Crumpling effects and specific absorption rates of flexible AMC integrated antennas," *IET Microw. Antennas Propag.* vol. 12, pp.627–635, 2018.

[66] A. Y. I. Ashyap, Z. Z. Abidin, S. H. Dahlan, H. A. Majid, S. M. Shah, M. R. Kamarudin, and A. Alomainy, "Compact and low-profile textile EBG-based antenna for wearable

medical applications," *IEEE Antennas Wireless Propag. Lett.*, vol. 16, pp. 2550–2553, 2017.

[67] S. Zhu and R. Langley, "Dual-band wearable textile antenna on an EBG substrate," *IEEE Trans. Antennas Propag.*, vol. 57, no. 4, pp. 926–935, Apr. 2009.

[68] S. Kim, Y.-J. Ren, H. Lee, A. Rida, S. Nikolaou, and M. M. Tentzeris, "Monopole antenna with inkjet-printed EBG array on paper substrate for wearable applications," *IEEE Antennas Wireless Propag. Lett.*, vol. 11, pp. 663–666, 2012.

[69] D. Sievenpiper, L. Zhang, R. Broas, N. Alexopolous, and E. Yablonovitch, "High-impedance electromagnetic surfaces with a forbidden frequency band," *IEEE Trans. Microw. Theory Techn.*, vol. 47, no. 11, pp. 2059– 2074, 1999.

[70] Y. Rahmat-Samii, F. Yang, "Electromagnetic band gap structures" in *Antenna Engineering,* New York, NY, USA: Cambridge Univ. Press, 2009.

[71] F. Yang, Y. Rahmat-Samii, "Reflection phase characterizations of the EBG ground plane for low profile wire antenna applications," *IEEE Trans. Antennas Propag.*, vol. 51, no. 10, pp. 2691–2703, Oct. 2003.

[72] L. Alonso-González, S. Ver-Hoeye, M. Fernández-García, C. Vázquez-Antuña, and F. L. H. Andrés, "On the development of a novel mixed embroidered-woven slot antenna for wireless applications," *IEEE Access,* vol. 7, pp. 9476–9489, 2019.

[73] J. Baker-Jarvis, R. G. Geyer, J. H. Grosvenor, Jr. Janezic, M. D. Jones, C. A. Riddle, B. Weil, and C. M. Krupka, "Dielectric characterization of low-loss materials a comparison of techniques," *IEEE T Dielect El In*, vol. 5, no. 4, pp. 571–577, 1998.

[74] K. C. Yaw, "Measurement of dielectric material properties," Rohde & Schwarz Application note 2012. Available at: https://webcache.googleusercontent.com/search?q=cache:mEjjIPAsToIJ:https://cdn.rohde-schwarz.com/pws/dl_downloads/dl_application/00aps_undefined/RAC-0607-0019_1_5E.pdf+&cd=2&hl=en&ct=clnk&gl=fi&client=firefox-b-ab.

[75] L. Chen, C. K. Ong, V. V. Varadan, and V. K. Varadan, "Measurement and materials characterization," *Microwave Electronics*, 2004.

[76] R. Gonçalves, R. Magueta, P. Pinho, and N. B. Carvalho, "Dissipation factor and permittivity estimation of dielectric substrates using a single microstrip line measurement," *Applied Computational Electromagnetics Society Journal,* vol. 31, no. 2, pp. 118–125, 2016.

[77] G. Carchon and B. Nauwelaers, "Accurate transmission line characterization on high and low-resistivity substrates," *IET Microwaves, Antennas and Propagation*, vol. 148, no. 5, pp. 285–290, 2001.

[78] W. R. Eisenstadt and Y. Eo, "S-parameter-based IC interconnect transmission line characterization," *IEEE Trans Compon Packaging Manuf Technol,* vol. 15, no. 4, pp. 483–490, 1992.

[79] F. Declercq, H. Rogier, and C. Hertleer, "Permittivity and loss tangent characterization for garment antennas based on a new matrix-pencil two-line method," *IEEE Trans. Antennas Propag*, vol. 56, no. 8, pp. 2548–2554, 2008.

[80] D. Dobkin, "*The RF in RFID: Passive UHF RFID in Practice*," Burlington, MA, USA, Newnes-Elsevier Inc, 2008.

[81] J. Virtanen, L. Ukkonen, T. Björninen, A. Z. Elsherbeni, and L. Sydänheimo, "Inkjet printed humidity sensor for passive UHF RFID systems," *IEEE Trans. Instrum. Meas.*, vol. 60, no. 8, pp. 2768–2777, Aug. 2011.

[82] S. S. Saad and Z. S. Nakad, "A standalone RFID indoor positioning system using passive tags," *IEEE Trans. Ind. Electron.*, vol. 58, no. 5, pp. 1961–1970, May 2011.

[83] G. Marrocco, "Pervasive electromagnetics: sensing paradigms by passive RFID technology," *IEEE Wireless Commun.*, vol. 17, no. 6, pp. 10–17, Dec. 2010.

[84] T. Kellomäki, T. Björninen, L. Ukkonen, and L. Sydänheimo, "Shirt collar tag for wearable UHF RFID systems," *Proc. Eu CAP Conf.*, pp. 12–16, Apr. 2010.

[85] A. Sani, M. Rajab, R. Foster, and Y. Hao, "Antennas and propagation of implanted RFIDs for pervasive healthcare applications," *Proceedings of the IEEE*, vol. 98, no. 9, pp. 1648–1655, Sept. 2010.

[86] R. Lodato, V. Lopresto, R. Pinto, and G. Marrocco, "Numerical and experimental characterization of through-the-body UHF-RFID links for passive tags implanted into human limbs," *IEEE Trans. Antennas Propag.,* vol. 62, no. 10, pp. 5298–5306, Oct. 2014.

[87] K. Ye, et al., "A novel textile dual-polarized antenna potentially used in body-centric system," in *IEEE International Conference on RFID Technology and Applications (RFID-TA)*, pp. 77–80, Foshan, 2016.

[88] EPCglobal. Overview of the ultra high frequency (UHF) regulations worldwide: http://www.gs1.org/epcglobal/implementation.

[89] D. M. Pozar, "Microwave Engineering, 4th ed," Hoboken, NJ, USA, Wiley, 2012.

[90] Keysight Technology. "About dielectric loss models," *Keysight Online Knowledge Center* 2009. Available at: http://edadocs.software.keysight.com/display/ads2009U1/About+Dielectric+Loss+Models.

[91] C. Svensson and G. E. Dermer, "Time domain modeling of lossy interconnects," *IEEE Transactions on Advanced Packaging*, vol. 24, no. 2, pp. 191–196, 2001.

[92] A. R. Djordjevic, R. M. Biljic, V. D. Likar-Smiljanic, and T. K. Sarkar, "Wideband frequency-domain characterization of FR-4 and time-domain causality," *IEEE Trans. Electromagn. Compat.* vol. 43, no. 4, pp. 662–667, 2001.

[93] J. C. Rautio, V. Demir, "Microstrip conductor loss models for electromagnetic analysis," *IEEE Trans. Microw. Theory Tech,* vol. 51, no. 3, pp. 915–921, 2003.

[94] T. N. Killian, S. M. Rao, M. E. Baginski, "Electromagnetic scattering from electrically large arbitrarily-shaped conductors using the method of moments and a new null-field generation technique," *IEEE Trans. Antennas Propag.*, vol. 59, no. 2, pp. 537–545, 2011.

[95] A. Lea, P. Hui, J. Ollikainen, and R. Vaughan, "Propagation between on-body antennas," *IEEE Trans. Antennas Propag.,* vol. 57, no. 11, pp. 3619–3627, 2009.

[96] U.S. Food and Drug Administration, Center for Devices and Radiological Health, "Reporting of computational modeling studies in medical device submissions: Draft guidance for industry and food and drug administration staff," 2014. [Online]. Available at: http://www.fda.gov/downloads/MedicalDevices/DeviceRegulationandGuidance/GuidanceDocuments/UCM381813.pdf [Accessed:June-2020].

[97] K. H., Yang, J. Hu, N. A. White, A. I. King, C. C. Chou, and P. Prasad, "Development of numerical models for injury biomechanics research: A review of 50 years of publications in the Stapp Car Crash Conference," *Stapp Car Crash J.*, vol. 50, pp. 529–490, 2006.

[98] M. Iwamoto, Y. Nakahira, and H. Kimpara, "Development and validation of the total human model for safety (THUMS) toward further understanding of occupant injury mechanisms in precrash and during crash," *Traffic Injury Prevention*, vol. 16, pp. 1–13, 2015.

[99] M. Grimm and D. Manteuffel, "Electromagnetic wave propagation on human trunk models excited by half-wavelength dipoles," *Proc. Antennas Propag. Conf.*, Loughborough, U.K, pp. 493–496, 2010.

[100] N. H. M. Rais, P. J. Soh, F. Malek, S.Ahmad, N. B. M. Hashim, and P. S. Hall, "A review of wearable antenna," *Proc. Antennas Propag. Conf.*, pp. 225–228, Loughborough, U.K., 2009.

[101] Commission of European Communities: Council recommendation on limits for exposure of the federal public to electromagnetic fields: 0 Hz–300 GHz. June 1998.

[102] IEEE Std C95.3-2002: IEEE recommended practice for measurements and computations of radio frequency electromagnetic fields with respect to human exposure to such fields 100 kHz–300 GHz. 2002.

[103] IT'IS Foundation, Tissue Properties [Online]. Available at: https://www.itis.ethz.ch/virtual-population/tissue-properties/downloads.

[104] S. Gabriel, R. W. Lau, and C. Gabriel, "The dielectric properties of biological tissues: III. Parametric models for the dielectric spectrum of tissues," *Phys. Med. Biol.*, vol. 41, no. 11, pp. 2271–2293, Nov. 1996.

[105] M. Khabiri, "Design and Simulation of Implantable PIFA, Presence of ANSYS Human Body Model for Biomedical Telemetry Using ANSYS HFSS," *Ozen Engineering, Inc.*

[106] S. Ma, L. Ukkonen, L. Sydänheimo, T. Björninen, "Robustness evaluation of split ring resonator antenna system for wireless brain care in semi-anatomical ellipsoid head model," *Applied Computational Electromagnetics Society Journal*, vol. 33, no. 9, pp. 966–972, 2018.

[107] K. Koski, T. Björninen, L. Sydänheimo, L. Ukkonen, and Y. Rahmat-Samii, "A new approach and analysis of modeling the human body in RFID-enable body-centric wireless systems," *Int. J. Antennas Propag.*, vol. 2014, 2014.

[108] J. Kim and Y. Rahmat-Samii, "Implanted antennas inside a human body: Simulations, designs, and characterizations," *IEEE Trans Microw Theory Tech*, vol. 52, no. 8, pp. 1934–1943, 2004.

[109] Voyantic, Ltd., Espoo, Finland: http://www.voyantic.com/.

[110] "Rubber-Cal, Closed Cell Rubber – EPDM." Available at: http://www.rubbercal.com/closed-cell-rubber-epdm.html.

[111] Arlon, Ar1000™ and AR600™ microwave materials, *ARLON Materials for Electronics*, 2000.

[112] Bungard, "Original Bungard fotobeschichtetes Basismaterial FR4," *Technische Daten*.

[113] "SOLIANI, Nickel Copper–coated fabric, Datasheet conductive fabric-GA.NICU." Available at: https://www.solianiemc.com/en/p/emc-emi-copper-nickel-coated-polyester-fabric.

[114] "Aiwei Functional Textile, nickel copper–coated conductive fabric circuit for electrical products," *Conductive Fabric*. Available at: http://www.conductive-fabric.com/sale-8234197-nickel-copper-coated-conductive-fabric-circuit-for-electrical-products.html.

[115] M. Stoppa and A. Chiolerio, "Wearable electronics and smart textiles: A critical review," *Sensors*, vol. 14, no. 7, pp. 11957–11992, 2014.

[116] M. A. Aziz, M. K. A. Rahim, and A. Asrokin, "The studies on different scaling factor for microstrip antenna design," *Applied Electromagnetics,* p. 4, 2005.

[117] L. Yang, X. Shi, K. Chen, K. Fu, and B. Zhang, "Analysis of photonic crystal and multi-frequency terahertz microstrip patch antenna," *Physica B: Condensed Matter*, pp. 11–14, 2013.

[118] S. N. Burokur, M. Latrach, and S. Toutain, "Theoretical investigation of a circular patch antenna in the presence of a left-handed medium," *IEEE Antennas and Wireless Propagation Letters*, vol. 4, pp. 183–186, 2005.

[119] S. Op't Land, O. Tereshchenko, M. Ramdani, F. Leferink, R. Perdriau, "Printed circuit board permittivity measurement using waveguide and resonator rings," *Electromagnetic Compatibility, Tokyo (EMC'14/Tokyo),* pp. 777–780, 2014.

[120] T. Björninen, F. Yang, "Low-profile head-worn antenna with a monopole-like radiation pattern," *IEEE Antennas Wireless Propag. Lett.*, vol. 15, pp. 794–797, 2016.

[121] Y. Qian, W. R. Deal, N. Kaneda, T. Itoh, "Microstrip-fed quasi-Yagi antenna with broadband characteristics," *Electronics Letters*, vol. 34 no. 23, pp. 2194–2196, 1998.

[122] H. Yagi, S. Uda, "Projector of the sharpest beam of electric waves," *Proceedings of the Imperial Academy*, vol. 2, no. 2, pp. 49-52, 1926

[123] K. Agarwal, Y. X. Guo, B. Salam, and L. C. W. Albert, "Latex based near-endfire wearable antenna backed by AMC surface," *IEEE MTT-S International Microwave Workshop Series on RF and Wireless Technologies for Biomedical and Healthcare Applicrations*, pp. 1–3, Singapore, Dec. 2013.

[124] B. S. Abirami and E. F. Sundarsingh, "EBG-backed flexible printed Yagi–Uda antenna for on-body communication," *IEEE Trans. Antennas Propag.*, vol. 65, pp. 3762–3765, 2017.

[125] G. Marrocco, "RFID grids: Part I—Electromagnetic theory," *IEEE Trans. Antennas and Propag.*, vol. 59, no. 3, pp. 1019–1026, Mar. 2011.

[126] Prinel, "Flexible PCB Printed Circuit Boards," 2019.

[127] F. Yang, A. Aminian, and Y. Rahmat-Samii, "A novel surface-wave antenna design using a thin periodically loaded ground plane," *Microw. Optical Technol. Lett.*, vol. 47, pp. 240–245, 2005.

[128] F. Yang and Y. Rahmat-Samii, "Reflection phase characterizations of the EBG ground plane for low profile wire antenna applications," IEEE *Trans. Antennas Propag.*, vol. 51, pp. 2691–2703, 2003.

[129] A. Foroozesh, L. Shafai, "Investigation into the application of artificial magnetic conductors to bandwidth broadening, gain Enhancement and beam shaping of low profile and conventional monopole antennas," *IEEE Transactions on Antennas and Propagation*, vol. 59, no. 1, pp. 4–20, Jan. 2011.

[130] K. Jebbawi, M. Egels, P. Pannier, "Design of an ultra-wideband UHF RFID reader antenna for wearable ankle tracking applications," in *European Microwave Conference in Central Europe (EuMCE)*, pp. 525–528, 2019.

[131] S. Ahmed et al., "Glove-integrated textile antenna with reduced SAR for wearable UHF RFID reader," *IEEE International Conference on RFID Technology and Applications, Pisa, Italy*, pp. 231-235, 2019.

[132] C. Occhiuzzi, S. Cippitelli and G. Marrocco, "Modeling, design and experimentation of wearable RFID sensor tag," *IEEE Trans. Antennas Propag.*, vol. 58, no. 8, pp. 2490–2498, Aug. 2010.

[133] G. A. Casula, G. Montisci and H. Rogier, "A wearable textile RFID tag based on an eighth-mode substrate integrated waveguide cavity," IEEE Access, vol. 8, pp. 11116–11123, Jan. 2020.

[134] R. K. Singh, A. Michel, P. Nepa and A. Salvatore, "Compact Quasi-Yagi Reader Antenna for UHF RFID Smart-Glove," 5th International Conference on Smart and Sustainable Technologies (SpliTech), pp. 1-4, 2020.

[135] M. Daiki and E. Perret, "Segmented solenoid coil antenna for UHF RFID near-field reader applications," *IEEE J. Radio Freq. Identif.,* vol. 2, no. 4, pp. 210–218, December 2018.

[136] R. K. Singh, A. Michel, P. Nepa and A. Salvatore, "Glove integrated dual-band Yagi reader antenna for UHF RFID and Bluetooth application," *International Workshop on Antenna Technology (iWAT)*, pp. 1–3, Bucharest, Romania, 2020.

[137] E. Moradi et al., "Backscattering neural tags for wireless brain–machine interface systems," *IEEE Transaction on Antennas Propagation*., vol. 63, no. 2, pp. 719–726, Feb. 2015.

[138] J. Grosinger, "Feasibility of backscatter RFID system on the human body," *EURASIP J. Embedded Syst.*, vol. 2013, no. 2, pp. 1-10, Mar. 2013.

[139] W. Mongan, E. Anday, G. Dion, A. Fontecchio, K. Joyce, T. Kurzweg, Y. Liu, O. Montgomery, I. Rasheed, C. Sahin, S. Vora, and K. Dandekar, "A multi-disciplinary framework for continuous biomedical monitoring using low-power passive RFID-based wireless wearable sensors," *IEEE International Conference on Smart Computing*, pp. 1-6, St. Louis, MO, USA, May 2016.

[140] S. Milici, S. Amendola, and A. Bianco, "Epidermal RFID passive sensor for body temperature measurements," *IEEE RFID Technology and Applications Conference (RFID-TA)*, pp. 140–144, Tampere, Finland, Sep. 2014.

[141] P. V. Nikitin, "Antennas and propagation in UHF RFID systems," *IEEE International Conference on RFID*, pp. 277–288, Las Vegas, NV, USA, Apr. 2008.

[142] G. Marrocco, "The art of UHF RFID antenna design: Impedance-matching and size-reduction techniques," *IEEE Antennas Propag. Mag.,* vol. 50, no. 1, pp. 66–79, Mar. 2008.

[143] E. Perret, S. Tedjini, and R. S. Nair, "Design of antennas for UHF RFID tags," *Proc. IEEE*, vol. 100, no. 7, pp. 2330–2340, July 2012.

[144] H. H. Tran, S. X. Ta, and I. Park, "A compact circularly polarized crossed-dipole antenna for an RFID tag," *IEEE Antennas Wireless Propag. Lett.*, vol. 14, pp. 674–677, Dec. 2010.

[145] H. D. Chen , C. H. Tsai, and C. Y. Kuo, "Circularly polarized loop tag antenna for long reading range RFID applications," *IEEE Antennas Wireless Propag. Lett.*, vol. 12, pp. 1460–1463, Nov. 2013.

[146] J. H. Lu and B. S. Chang, "Planar compact square-ring tag antenna with circular polarization for UHF RFID applications," *IEEE Trans. Antennas Propag.*, vol. 65, no. 2, pp. 432–441, Nov. 2016.

[147] A. S. M. Sayem, D. Le, R. B. V. B. Simorangir, T. Björninen, K. P. Esselle, R. M. Hasmi, and M. Zhadobov, "Optically transparent flexible robust circularly polarized antenna for UHF RFID tags," *IEEE Antennas Wireless Propag. Lett.*, vol. 19, no. 12, pp. 2334–2338.

[148] E. K. Kaivanto, M. Berg, E. Salonen, and P. de Maagt, "Wearable circularly polarized antenna for personal satellite communication and navigation," *IEEE Trans. Antennas Propag.*, vol. 59, no. 12, pp. 4490–4496, Dec. 2011.

[149] M. Joler and M. Boljkovac, "A sleeve-badge circularly polarized textile antenna," *IEEE Trans. Antennas Propag.*, vol. 66, no. 3, pp. 1576–1579, Mar. 2018.

[150] J. Li, Y. Jiang and X. Zhao, "Circularly polarized wearable antenna based on NinjaFlex-embedded conductive fabric," *Intl. J. Antennas Propag.*, vol. 2019, article ID 3059480, 8 pages, Sep. 2019.

[151] C. W. Chiu and J. H. Hong, "Circularly polarized tag antenna on an AMC substrate for wearable UHF RFID applications," *IEEE-APS Topical Conference on Antennas and Propagation in Wireless Communications*, pp. 71–74, Verona, Italy, Sep. 2017.

[152] H. Lee, J. Tak, and J. Choi, "Wearable antenna integrated into military berets for indoor/outdoor positioning system," *IEEE Antennas Wirel. Propag. Lett.*, vol. 16, pp. 1919–1922, Mar. 2017.

[153] W. S. Chen, C. K. Wu, and K. L. Wong, "Novel compact circularly polarized square microstrip antenna," *IEEE Trans. Antennas Propag.,* vol. 49, no. 3, pp. 340–342, Mar. 2001.

[154] K. Girish, Ray K. P, "Broadband Microstrip Antennas," Norwood, MA, Artech House, Inc, 2003.

[155] W. Kin-lu, "Compact and Broadband Microstrip Antennas," New York, Wiley Interscience, 2002.

[156] C. A. Balanis, "Antenna theory: Analysis and design," John Wiley & Sons, 2016

[157] T. Ali and R. C. Biradar, "A compact hexagonal slot dual band frequency reconfigurable antenna for WLAN applications," *Microwave and Optical Technology Letters*, vol. 59, no. 4, pp. 958–964, 2017.

[158] T. Björninen, K. E. Delzo, L. Ukkonen, A. Z. Elsherbeni, and L. Sydänheimo, "Long-range metal mountable tag antenna for passive UHF RFID systems," *IEEE International Conference on RFID Technologies and Applications*, pp. 15–16, 202–206, 2011.

[159] T. Ali, R. C. Biradar, "A miniaturized circularly polarized coaxial fed superstrate slot antenna for L-band application," *Internet Technol. Lett.,* vol. 6, no. 1, Nov. 2018.

[160] A. M . Thomas, "Modern Antenna Design 2nd ed," vol. 2. John-Wiley & Sons, Inc., pp. 18–24, 2005.

[161] EPC UHF radio frequency identity protocols: class 1 generation 2 UHF RFID version 1.2.2 [Online]. Available at: https://www.gs1.org/standards/epc-rfid [Accessed:June-2020].

[162] H. T. Friis, "A note on a simple transmission formula," *Proc. IRE*, vol. 34, no. 5, pp. 254–265, 1946.

[163] A. S. Za'aba, S. N. Ibrahim, N. F. A. Malek, and A. M. Ramly, "Development of wearable patch antenna for medical application," *IEEE Regional Symposium on Micro and Nanoelectronics (RSM)*, pp. 260–263, 2017.

[164] D. Rano and M. Hashmi, "Design and analysis of wearable patch antenna array for MBAN applications," *Twenty-Second National Conference on Communication (NCC)*, pp. 1–6, 2016.

[165] J. Yanamadala, G. M. Noetscher, V. K. Rathi, S. Maliye, H. A. Win, A. L. Tran, and S. N. Makarov, "New VHP-Female v. 2.0 full-body computational phantom

and its performance metrics using FEM simulator ANSYS HFSS," *37th Annual International Conference of the IEEE Engineering in Medicine and Biology Society (EMBC)* pp. 3237–3241, 2015.

[166] Y. Kuang, S. Ma, L. Ukkonen, J. Virkki, T. Björninen, "Circularly polarized textile tag antenna for wearable passive UHF RFID systems," *International Applied Computational Electromagnetics Society Symposium-China*, pp 1-2, 2018.

[167] H. D. Chen, W. S. Chen, S. H. Kuo, "CP RFID tag design for metal surface mount," *In Proceedings of 2011 Cross Strait Quad-Regional Radio Science and Wireless Technology Conference,* Vol. 1, pp. 491-493, 2011.

[168] S. Ma, L. Ukkonen, L. Sydänheimo, T. Bjöminen, "Dual-Layer circularly polarized split ring resonator inspired antenna for wearable UHF RFID tag," *IEEE International Symposium on Antennas and Propagation USNC/URSI National Radio Science Meeting*, pp. 683-684, 2018.

[169] C. W. Chiu, J. H. Hong, "Circularly polarized tag antenna on an AMC substrate for wearable UHF RFID applications," *IEEE-APS Topical Conference on Antennas and Propagation in Wireless Communications,* pp. 71-74, 2017.

PUBLICATION I

Microstrip Transmission Line Model Fitting Approach for Characterization of Textile Materials as Dielectrics and Conductors for Wearable Electronics

Duc Le, Ye Kuang, Leena Ukkonen, Toni Björninen

International Journal of Numerical Modelling Electronic Networks Devices and Fields 32(7), February 2019, doi: 10.1002/jnm.2582

Microstrip Transmission Line Model Fitting Approach for Characterization of Textile Materials as Dielectrics and Conductors for Wearable Electronics

Duc Le[(1)], Ye Kuang[(2)], Leena Ukkonen[(1)], Toni Björninen[(1)]

[(1)]Faculty of Medicine and Health Technology
Tampere University, Tampere, Finland

[(2)]College of Textiles, Donghua University, Shanghai, China

***Abstract* - Characterization of unconventional materials is essential in the field of microwave engineering. In this study, we present a method for the microwave characterization of conductive and non-conductive textile materials. Our approach is based on fitting the material parameters of a numerical microstrip transmission line model so that the simulated signal transmission properties match with the data we measure from implemented test lines. Unlike many conventional test structures, such as cavity resonators and waveguides, microstrip lines can be readily manufactured in textile technology with rather relaxed tolerances in the fabrication process. In addition, our method provides estimates for all three key material parameters; frequency-dependent relative permittivity and loss tangent of the non-conductive line substrate and the bulk conductivity of the strip conductor. For validation, we have characterized conventional microwave laminates and compared the data with the datasheets and literature, and used our parameter estimates for the textile materials to optimize fully textile-based low-pass filters. Overall, the results confirm the applicability of our method for microwave engineering with textile materials.**

I. INTRODUCTION

Recently, the textile materials have been replacing circuit boards in wearable devices and body-worn wireless applications because they enable seamless cloth-integration [1][2]. Nevertheless, the high-frequency characterization of textiles and electro-textiles in terms of the relative permittivity, loss tangent, and conductivity is challenging, because the conventional methods rely on procedures that are not suitable for textile-based flexible and compressible materials. The two-line method was introduced [3] for measuring the relative permittivity of circuit board materials, however, it does not provide the loss tangent. The other conventional methods rely on the accurate manufacturing of test structures, such as resonators and waveguides, and the direct inversion of their closed-form design equations [4][5][6][7][8][9]. In contrast, our approach stems from the numerical model fitting. According to our findings, this provides a more robust method that provides a not only a frequency-continuous dielectric model but also an estimate for the bulk conductivity. Overall, it balances the ease of use and data processing and sufficient accuracy for microwave engineering applications. Importantly, it is appropriate to the novel textile or flexible substrates and conductor materials that are required for building modern wearable electronics devices.

To summarize our method, at first, we implement a transmission line on an unknown substrate using copper foil as a conductor and estimate the relative permittivity and loss tangent of the substrate by fitting the simulated maximum attainable transducer power gain of the line to the measured one in the least-squares sense. Next, we apply the same approach for estimating the conductivity of an electro-textile conductor on the known substrate. We have tested the method on

conventional circuit board materials and textiles. As a further validation, we used the obtained data for optimizing textile low-pass filters and found very close agreement between their simulated and measured properties. In the future, we will utilize the method for optimizing wearable textile antennas and microwave components.

II. Background and the Material Models

A. Microstrip transmission line

Microstrip line is a planar microwave transmission line with the cross-sectional structure shown in Fig. 1. It comprises a strip conductor and a ground plane separated by a dielectric substrate layer and supports quasi-TEM (transverse electromagnetic) wave propagation towards the direction normal to the cross-sectional plane. Due to its simple structure that is compatible with standard circuit board manufacturing methods, the microstrip line is a widely used interconnection in microwave circuits [10].

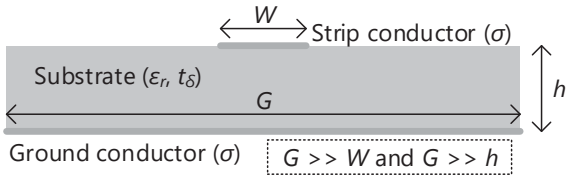

Figure 1. *Cross-sectional view of a microstrip transmission line.*

Overall, the width of the strip conductor (W), thickness of the substrate (h) and the relative permittivity (ε_r) of the substrate are determinant for the phase constant and characteristic impedance (Z_0) of the line, whereas the conductor thickness (t) and conductivity (σ) of the strip and ground conductors, and the loss tangent of the substrate (t_δ) determine the signal attenuation. Normally, circuit designers rely on ε_r as the key parameter to optimize the line width to achieve Z_0 that equals their system impedance, which is very often 50 Ω. This is done to minimize the signal reflection at the beginning and end of the line that would be caused by impedance discontinuity. In contrast, our method of estimating the material parameters of an unknown substrate and conductor materials relies upon a reverse approach: we adapt the material parameters in our numerical model of the line so that the simulated results match with the data that we measure from a test line built using the materials of interest.

Since in our case the material parameters are unknown, we cannot compute Z_0 of the test lines. Therefore, we base the model fitting to the maximum attainable transducer power gain (G_{max}) of the line, which we will refer to as 'maximum gain' from here onwards. By definition, it is the power gain parameter that excludes the signal reflection loss due to impedance discontinuity at the in/output of the line and is thus determined totally by its internal structure and materials. The maximum gain is computed as [10]

$$G_{max} = \frac{|S_{21}|}{|S_{12}|}\left(K - \sqrt{K^2 - 1}\right), \tag{1}$$

where K is given by

$$K = \frac{1 - |S_{11}|^2 - |S_{11}|^2 + |\det(\mathbf{S})|^2}{2|S_{12}S_{21}|} \tag{2}$$

and S_{ij} are the elements of the 2-by-2 scattering matrix **S** of the line. It should be noted that since a transmission line is a passive two-port device, i.e. $G_{max} < 1$, it is unconditionally stable with $K > 1$, which guarantees that equation (1) is well-defined.

B. Frequency-model of the relative permittivity and loss tangent of dielectric material

In the notion of complex relative permittivity ($\tilde{\varepsilon}_r$), the real-valued physical relative permittivity (ε_r) of a material is given by $\varepsilon_r = \mathrm{Re}(\tilde{\varepsilon}_r)$ and its relation to loss tangent (t_δ) is given by [10]

$$\tilde{\varepsilon}_r = \varepsilon' - j\varepsilon'' = \varepsilon'(1 - jt_\delta), \tag{3}$$

where j is the imaginary unit. Considering the dielectric relaxation phenomenon, the Svensson/Djordjevic model provides a frequency-dependent complex relative permittivity, which is computed as [11][12][13]

$$\tilde{\varepsilon}_r(f) = \varepsilon_\infty + a \ln \frac{f_H + jf}{f_L + jf}, \tag{4}$$

where f_L and f_H define the model's low- and high-frequency trends, a is a constant and $f \longrightarrow \infty \Longrightarrow \tilde{\varepsilon}_r \longrightarrow \varepsilon_\infty$. Now, the knowledge of the values ε_r and t_δ at a given central frequency f_0, enables the modelling of their values at a range frequencies around it as follows. First, using equation (3), the constant a can be computed from equation (4) as

$$a = -\varepsilon_{r0} t_{\delta 0} \mathrm{Im}\left(\ln \frac{f_H + jf_0}{f_L + jf_0}\right), \tag{5}$$

where $\varepsilon_{r0} = \varepsilon_r(f_0)$ and $t_{\delta 0} = t_\delta(f_0)$. Consequently, the constant ε_∞ can be solved from equation (4) and then equation (3) implies that

$$\varepsilon_r(f) = Re\left(\tilde{\varepsilon}_r(f)\right) \quad \text{and} \quad t_\delta(f) = -\frac{\mathrm{Im}\left(\tilde{\varepsilon}_r(f)\right)}{\mathrm{Re}\left(\tilde{\varepsilon}_r(f)\right)}, \tag{6}$$

As will be explained below, our model fitting method targets at estimating the central frequency parameters ε_{r0} and $t_{\delta 0}$ of a dielectric materials through comparison of data from numerical simulations and measurements of a microstrip transmission line built on the material of interest.

C. Conductor model

According to the laws of electromagnetism, the amplitude of the current density inside a conductor decreases exponentially with the depth measured from the surface and the skin depth (δ) is defined as the distance where the amplitude has declined by the factor of $1/e$ from its value at the surface. In general, δ can be approximated as [10][14]

$$\delta = \sqrt{\frac{2}{\omega\mu\sigma}}, \tag{7}$$

where μ and σ are the magnetic permeability and the bulk conductivity of the conductor, respectively, and ω is the angular frequency. Thus, it is natural to expect that the energy loss in a conductor is, in addition to the parameters in equation (7), a function of the conductor thickness.

Because the analysis of finite thickness conductors can be computationally demanding, numerical tools often model planar conductors as infinitely thin sheets with a surface impedance that approximately accounts for the impact of the finite thickness. In our simulations, we have used the double sided skin effect model that assumes the current is flowing on the two planar surfaces of the conductor [15]. In this case, the conductor (thickness: t) is divided into two equal layers of thickness $t/2$ and each layer is modeled as two infinitely thin sheets in parallel, both having the surface impedance given by [14]

$$Z_s = \frac{(1-j)}{\delta\sigma}\cot\left((1-j)\frac{t}{2\delta}\right). \tag{8}$$

As will be explained below, our model fitting method targets at estimating the bulk conductivity of electro-textile materials through comparison of data from numerical simulations adopting the above described conductor model and measurements of a microstrip transmission line.

III. Data Processing and the Estimated Material Parameters

A. Model fitting based on the least-squares method

We used the least-squares method to estimate the best-fit values for the material parameters ε_{r0}, $t_{\delta 0}$, and σ. In this process, we varied them over a given interval in the numerical simulation of a microstrip transmission line and extracted the corresponding scattering matrices $\mathbf{S}_{sim}$ over the frequency range of interest. For each set of material parameters, we then computed the sum of the squared residuals with respected to measured data ($\mathbf{S}_{mes}$) as

$$E(\epsilon_{r0}, t_{\delta 0}, \sigma) = \sum_{n=1}^{N}\left(G_{max}\left(\mathbf{S}_{sim}^{(n)}\right) - G_{max}\left(\mathbf{S}_{mes}^{(n)}\right)\right)^2, \tag{9}$$

where the superscript (n) denotes the frequency index and looked for the one that minimized E. Here we selected the G_{max} as the model function, because it is sensitive for the material parameters and a key parameter in the optimization and performance evaluation of most microwave devices.

Overall, our model fitting strategy was two-fold. First, we implement a microstrip transmission line on an unknown substrate using copper foil with known properties as the conductor. Then we estimate ε_{r0} and $t_{\delta 0}$ in the least-squares sense by identifying the values that minimize $E(\varepsilon_{r0}, t_{\delta 0})$. Next, we estimated σ of an unknown conductor of a line built on the substrate with previously estimated ε_{r0} and $t_{\delta 0}$, but this time minimizing E from equation (9) with respect to the single parameter σ. In the following sections, we will describe the numerical modelling and data processing in more detail.

B. Experimental arrangement, simulations, and data processing

Firstly, we built the test lines with the properties listed in Table 1 for the estimation of the dielectric properties of three substrate materials: FR4 circuit board (Bungard Elektronik) [16], Arlon AR1000 high-permittivity microwave laminate [17], and textile cell-rubber foam ethylene-propylene-diene-monomer (EPDM) from Johannes Birkenstock Gmbh [18]. Secondly, we used the FR4 as a substrate for test lines (see Table 1) for estimating the conductivity of two conductive

fabrics: Nickel and Copper plated fabric (Shieldit Super from LessEMF) [19] and Copper plated fabric (Pure Copper Taffeta from LessEMF) [19], which will be referred to as NCPF and CPF, respectively, from here onwards. In this experiment, both the line and the groud plane were implemented from the conductive fabric under test.

Our method of estimating the material parameters does not impose any specific requirements for the widths and lengths of the test lines and we have chosen these dimensions considering the ease of manufacturing and testing. The lengths of all the lines were 65 mm and to ensure quasi-TEM wave propagation in the structures, the ground plane was extended 4 times the line width on boths sides of the lines. We used regular SMA (SubMiniature version A) soldered to all the lines to connect them to vector network analyser (Keysight E5080A) for the measurement of the S-parameters over the frequency range from 400 MHz to 3 GHz. This frequency range was considered in the model fitting since it covers many of the relevant wireless communication bands for wearable wireless systems, such as MedRadio at 401-406 MHz, the worldwide ISM band centred at 2.45 GHz, GPS at 1575.42 MHz, and UHF RFID bands at 866 MHz and 915 MHz.

For numerical simulations, we used Keysight ADS, where we implemented the models of the measured lines using the dielectric and conductor models described in Section II. From the simulation, we extracted the S-parameters of the lines. Finally, we computed the maximum gains of the lines from the simulated and measured data using Equations (1-2) and performed the two-step least-squares model fitting, as described above, using Matlab.

TABLE I
Properties of the test lines.

Step 1: Estimation of the dielectric properties.					
	Thickness [mm]	Conductor	Conductor thickness [μm]	Conductivity [MS/m]	Strip width [mm]
FR4	1.5848	Plated copper	35	58	6
AR1000	0.127	Plated copper	35	58	6
EPDM	3	Adhered copper foil	40	58	6
Step 2: Estimation of the conductivity.					
	Conductor thickness [μm]	Substrate (FR4) thickness [mm]	Estimated substrate ε_r at 1 GHz	Estimated substrate t_δ at 1 GHz	Strip width [mm]
NCPF	76	1.5848	4.43	0.017	3
CPF	73	1.5848	4.43	0.017	3

Table II shows the estimated relative permittivity, loss tangent at our centre frequency of 1 GHz, and the bulk conductivity. As illustrated, the estimated relative permittivity and loss tangent of FR4 agree closely with the values reported in [19]. Similarly, for AR1000, which is a high-permittivity microwave circuit board, the estimate agrees with the manufacturer's data although our estimate for the permittivity is slightly higher. The reason may be the thickness of our material sample, which according to the manufacturer affects the relative permittivity due to material processing. Finally, the estimated relative permittivity of the EPDM textile material is 1.534, which is close to the values used in [20][21] for practical antenna designs.

TABLE II
The estimated material paramaters.

Dielectric properties				
	Estimated values		Reference values	
	ε_r at 1 GHz	t_δ at 1 GHz	ε_r at 1 GHz	t_δ at 1 GHz
FR4	4.43	0.017	4.6 [13] & 4.5 [16]	0.018 [13] & 0.015 [16]
AR1000	12.99	0.003	10 [17]	0.0025 [17]
EPDM	1.534	0.01	1.21 [20] & 1.23 [21]	0.02 [21]
Conductivity [S/m]				
NCPF	0.7×10^5	CPF	2.6×10^5	

After finding the best-fit data for the dielectric materials, the conductivity of the electro-textile materials was varied in the numerical simulation to find a value that provided the best-fit between the simulated and measured maximum gain of test lines listed in Table I. The obtained conductivities for NCPF and CPF were 0.7×10^5 S/m and 2.6×10^5 S/m, respectively.

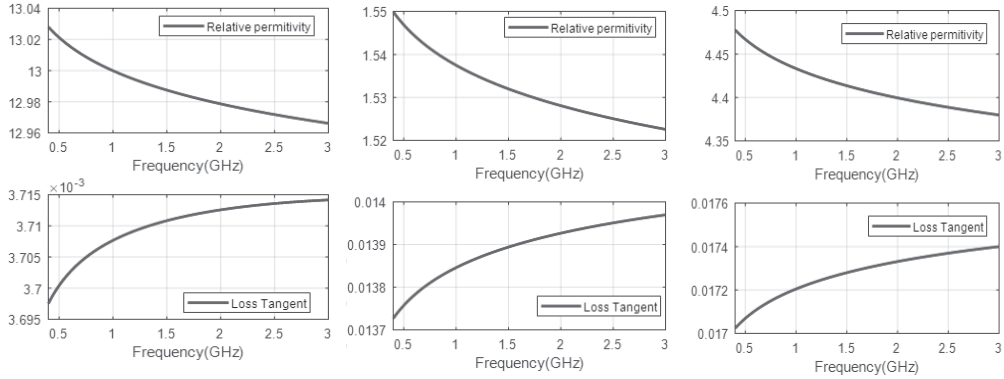

Figure 2. *Relative permittivity and loss tangent. Left: AR1000, center: EPDM, right:FR4.*

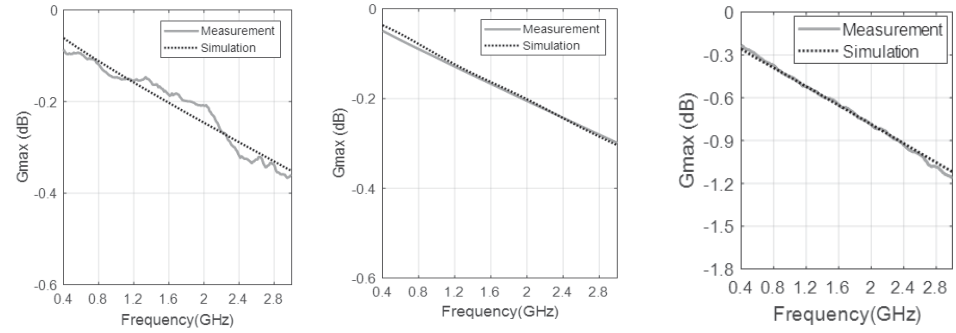

Figure 3. *Simulated and measured maximum gain of three tested lines. Left: AR1000, center: EPDM with adhered copper foil, right: FR4 with NCPF.*

As can be seen from Figure 2, the frequency model for the relative permittivity and loss tangent which we implemented in the numerical simulation, gives only small frequency-variation over the studied range from 400 MHz to 3 GHz. Thus, although the dielectric relaxation model in the

numerical simulation may have improved the model fitting, for most microwave engineering applications, we could also model the studied materials using constant values as estimates for the relative permittivity and loss tangent over this frequency band. However, for instance the dielectric properties of FR4 have been shown to exhibit significant variation over decades of frequencies [13]. Finally, Figure 3 presents the simulated and measured maximum gain of three of the studied lines. The results agree closely, also in the case textile materials, demonstrating the effectiveness and applicability of our method for wearable electronics applications.

IV. Sample Designs and Model Validation

In this section, we present the implementation and testing of low-pass stub and stepped impedance filters using the estimated material parameters from Section III. Filters were selected in this validation, because they are examples of common microwave transmission line components which are sensitive towards material parameters and exhibit strongly varying frequency responses. The filters were fabricated on copper-plated FR4 and on EPDM with both electro-textiles we have characterized.

A. The microstrip line low-pass stub filter

The structural diagram of a microstrip line low-pass stub filter is shown in Figure 4. Here the filter SF1 is built on FR4 with plated copper, and SF2 and SF3 are on EPDM with adhered CPF and

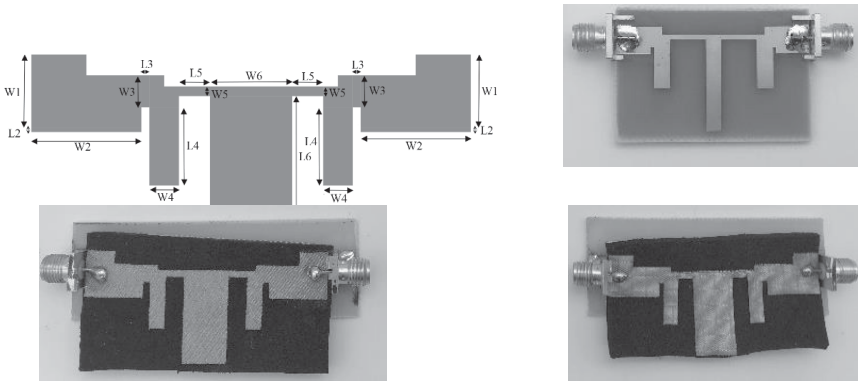

Figure 4. *The structural diagram and manufactured prototypes of the low-pass stub filters. Top: SF1, bottom left: SF2 and bottom right: SF3.*

CNPF, respectively. The geometrical parameters of the filters are listed in Table III. The key-parameters for optimizing the filter are the lengths, widths and separations of the three open circuited stubs. This way, the reactive loading is added to the transmission line to tailor the desired filtering frequency response for it [10]. We designed all the filters for 50 Ω system impedance. The targeted specifications were pass-band with the maximum of 1 dB signal attenuation up to 1.5 GHz, and input and output reflection coefficients better than −10 dB and the minimum stop-band

attenuation of −10 dB starting at 2.2 GHz. Here, we considered the third order filter topology sufficient. Table III lists the dimension of each segment of the low-pass stub filter.

TABLE III
LOW-PASS STUB FILTER GEOMETRICAL PARAMETERS

Symbol	Dimension (mm)		
	SF1	SF2	SF3
W1	7.8	9.2	9.2
W2	7.7	13.8	13.8
W3	5.67	4	4
W4	4.88	3.7	3.7
W5	0.8	1.2	1.2
W6	3.71	10.3	10.3
L2	1.091	0.5	0.5
L3	0.7	1	1
L4	8.6	9.8	9.8
L5	7.8	3.8	3.9
L6	20.66	17.9	17.9

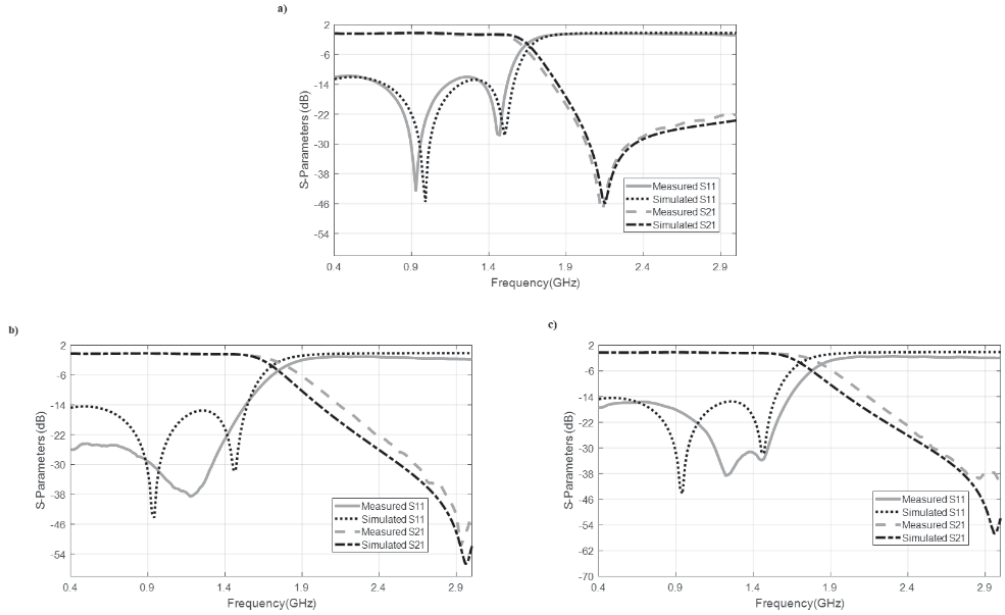

Figure 5. *Simulated and measured S-parameters of the low-pass stub filters. Top: SF1, bottom left: SF2, bottom right: SF3.*

As shown in Figure 5, the simulated and measured results for the FR4 filter (SF1) are in excellent agreement and the filter meets its specifications. The comparison between the numerical model and the measured results for the textile filters (SF2 and SF3) show also good agreement although a small difference can be observed in the stop-band attenuation. A possible source for this maybe

the slightly non-planar profile of the textile material which has affected the properties of the open-circuited microstrip line stubs that are determinant for the response of the filters. However, the agreement in the pass-band is excellent and the difference in the simulated and measured S_{11} magnitude is less significant, because the discrepancies occur at very small values below −14 dB.

B. The microstrip line low-pass stepped impedance filters

Stepped impedance filter is another common class of microwave transmission line filters [10]. It benefits from simpler structure and design compared with the stub filter, but does not provide as sharp transition between the pass- and stop-bands. Unlike the stub filter, where the stubs are tuned to achieve the reactive loading for engineering the desired pass- and stop-bands, in stepped impedance filter this achieved by alternating line sections with maximally low and high characteristic impedances. These correspond to wide and narrow line sections, respectively. The structure and manufactured prototypes of three stepped impedance filters are shown in Figure 6 with their geometrical dimensions listed in Table IV. All the filters were designed for 50 **Ω** system impedance with the pass-band corner frequency with 3-dB attenuation at 1 GHz and stop-band starting frequency with more than 15 dB attenuation at 2 GHz.

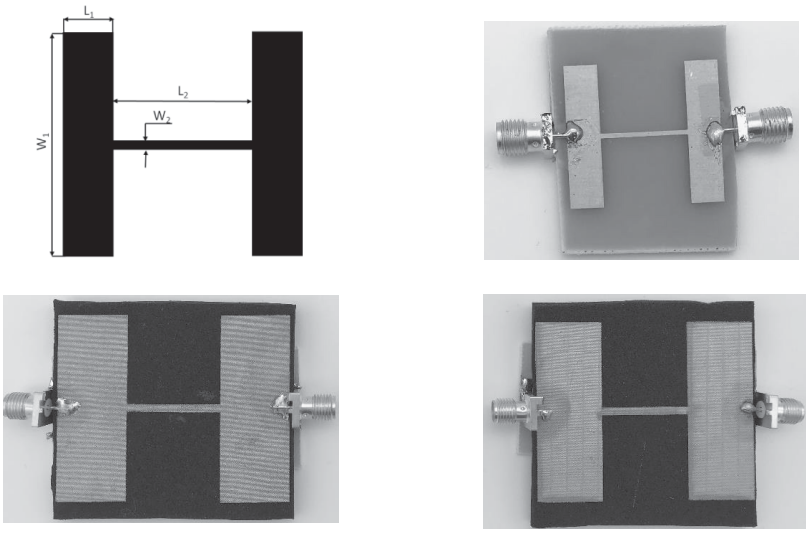

Figure 6. *The layout and samples of stepped impedance low-pass filters. Top right: SIF-1, bottom left: SIF-2 and bottom right:SIF-3*

TABLE IV
Low-pass stepped impedance filter geometrical parameters.

No.	Substrate	Conductor	L_1	W_1	L_2	W_2
SIF-1	FR4	Copper	6	25	15	1
SIF-2	EPDM	CPF	16	43	21	2
SIF-3	EPDM	NCPF	16	43	21	2

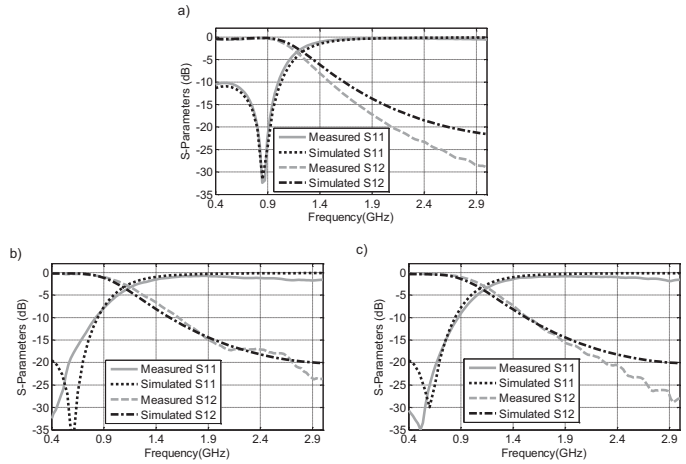

Figure 7. *Simulated and measured S-parameters of the stepped impedance filters. Top: SIF-1, bottom left: SIF-2 and bottom right: SIF-3*

The simulated and measured S-parameters of the three stepped impedance filters are presented in Figure 7. In all cases, the designed filters meet their specifications. The simulated and measured S_{11} parameters agree closely and the simulation predicts the pass-band attenuation well. Towards higher frequencies, there are differences in between the simulated and measured S_{21} parameters of SIF-1 and SIF-3. The is likely due to manufacturing tolerances, such as the width of the narrow line sections and the impact of the finite physical distance between the point where the SMA connectors contacts the line and the calibration phase reference plane of the VNA, which is inside the connector's body. However, this is less critical, since the discrepancies occur in the stop-band where the key-requirement for the filters' performance is the sufficient attenuation and not the signal transmission properties.

V. CONCLUSION

The knowledge of the relative permittivity and loss tangent of dielectrics and the conductivity of conductors is pertinent to the judicious optimization of microwave circuits and antennas. In particular, it is important for wearable electronics applications, because unlike regular circuit boards, the textile materials do not come with specified electromagnetic properties. To address, this challenge, we presented a microstrip transmission line model fitting approach for the estimation of these parameters for regular fabrics and electrically conductive textiles. The method benefits from simple test structures, which are readily built from textile materials with relatively relaxed manufacturing tolerances, and uncomplicated data processing. We have applied the method on circuit boards with known properties and to different textile and electro-textile materials within the frequency range from 400 MHz to 3 GHz. The obtained results are consistent with the published literature and datasheets. Moreover, we optimized transmission line low-pass stub and stepped impedance filters, using the estimated material parameters in numerical simulations. The comparison of the simulated and measured responses of the filters provided further assurance for the effectiveness and applicability of our method for wearable electronics applications.

REFERENCES

[1] Stoppa, M., Chiolerio, A., Wearable electronics and smart textiles: a critical review. *Sensors* **2014**; ***14*(7)**, pp. 11957-11992.

[2] Kaushik, V., Lee, J., Hong, J., Lee, S., Lee, S., Seo, J., Lee, T., Textile-based electronic components for energy applications: Principles, problems, and perspective, *Nanomaterials* **2015**; **5(3)**, pp. 1493 - 1531.

[3] Declercq, F., Rogier, H., Hertleer, C., Permittivity and loss tangent characterization for garmen antennas based on a new matrix-pencil two-line method, *IEEE Transactions on antennas and propagation* **2008; 56(8)**, pp. 2548-2554.

[4] J. Baker-Jarvis, R. G., Geyer, J. H, Grosvenor, Jr., Janezic, M. D., Jones, C. A., Riddle, B., Weil, C. M., Krupka, J., Dielectric characterization of low-loss materials a comparison of techniques, *IEEE Transactions on Dielectrics and Electrical Insulation* **1998; 5(4)**, pp. 571-577.

[5] Yaw, K. C., Measurement of dielectric material properties, *Rohde-Schwarz Application note* **2012**. Available: https://www.rohde-schwarz.com/fi/applications/measurement-of-dielectric-material-properties-application-note_56280-15697.html

[6] Chen, L., Ong, C. K., Varadan, V. V., Varadan, V. K., Measurement and Materials Characterization, *Microwave Electronics* **2004**.

[7] Gonçalves, R., Magueta, R., Pinho, P., Carvalho, N. B., Dissipation factor and permittivity estimation of dielectric substrates using a single microstrip line measurement, *Applied Computational Electromagnetics Society Journal* **2016; 31(2)**, pp. 118-125.

[8] Carchon, G., Nauwelaers, B., Accurate transmission line characterization on high and low-resistivity substrates. *IET Microwaves, Antennas and Propagation* **2001; *148*(5)**, pp. 285-290.

[9] Eisenstadt, W. R., Eo, Y., S-parameter-based IC interconnect transmission line characterization. *IEEE Transactions on Components, Hybrids, and Manufacturing Technology* **1992; 15(4)**, pp. 483-490.

[10] Pozar, D. M., Microwave Engineering 4e **2011**.

[11] Keysight Technology, "About Dielectric Loss Models", *Keysight Online Knowledge Center* **2009**. Available: http://edadocs.software.keysight.com/display/ads2009U1/About+Dielectric+Loss+Models.

[12] Svensson, C., Dermer G. E., Time domain modeling of lossy interconnects, *IEEE Transactions on Advanced Packaging* **2001; 24(2)**, pp. 191-196.

[13] Djordjevic, A. R., Biljic, R. M., Likar-Smiljanic, V. D., Sarkar, T. K., Wideband frequency-domain characterization of FR-4 and time-domain causality, *IEEE Transactions on Electromagnetic Compatibility* **2001; 43(4)**, pp. 662-667.

[14] Rautio, J. C., Demir, V., Microstrip conductor loss models for electromagnetic analysis. *IEEE Transactions on Microwave Theory and Techniques* **2003; 51(3)**, pp. 915-921.

[15] Keysight Technology, "Conductor Loss Models in Momentum," *Keysight Online Knowledge Center* **2009**. Available: http://edadocs.software.keysight.com/display/ads2009/Conductor+Loss+Models+in+Momentum.

[16] Bungard, "FR4 Data Sheet," Available: https://www.bungard.de/index.php/en/products/downloads

[17] Arlon Materials, "AR1000 Data Sheet," Available: https://www.cirexx.com/arlon-materials/

[18] Johannes Birkenstock GmbH, EPDM Cellular Rubber (type ZKAP): http://www.joh-birkenstock.de/content/gummi.html

[19] LessEMF, Shieldit Super and Pure Copper Taffeta conductive fabrics: http://www.lessemf.com/fabric.html

[20] Manzari, S., Pettinari S., Marrocco G., Miniaturized and tunable wearable RFID tag for body-centric applications, 2012 IEEE International Conference on RFID-Technologies and Applications (RFID-TA), Nice, 2012, pp. 239-243.

[21] Koski, K., Sydänheimo, L., Rahmat-Samii, Y., Ukkonen, L., Fundamental characteristics of electro-textiles in wearable UHF RFID patch antennas for body-centric sensing systems, *IEEE Transactions on Antennas and Propagation*, 2014; 62(12), pp. 6454-6462.

PUBLICATION II

Dual-ID headgear UHF RFID tag with broadside and end-fire patterns based on quasi-Yagi antenna

Duc Le, Leena Ukkonen, Toni Björninen

IEEE Asia-Pacific Microwave Conference
December 2019, doi: 10.1109/APMC46564.2019.9038680

Dual-ID Headgear UHF RFID Tag with Broadside and End-Fire Patterns based on Quasi-Yagi Antenna

Duc Le, Leena Ukkonen, Toni Björninen
Faculty of Medicine and Health Technology
Tampere University, Tampere, Finland
{vietduc.le, leena.ukkonen, toni.bjorninen}@tuni.fi

***Abstract*—We present a wearable quasi-Yagi antenna on a periodic surface for a dual-ID passive UHF RFID tag embedded in headgear. The antenna produces a near end-fire radiation pattern directed towards the user's line of sight with the directivity of 4 dBi. Moreover, it integrates another tag by utilizing the Yagi antenna's reflector as a second dipole tag antenna with broadside radiation directed upwards from the user. Hence, in one platform, we obtain a dual-ID tag with near end-fire and broadside patterns for the two tag IDs. The former is achieved by inserting a periodic surface made up of a 2-by-2 grid of square loops in between the antenna and the body. This enhances the launching of surface waves for achieving the end-fire radiation and suppresses the undesired electromagnetic antenna-body interaction.**

Keywords—quasi-Yagi antenna; RFID tag; periodic surface; wearable antenna

I. Introduction

The development of microwave and antenna technology considering the human body as the operation environment is pivotal to achieving versatile and reliable wireless body-centric systems. Such technology is at demand in several application areas including e.g. wireless health monitoring. The employment of radio identification (RFID) and RFID-inspired backscattering communications has been established an advantageous solution for low-power body-centric systems. Nowadays, several wearable antennas have been researched for this application [1-3], but in terms of the radiation pattern, it is challenging to aim the directional radiation beam in the antenna plane, because when worn on the body, antennas such as dipoles that are omnidirectional in the air become directive towards the normal of the body surface [2]. Previously, an ellipsis shaped center-fed microstrip patch antenna for headgear was shown to produce a monopole-like pattern around the head at 5.8 GHz [3]. However, the dimension of antenna is not scalable to the UHF RFID bands centered at 915 MHz.

To advance upon these works, we prosed a quasi-Yagi headgear RFID tag operating at 866 MHz that provided a directive beam in the antenna plane towards the front of the user [4]. However, despite the suitable end-fire pattern, the antenna gain remained limited −14.2 dBi, which may limit applicability in practice. In this work, we introduce an enhanced periodic surface and further antenna optimization that enables more than 3-dB improvement in the end-fire gain within the same antenna size. In addition, to enhance the versatility and spatial coverage of the tag, we create a second dipole tag in the same platform by reusing the Yagi antenna's reflector as a second tag antenna. With this approach, the antenna provides radiation pattern also in the upward direction of the user's head without increasing its size. Another challenge in this research is that the total footprint size of the antenna should be restricted to around 80 mm by 80 mm for fitting it in a headgear. At 915 MHz, this is approximately $0.25\lambda \times 0.25\lambda$, whereas a conventional Yagi antenna features a 0.5λ reflector and other elements of comparable size. Thus, we have employed folding of the reflector, driven element, and the director for the purpose of miniaturization.

II. Antenna Structure and Design Considerations

A. Concept and Requirements

The main idea is to develop the quasi-Yagi antenna and the folded-dipole based reflector on top of the human head and pertain the near end-fire radiation pattern and dipole-type radiation. To achieve this target, we isolate the antenna section to the body part by the periodic surface rather than the regular ground plane, which degrades the antenna properties due to image current. In general, the antenna development in this research is motivated by previous research [5] and [6] introducing on body Yagi antenna and for the on body dipole antenna, [8] EBG-based RFID dipole tag for rugged on-body and metal mounted applications and the periodic surface wave analyze shown in [9]. In this research, the antenna modelling and optimization was done by ANSYS High Frequency Structure Simulator (HFSS), which is a full-wave electromagnetic field solver based on the finite element method. The antenna modeling employs the simplified head and neck model and antenna installation. The size of the polygonal cylinder representing the head and neck is approximate to actual adult male head size. The cylinder material is skin ($\varepsilon_r = 41.6$, $\sigma = 0.86$ S/m), because it is the tissue type closest to the antenna. The antenna placement on the head model is shown in Fig. 4. Considering the wearable application, we used flexible EPDM cell-rubber foam ($\varepsilon_r = 1.53$, $\sigma = 0.01$ S/m [11]) as the antenna substrate. Moreover, the UHF RFID microchip (NXP UCODE G2iL; turn-on power −18 dBm) is mounted at the dipole's feed point. The chip is modelled as a parallel connection of R = 2850

kΩ and C = 0.91 pF [14], which is the impedance of 12.8-*j*191 Ω at 915 MHz.

B. Periodic Surface

The load periodic patch facilitates the propagation of the electromagnetic wave in all incident angles and polarization phase at the operating frequency [9]. The dimension of these square patches is simulated and optimized based on the Floquet theory and the periodic boundary condition by using HFSS software [13]. The main target of the load periodic patch is to get $90^0 \pm 45^0$ reflection phase response at desired frequency region including 915 MHz [9]. Following the guidelines from [9], we set the size of the square patches to $W \approx 0.1\lambda$ at 915 MHz and their spacing to g = 1.5 mm. The simulation model of unit cell and the phase reflection are shown in Fig. 1 and the specific dimension is illustrated in Fig. 2. Next, the periodic surface is composed of a 2-by-2 grid of the unit cells.

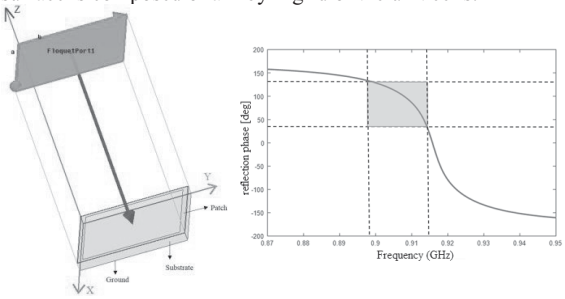

Fig.1. The Floquet port simulation and reflection phase outcome of the load periodic patch.

C. Antenna Structure and Design Principles

The Uda-Yagi antenna consists of three crucial sections, namely driven element, director and reflector and the reflector in this research also plays as another dipole antenna which is a commonly used antenna configuration in UHF RFID tags.

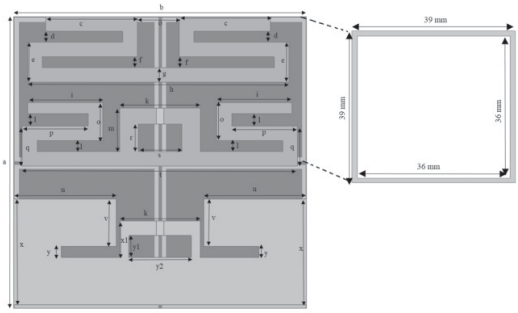

a	b	c	d	e	f	g	h	i	k	l	m
80	80	25	3	11	3	4	72	21	22	4	11
o	p	q	r	s	x	t	u	v	x1	y1	y2
12	18	11	7	12	29	75	28	13	10	6	17

Fig. 2. The geometry and dimension of the antenna in details.

As shown in Fig. 2, we have folded all the element of the antenna to ensure it fits in 80 mm by 80 mm limited head dimension as demonstrated. To maximize the tag's readable range and total gain, we optimized antenna impedance to equal the complex conjugate of IC chip's impedance by using inductive loop matching defined by parameters *r* and *s* for the driven element and *y1* and *y2* for the dipole based reflector.

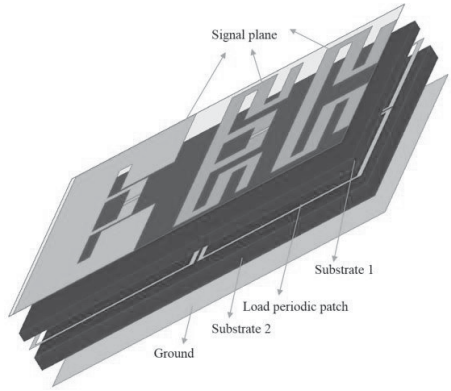

Fig.3. Exploded view of the antenna.

The exploded view of the antenna in Fig. 3 illustrates the number and the order of antenna layers. The first layer is the signal plane of the Yagi and dipole-based reflector antenna. This layer is printed on a polyester (PET) substrate with mechanical flexibility and relative permittivity ε_r = 3.2 and loss tangent tanδ = 0.003 [12]. The thickness of the PET substrate and copper conductor are 35 µm and 18 µm. Next, we set up them on the first 3 mm thickness EPDM substrate that are the second layer. The third layer is the load periodic patch also printed on the flexible substrate, which is placed on the second EPDM substrate. The last layer is the ground plane.

III. Simulation Result and Discussion

The 3D gain pattern of the antenna installed on the head and neck model at 915 MHz is demonstrated in Fig. 4. It can be observed that the radiation pattern direction of quasiYagi antenna with the periodic surface is towards the negative x-axis and those of the dipole-based reflector is upwards the positive z-axis. The maximum gain of the Yagi antenna and the dipole are -7.5 dB at φ=180° and $\theta = 45^{\circ}$ and -6.1 dB at φ=180° and $\theta = 0^{\circ}$ respectively. Fig. 5 illustrates directivity and an attainable read range of two antennas from 860 MHz to 960 MHz.

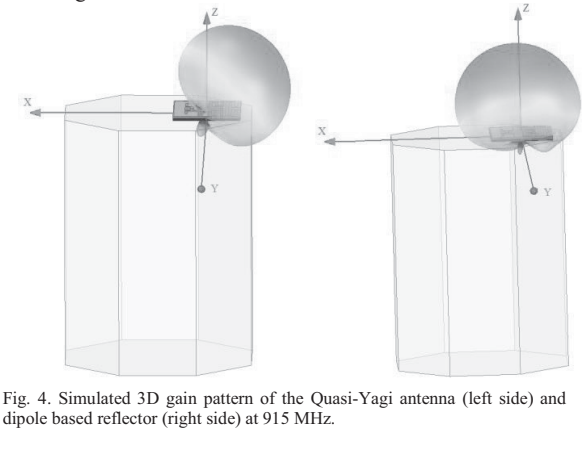

Fig. 4. Simulated 3D gain pattern of the Quasi-Yagi antenna (left side) and dipole based reflector (right side) at 915 MHz.

The maximum directivity of the Yagi antenna is 7 dBi at φ=180° and $\theta = 45^{\circ}$ and 4 dBi at φ=180° and $\theta = 90^{\circ}$. Those of the dipole antenna is 6.6 dBi at φ=180° and $\theta = 0^{\circ}$.

The dimensional miniaturization to fit the antenna on the human head comes at the cost of reduced gain, which is also partly impacted by the dissipative biological background. However, in terms of the attainable read range of the tag, the highest value that Yagi antenna can provide is approximately 4 meters at φ=180° and $\theta = 45^{\circ}$ and 3 meters in the direction where the user is facing.

Moreover, the attainable read range of the dipole antenna reaches 5 meters at 920 MHz and approximately 5 meters at 915 MHz at upward direction. Towards user's facing direction, the read range of this antenna is only 1.5 meters, which is much lower than that of the Yagi antenna is as expected.

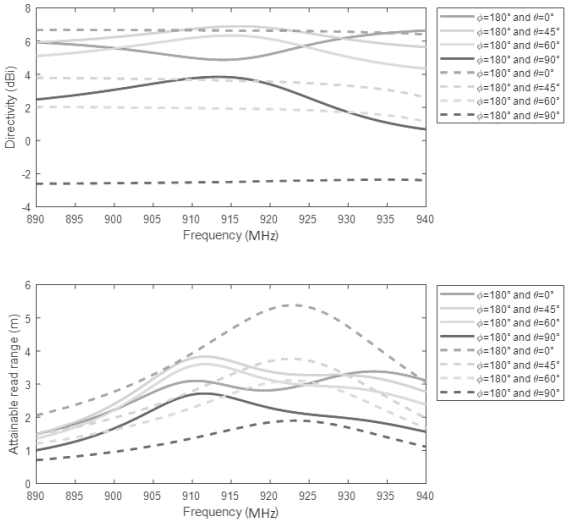

Fig. 5. Simulated directivity and an attainable read range of the Yagi antenna (continuous line) and the dipole based reflector (dash line).

It is noted that the computed read range of both antennas by the Friis' model as described in [2] under the RFID emission limit of 3.28 W EIRP is above 3.5 meters (Yagi antenna) and 5.5 meters (dipole antenna). In addition, it should be noted that these distances could be increased by a factor 1.7 to 5.9 meters and 9.3 meters, respectively, with the latest IC chip such NXP UCODE 8 chip having lower turn-on power of –23 dBm. The previous research [4] presented a Quasi –Yagi antenna with single ID for a headgear. In this research, with the modification of the antenna geometry and the feeding point position, the antenna gain is doubly improved. Moreover, we have created a second tag on the same platform by inserting by utilizing the reflector element of the Yagi antenna as a dipole tag with a second IC chip. It provides broadside pattern directed upwards from the user, thus enhancing the versatility and spatial coverage of the system without increasing its size.

IV. Conclusion

We introduced a novel two antenna system that provides a dual-ID RFID tag for a headgear. It comprises quasi-Yagi antenna where the reflector element is reused as an independent dipole antenna and the two RFID ICs are mounted in the driven element and reflector. The quasi-Yagi tag (IC in the driven element) exhibits end-fire pattern in the antenna plane towards the direction the user is facing and the dipole tag (IC in the reflector) produces broadside pattern directed upwards from the user. The end-fire pattern of the quasi-Yagi tag is enabled by a periodic surface composed of a 2-by-2 grid of square loops between the antenna and the head. The surface was optimized to support the launching of surface waves thus enhancing the end-fire radiation. Simultaneously, it helps decoupling the antenna from the biological background for reducing the undesired antenna-body interaction.

References

[1] C. Chiu and J. H. Hong, "Circularly polarized tag antenna on an AMC substrate for wearable UHF RFID applications," IEEE-APS Topical Conference on Antennas and Propagation in Wireless Communications, Verona, 2017, pp. 71-74.

[2] T. Björninen, "Comparison of three body models of different complexities in modelling of equal-sized dipole and folded dipole wearable passive UHF RFID tags," Appl. Computational Electromagn. Soc. J., vol. 33, no. 6, pp. 706–709, June 2018.

[3] T. Björninen and F. Yang, "Low-profile head-worn antenna with a monopole-like radiation pattern," IEEE Antennas Wireless Propag. Lett., vol. 15, pp. 794-797, 2016.

[4] D. Le, L. Ukkonen, and T. Björninen,"Quasi-Yagi Antenna on a Periodic Surface for Low-Profile Headgear RFID Tag with Endfire Radiation", 2019.

[5] K. Agarwal, Y. X. Guo, B. Salam and L. C. W. Albert, "Latex based near-endfire wearable antenna backed by AMC surface," 2013 IEEE MTT-S International Microwave Workshop Series on RF and Wireless Technologies for Biomedical and Healthcare Applications (IMWS-BIO), pp. 1-3, Dec. 2013.

[6] B. S. Abirami and E. F. Sundarsingh, "EBG-backed flexible printed Yagi–Uda antenna for on-body communication," IEEE Trans. Antennas Propag., vol. 65, pp. 3762-3765, 2017.

[7] H. Lee, S. Kim, D. De Donno, and M. M. Tentzeris, "A novel "universal" inkjet-printed EBG-backed flexible RFID for rugged on-body and metal mounted applications," In IEEE/MTT-S International Microwave Symposium Digest, pp. 1-3, 2012.

[8] L.Akhoondzadeh-Asl, P. S. Hall, and Y. Nechayev, "Novel conformal surface wave Yagi antenna for on-body communication channel," In 2010 IEEE Antennas and Propagation Society International Symposium, pp. 1-4, 2010.

[9] F. Yang and Y. Rahmat-Samii, "Reflection phase characterizations of the EBG ground plane for low profile wire antenna applications," IEEE Transactions on antennas and propagation, vol. 51, pp. 2691-2703, 2003.

[10] F. Yang, A. Aminian and Y. Rahmat-Samii, "A novel surface-wave antenna design using a thin periodically loaded ground plane," Microw. Optical Technol. Lett., vol. 47, pp. 240-245, 2005.

[11] D. Le, Y. Kuang, L. Ukkonen, and T. Björninen, "Microstrip transmission line model fitting approach for characterization of textile materials as dielectrics and conductors for wearable electronics", Intl. J Numerical Modelling Electronic Netw. Dev. Fields, in press.

[12] Prinel, "Flexible," http://www.prinel.fi/tuotteet-flex.

[13] HFSS, "Getting started with HFSS: Floquet ports," http://www.ansoft.com, accessed July 2007.

[14] NXP Semiconductors, "UCODE G2iL and G2iL+", 2019.

PUBLICATION III

A dual-ID RFID tag for headgear based on quasi-Yagi and dipole antennas

Duc Le, Leena Ukkonen, Toni Björninen

IEEE Antennas and Wireless Propagation Letters

June 2020, doi: 10.1109/LAWP.2020.2999735

A Dual-ID RFID Tag for Headgear based on Quasi-Yagi and Dipole Antennas

Duc Le, *Member, IEEE*, Leena Ukkonen, *Member, IEEE*, Toni Björninen, *Senior Member, IEEE*
Faculty of Medicine and Health Technology
Tampere University, Tampere, Finland
{vietduc.le, leena.ukkonen, toni.bjorninen}@tuni.fi

***Abstract*—We present a dual-ID RFID headgear based on quasi-Yagi antenna where we reuse the reflector element as second dipole antenna that provides radiation pattern upwards from the user's head. Thus, we achieve simultaneously the broadside and end-fire patterns without increasing the size of the antenna platform. For avoiding the unpredictable impact of the surface of the human body to the electromagnetic properties of the antenna platform, we inserted a periodic surface made up of a 2-by-2 grid of square loops beneath it. It facilitates launching of surface waves thereby enhancing the end-fire radiation for the quasi-Yagi antenna and its back metal plate isolates the antenna platform from the human body. We have fitted the whole structure on the headgear by folding the quasi-Yagi antenna elements and created the antenna on a low-permittivity textile substrate. Moreover, we have modelled the antenna in both simple and anatomical head models, both including curvature, and measured the attainable read ranges of 6.8 meters and 5 meters, for the quasi-Yagi and dipole tags, respectively, in head-worn configuration.**

***Index Terms*—quasi-Yagi antenna; RFID tag; periodic surface; wearable antenna**

I. INTRODUCTION

The advent of the wireless era in medicine and healthcare has prompted a huge demand for the development of wireless body area systems comprising implantable and wearable devices [1-4]. With their energy-efficient and versatile characteristics, radio frequency identification (RFID) and RFID-based backscattering communication systems have been recognized as compelling solution for low-power body-centric systems. This cutting-edge approach offers marked benefits for wireless health technology [5-7]. The operation of the RFID system is based on the electromagnetic waves transmitted by the reader and the backscattering of the modulated digital signal from the passive RFID tag, in which an ultra-low-power integrated circuit with an antenna provide identification and sensing functionalities [8-12]. Very often, these tags also need to be seamlessly integrated into wearable items to be worn directly on the body [13-14]. Recently, some efforts have been made to develop antennas for the headgear configurations [15-18]. A multi-layer antenna in the form of a microstrip patch antenna has often been integrated into military berets. This device benefits from antenna-body isolation by the ground plane [15]. Nevertheless, for planar antennas, it is challenging to get the directive radiation pattern in the antenna plane, since in their standard configurations, most antennas with ground plane, such as microstrip patch antenna, provide directive broadside patterns and when placed on body. Previously, an ellipsis shaped center-fed microstrip patch antenna for headgear has been shown to produce a monopole-like pattern around the head at 5.8 GHz [16]. However, the dimensions of this antenna are not scalable to the UHF RFID bands, which are centered at 866 MHz or 915 MHz worldwide.

In an earlier study [17], we presented our head-worn quasi-Yagi antenna on a periodic surface made up of square patches. Although end-fire radiation was achieved, the simulated antenna gain remained limited to −14.2 dBi, which may limit the applicability of this scheme in practice. After further research [18], we optimized the antenna's geometry and changed the periodic surface into a 2-by-2 grid of square loops, which doubled the antenna's end-fire gain in the simulations. Moreover, we reused the reflector as the second dipole antenna. Hence, this antenna was also able to direct the radiation pattern upwards from the user's head without changing the total size of the antenna footprint. To achieve the required level of miniaturization, we utilized the folding technique for the reflector, the driven element, and the director. This reduced the size of the antenna by up to 50% compared to a conventional dipole antenna. Consequently, the antenna was approximately $0.25\lambda \times 0.25\lambda$ or 80 mm by 80 mm, which allows it to be fitted into the headgear.

In order to advance the previous research further, in this study we validate the modelling result using more realistic head models (simplified and anatomical) both including curvature and implement two-port modeling approach to more accurately account for the mutual coupling between the two radiating elements. Moreover, for the first time, we present measured results of the headgear RFID tag. The tag's performance is characterized by measuring it in head-worn configurations both from the front and above of the user.

D. Le, L. Ukkonen and T. Björninen are with Faculty of Medicine and Health Technology, Tampere University, Tampere, Finland.

II. The Antenna Structure, EM Optimization and Evaluation of the Tag's Performance

The antenna development began by considering the quasi-Yagi antenna structure shown in Fig. 3. The antenna structure originates from [19-20], where the Yagi-Uda latex antenna configuration on the AMC (artificial magnetic conductor) was proposed to produce the end-fire radiation pattern, and it advances and expands our initial studies [17-18]. For creating the dual-ID RFID tag based on the developed antenna, we interface it with NXP UCODE G2iL RFID microchip [21] with the turn-on power of –18 dBm and its frequency-dependent impedance was modelled as a parallel connection of a resistor (R = 2850 Ω) and capacitor (C = 0.91 pF), where the equivalent component values were measured in [21]. At 915 MHz, the IC impedance is approximately 12.8−j191 Ω. The metal layers of the antenna were patterned from 18 μm thick copper on 35 μm polyester (PET; ε_r = 3.2, σ = 0.003 S/m [22]) substrate. The periodic surface was sandwiched between two textile layers of flexible, ethylene-propylene-diene-monomer (EPDM) rubber foam (ε_r = 1.53, σ = 0.01 S/m [23]).

A. Periodic Surface

As discussed in our previous simulation studies [17-18], the function of the periodic surface is two-fold. Firstly, its back metal layer helps to suppress the unwanted electromagnetic interaction between the antenna and the body and secondly the periodic surface is optimized to facilitate the launching of the surface waves in the antenna plane. Thus, it improves end-fire radiation pattern of the quasi-Yagi antenna. After the process of analyzing the periodic surface, the surface-wave antenna was designed using a thin periodically loaded ground plane [24-25]. The unit cell of the periodic surface is optimized under Floquet boundary conditions to get a $90^0 \pm 45^0$ reflection phase response in the desired frequency region, which was centered at 915 MHz as shown in Fig. 1. Next, the symmetrical unit cell was tuned in order to minimize the total size of the periodic surface and to improve the stability of the reflection phase with respect to the direction of the incident wave. Later, the periodic surface dimensions were fine-tuned to fit with the total size of the antenna. Finally, the periodic surface was developed by periodically repeating unit cells along the x and y-axes' dimensions, forming the units into a 2-by-2 grid as Fig. 2.

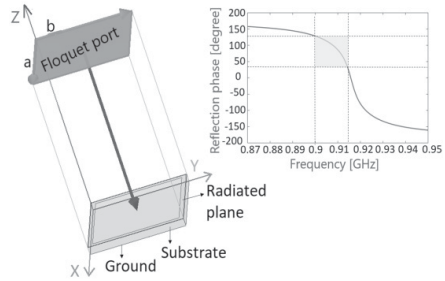

Fig. 1. Floquet port simulation of the reflection phase of the periodic surface.

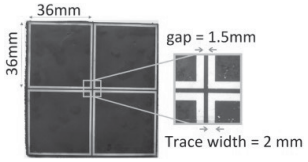

Fig. 2. The periodic surface set-up on the EPDM substrate.

B. Numerical Model of the Quasi-Yagi Antenna

In this research, the RFID tag modeling and optimization were conducted in an ANSYS High-Frequency Structure Simulator (HFSS), which is a full-wave electromagnetic field solver based on the finite element method. The major goal in the optimization was to achieve bi-conjugate matching at the two antenna ports with the impedance of the RFID IC connected to them and achieving good end-fire directivity for Port 1 (red marking in Fig. 3) and broadside directivity of Port 2 (blue marking in Fig. 3). In our modeling approach, we consider the antenna as a two-port network.

In our initial assessment, the coupling between the ports was found to be at maximum around –10 dB in under perfect bi-conjugate impedance matching at the ports. This is not significantly high, yet non-negligible in terms of the input impedances of the two antenna ports. Thus, we have utilized the two-port network theory in computing the input impedance of both ports so that the loading effect of the ICs at connected to them is accounted for and targeted to achieve bi-conjugate impedance matching [26]. Moreover, we implemented the frequency-dependent port terminations in the simulation model, so that the full-wave modeling approach implicitly accounts for the antenna array effects present at general N-port RFID grids, which have been explicitly analyzed in [27].

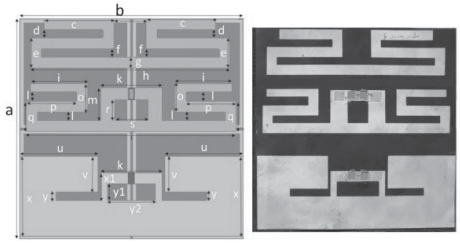

Fig. 3. The top view of the quasi-Yagi antenna in the simulation (left side) and an implemented prototype (right side).

TABLE I
Simulated Antenna Parameters

a	b	c	d	e	f	g	h	i	k	l	m
80	80	25	3	73	3	4	72	21	22	4	11
o	p	q	r	s	x	t	u	v	x1	y1	y2
12	18	11	7	12	29	75	28	13	10	6	17

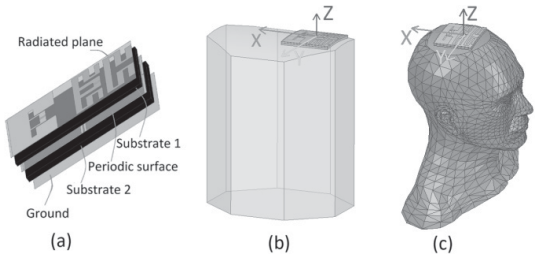

Fig. 4. An exploded view of the antenna (a), the simple head model (b) the anatomical head model (c).

The impedance matching at the two antenna ports is controlled primarily by the geometrical parameters related to the inductive matching loops built around the feed points. Since the radiation efficiency and gain of the antenna are proportional to its electrical size, the best solution is to make use of the available space as efficiently as possible. Here the folding applied on all the antenna elements helped to ensure that the total size of the antenna would not exceed the size of an average adult human head. For achieving the end-fire directivity for Port 1 and broadside directivity for Port 2, the geometrical parameters related to the size and spacing of all antenna elements were optimized within the footprint size of 80 mm by 80 mm, which we considered the maximum feasible size for the considered application.

To account for the influence of the human body on the EM properties of the antenna, we set up two head models illustrated in Fig. 4(b) and Fig 4(c) for simulation of the antenna with the exploded view illustrated in Fig. 4(a). The simplified head human head and neck model in Fig. 4(b) is a polygonal cylinder with a slight curvature on the top (curvature radius: 22 cm) for estimating the impact of bending of the antenna along the human head. As our previous results have indicated that including internal structures of the body in the simulation model of wearable antennas for off-body communications had very limited impact on the simulation results [14], we assigned the cylinder to be homogenously filled and assigned it the dielectric properties of the human skin (ε_r = 41.6, σ = 0.86 S/m at 915 MHz [28]). Here the skin was chosen as the filling material, because it is the closest tissue material to the antenna. Overall, the antenna was developed using the simplified model and final results were verified using ANSYS anatomical human head model of an adult male shown in Fig. 4(c). Similar with the simplified model, this model has the same homogenous filling. In terms of the computational cost, simple model reduced the simulation time and mesh size by the factor of 0.77 and 0.70 compared with the anatomical model, respectively.

C. Simulation Results

The primary parameter for assessing the performance of the RFID tag is the attainable read range. This is determined by the efficiency of the wireless power transfer from the reader to the tag IC and the sensitivity of the RFID's integrated circuit. In free space, the obtainable read range is given

$$d_{tag} = \frac{\lambda}{4\pi}\sqrt{\left\{\frac{4Re(Z_a)Re(Z_{ic})}{|Z_a+Z_{ic}|^2}\right\}\frac{\chi \cdot G \cdot EIRP}{P_{ic}}}, \quad (1)$$

where λ is the wavelength of the reader's signal, the factor in the curly brackets is antenna-IC power transfer efficiency ($0 < \tau \leq 1$) is determined by the matching the impedance of the tag antenna, Z_a, and the RFID IC, Z_{ic}, respectively. G is the gain of the tag antenna, $EIRP$ = 3.28 W is the regulated isotropic equivalent radiated power of the reader, P_{ic} is the turn-on power of the tag IC and χ is the polarisation efficiency between the tag antenna and the incident wave, $0 \leq \chi \leq 1$. The simulation results in Fig. 9 predicted the attainable read range of both antennas at different spatial observation angles, φ and θ, of a spherical coordinate system centered at the tag. The angle θ is zero at the positive z-axis and is swept around the xz-plane, whereas φ = 0° at the positive x-axis and sweeps around the xy-plane.

At the UHF frequency band, the quasi-Yagi tag gave the read range of 3 meters towards the end-fire direction (φ=180°, θ=90°). The dipole-based reflector achieved around 5 meters in the direction pointing upwards from the head (φ=180°, θ=0°). The impedance and directivity of the quasi-Yagi and dipole-based reflector antenna with the RFID IC are shown in Fig. 5 and Fig. 6. At 915 MHz, the input impedance of the dipole antenna was 16+j166 Ω and quasi-Yagi antenna provided input impedance of 42+ j192 Ω. The directivity of the quasi-Yagi antenna reaches peak at φ =180°, θ = 45° with 6 dBi and covers the most of the range from 0° ≤ θ ≤ 90° with acceptable directivity as shown in Fig. 6. The dipole-based reflector directs radiation upwards from the human's head and partly towards the opposite side of the head as compared with the quasi-Yagi

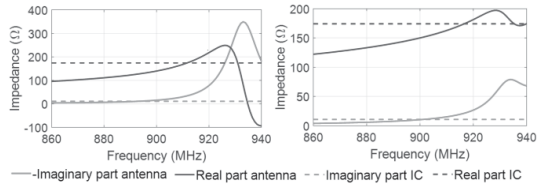

Fig. 5. Simulated (simple model) impedance of Yagi antenna (left side) and dipole antenna (right side).

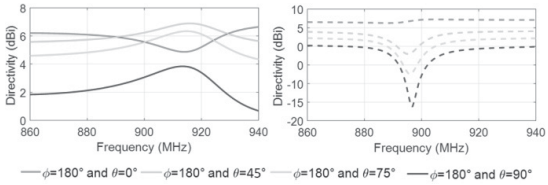

Fig. 6. Simulated (simple model) directivity of the quasi-Yagi antenna (continuous lines at left side) and dipole antenna (dashed lines at right side).

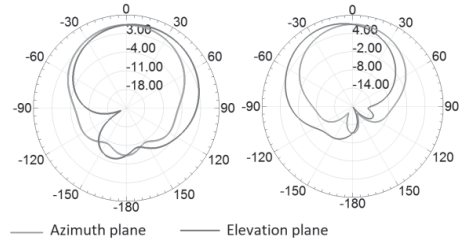

Fig. 7. Simulated (simple model) 2D directivity pattern of the quasi-Yagi antenna (left side) and dipole antenna (right side) at 915 MHz. Elevation where θ = 0° is at z-axis and swept around the xz-plane and Azimuth is plane where φ = 0° at x-axis and swept around the xy-plane.

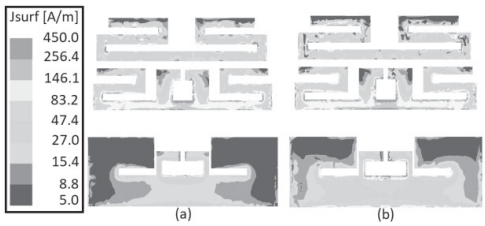

Fig. 8. Amplitude of the surface current density [A/m] at 915 MHz when 100 mW is delivered to (a) quasi-Yagi antenna (b) dipole antenna.

antenna with the maximum directivity of 7 dBi at φ =180°, θ = -15°. The simulated surface current distributions of the proposed quasi-Yagi and dipole antenna at 915 MHz are shown in Fig. 8. For the quasi-Yagi antenna, the current concentrates on the meandered driven element and director, while reflector has weaker surface current. In contrast, the current density is strong at reflector in the dipole antenna simulation.

Table II summarized the simulated radiation properties of the quasi-Yagi and dipole with two head models. In general, the achievable gain and radiation efficiency of. The simple head model illustrated 6% higher than those of the anatomical model. Overall, although antenna performance was limited by the presence of the dissipative biological background and the miniaturization of the device, both Yagi and dipole antenna provide the acceptable gain and directivity for the wearable application.

TABLE II
SIMULATED ANTENNA PARAMETERS

Antenna [Model]	Gain [dBi]	Directivity [dBi]	Radiation efficiency	τ
Quasi-Yagi [Simple]	−1.6	6.7	15%	74%
Quasi-Yagi [Anatomical]	−2	6.6	9%	72%
Dipole [Simple]	−3.5	7	9%	75%
Dipole [Anatomical]	−3.2	6.7	10%	70%

III. Measurement Results and Discussion

A. *Experimental Characterization*

The authors experimented with the RFID tag wirelessly using the Voyantic Tagformance measurement system inside an anechoic chamber. A linearly polarized reader antenna was connected to the Tagformance measurement devices and to a computer to measure the tag performance. All the tag measurements were conducted with head-worn configurations. During the measurements we carefully aligned the tag antennas to match the reader polarization in order to reduce any polarization mismatch. We took two RFID tag measurements with the reader in two different positions at the far field area of the reader. These were in front of the head and above the head to obtain the achievable read ranges of the tags at θ = 90° and θ = 0° of the antenna planes, respectively. The RFID reader had an adjustable transmission frequency from 800 MHz to 1 GHz. During the measurements the threshold power, (P_{th}), was defined as the minimum transmitted power which enables the tag to send a response. The path loss calibration from the reader antenna to the location of the tag was done using the measurement system's reference tag. As detailed in [29], the maximum read range (d_{tag}) of the tag was estimated from its measured threshold power, according to the equation [29]

$$d_{tag} = \frac{\lambda}{4\pi}\sqrt{\frac{EIRP}{\Lambda}\frac{P_{th*}}{P_{th}}}, \qquad (2)$$

where, Λ is a known constant of the measurement system describing the sensitivity of its calibration tag, and P_{th*} is the measured threshold power of the reference tag.

B. *Results and Discussion*

Figures 9 and 10 show the measured attainable read range of both tags and compares it with the simulations. In the direction of the user's line of sight, the frequency trend of the measured

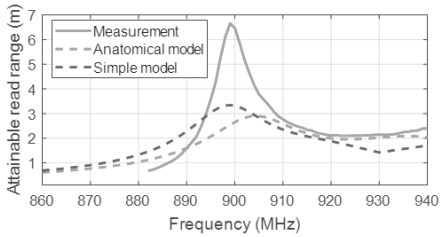

Fig. 9. Attainable read range of the quasi-Yagi tag (EIRP = 3.28 W).

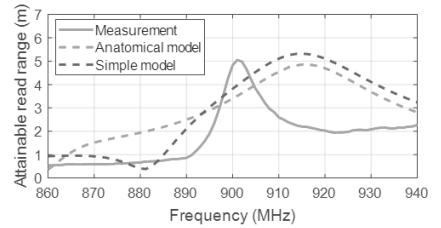

Fig. 10. Attainable read range of the dipole tag (EIRP = 3.28 W).

read range of the quasi-Yagi antenna agrees with the simulation results although the measured peak read range is higher. Both results reached the peak at 900 MHz. The measured peak read range quasi-Yagi antenna was 3 meters higher than the simulated one and was attained around 12 MHz lower frequency than predicted by the simulation. The read range of the dipole-based reflector antenna reached 5 meters at 902 MHz in the upward direction, which was 0.5 meter lower compared with the simulated value. It should be noted that with the latest IC chip, such as the NXP UCODE 8, which has a lower turn-on power of –23 dBm, the detectable distance of the tags can be enhanced by a factor of 1.7, i.e. to 11.5 meters for the quasi-Yagi tag and 8.5 meters for the dipole tag. Finally, we reused the reflector as a dipole antenna, which turns the whole platform from a single ID to a dual-ID headgear UHF RFID tag. This approach enhances the versatility and spatial coverage of the system without increasing its size.

II. Conclusion

Wearable antennas are core technology for modern wireless body-area systems that enable important applications for instance in the healthcare and medicine. We have presented headgear antenna platform comprising quasi-Yagi and dipole antennas that provide directive radiation patterns toward the directions of the user's line of sight and upward from the head, respectively. This was achieved by reusing the reflector element of the quasi-Yagi antenna as a dipole antenna and placing a periodic surface underneath the antenna platform for enhancing the end-fire directivity of the quasi-Yagi antenna. Moreover, we impedance matched the two antennas to RFID microsystems that exhibit low-resistance and capacitive impedance typical of many RF energy harvesting systems, thus achieving a dual-ID passive UHF RFID headgear tag. The measured attainable read ranges of the two tag IDs in the head-worn configuration reached 6.8 and 5 meters for the quasi-Yagi and dipole tags, respectively. This verifies the operation mechanism of the proposed antenna platform and demonstrating its applicability to wearable power harvesting and backscattering communications systems.

References

[1] P. Van Daele, I. Moerman, and P. Demeester, "Wireless body area networks: status and opportunities," General Assembly and Scientific Symposium (URSI GASS), 2014, Beijing, China, 4 pages.

[2] Y. L. Zheng, et al. , "Unobtrusive sensing and wearable devices for health informatics," *IEEE Trans. Biomed. Eng.*, vol. 61, no. 5, pp. 1538–1554, May 2014.

[3] S. Movassaghi, M. Abolhasan, J. Lipman, D. Smith, and A. Jamalipour, "Wireless body area networks: a survey," *IEEE Commun. Surveys Tuts.*, vol. 16, no. 3, pp. 1658–1686, Jan. 2014.

[4] A. Sani, M. Rajab, R. Forster, and Y. Hao, "Antennas and propagation of implanted RFIDs for pervasive healthcare applications," *Proc. IEEE*, vol. 98, no. 9, pp. 1648–1655, Sep. 2010.

[5] J. Grosinger, "Feasibility of backscatter RFID system on the human body," *EURASIP J. Embedded Syst.*, vol. 2013, no. 2, p. 10, Mar. 2013.

[6] W. Mongan, E. Anday, G. Dion, et al, "A multi-disciplinary framework for continuous biomedical monitoring using low-power passive RFID-based wireless wearable sensors," 2016 IEEE International Conference on Smart Computing (SMARTCOMP), St. Louis, Missouri, pp. 1-6, 2016.

[7] S. Milici, S. Amendola, and A. Bianco, "Epidermal RFID passive sensor for body temperature measurements," IEEE RFID technology and applications conference, Sep. 2014, Tampere, Finland, pp. 140-144.

[8] S. Manzari, S. Pettinari, and G. Marrocco, "Miniaturized and tunable wearable RFID tag for body-centric applications," IEEE International Conference on RFID-Technologies and Applications, Nov. 2012, Nice, France, pp. 239-243,.

[9] A. P. Sample, D. J. Yeager, P. S. Powledge, A. V. Mamishev, and J. R. Smith, "Design of an RFID-based battery-free programmable sensing platform," *IEEE Trans. Instrum. Meas.*, vol. 57, no. 11, pp. 2608–2615, Nov. 2008.

[10] G. Marrocco, "Pervasive electromagnetics: sensing paradigms by passive RFID technology," *IEEE Wireless Commun.*, vol. 17, no. 6, pp. 10–17, Dec. 2010.

[11] M. Islam, T. Alam, I. Yahya, and M. Cho, "Flexible radio-frequency identification (RFID) tag antenna for sensor applications," *Sensors*, vol. 18, no. 12, pp. 4212, Nov. 2018.

[12] N. Chahat, M. Zhadobov, and R.Sauleau, "Yagi-Uda textile antenna for on-body communications at 60 GHz," *IEEE Antennas Wirel. Propag. Lett.*, vol. 11, pp. 799-802, April. 2013.

[13] C. Chiu and J. H. Hong, "Circularly polarized tag antenna on an AMC substrate for wearable UHF RFID applications," IEEE-APS Topical Conference on Antennas and Propagation in Wireless Communications, Sep. 2017, Verona, Italy, pp. 71-74.

[14] T. Björninen, "Comparison of three body models of different complexities in modelling of equal-sized dipole and folded dipole wearable passive UHF RFID tags," *Appl. Computational Electromagn. Soc. J.*, vol. 33, no. 6, pp. 706–709, May. 2018.

[15] H. Lee, J. Tak, and J. Choi, "Wearable antenna integrated into military berets for indoor/outdoor positioning system," *IEEE Antennas Wirel. Propag. Lett.*, vol. 16, pp. 1919-1922, March. 2017.

[16] T. Björninen, and F. Yang, "Low-profile head-worn antenna with a monopole-like radiation pattern," *IEEE Antennas Wireless Propag. Lett.*, vol. 15, pp. 794-797, 2016.

[17] D. Le, L. Ukkonen, and T. Björninen, "Quasi-Yagi antenna on a periodic surface for low-profile headgear RFID tag with endfire radiation," Asia-Pacific Conference on Antennas and Propagation, Aug. 2019, Incheon, Korea, 2 pages.

[18] D. Le, L. Ukkonen, and T. Björninen, "Dual-ID headgear UHF RFID tag with broadside and end-fire patterns based on quasi-Yagi antenna," IEEE Asia-Pacific Microwave Conference, Dec. 2019, Singapore, 3 pages.

[19] K. Agarwal, Y. X. Guo, B. Salam, and L. C. W. Albert, "Latex based near-endfire wearable antenna backed by AMC surface," IEEE MTT-S International Microwave Workshop Series on RF and Wireless Technologies for Biomedical and Healthcare Applicrations, Dec. 2013, Singapore, 3 pages.

[20] B. S. Abirami, and E. F. Sundarsingh, "EBG-backed flexible printed Yagi–Uda antenna for on-body communication," *IEEE Trans. Antennas Propag.*, vol. 65, pp. 3762-3765, 2017.

[21] T. Björninen, L. Sydänheimo, L. Ukkonen, "Development and validation of an equivalent circuit model for UHF RFID IC based on wireless tag measurements," Antenna Measurement Techniques Association Symp., October 2012, Bellevue, WA, USA, 6 pages.

[22] Prinel, "Flexible PCB Printed Circuit Boards," 2019.

[23] D. Le, Y. Kuang, L. Ukkonen, and T. Björninen, "Microstrip transmission line model fitting approach for characterization of textile materials as dielectrics and conductors for wearable electronics," *Intl. J. Numerical Modelling Electronic Netw. Dev. Fields*, 2019.

[24] F. Yang, A. Aminian, and Y. Rahmat-Samii, "A novel surface-wave antenna design using a thin periodically loaded ground plane," *Microw. Optical Technol. Lett.*, vol. 47, pp. 240-245, 2005.

[25] F. Yang, and Y. Rahmat-Samii, "Reflection phase characterizations of the EBG ground plane for low profile wire antenna applications," IEEE *Trans. Antennas Propag.*, vol. 51, pp. 2691-2703, 2003.

[26] D. M. Pozar, *Microwave Engineering*. 4th Edition. John-Wiley & Sons, Hoboken, NJ, USA, pp. 558-564.

[27] G. Marrocco, "RFID Grids: Part I—Electromagnetic Theory," *IEEE Trans. Antennas and Propag.*, vol. 59, no. 3, pp. 1019-1026, Mar. 2011.

[28] "Tissue Properties", Accessed on: May. 2018, [Online]. Available: https://www.itis.ethz.ch/virtual-population/tissue-properties/downloads/§

[29] J. Virkki, T. Björninen, S. Merilampi, L. Sydänheimo, and L. Ukkonen, "The effects of recurrent stretching on the performance of electro-textile and screen-printed UHF RFID tags," *Text. Res. J.*, vol. 85, no. 3, pp. 294-301, Feb. 2015.

PUBLICATION IV

Wearable Metasurface-Enabled Quasi-Yagi Antenna for UHF RFID Reader with End-Fire Radiation along the Forearm

Shahbaz Ahmed, Duc Le, Leena Ukkonen, Toni Björninen

IEEE Access. vol. 99

June 2020, doi: 10.1109/ACCESS.2021.3078239

IEEE Access
Multidisciplinary ⋮ Rapid Review ⋮ Open Access Journal

Received April 23, 2021, accepted April 26, 2021, date of publication May 7, 2021, date of current version June 2, 2021.

Digital Object Identifier 10.1109/ACCESS.2021.3078239

Wearable Metasurface-Enabled Quasi-Yagi Antenna for UHF RFID Reader With End-Fire Radiation Along the Forearm

SHAHBAZ AHMED, (Student Member, IEEE), DUC LE, (Student Member, IEEE), LAURI SYDÄNHEIMO, (Member, IEEE), LEENA UKKONEN, (Member, IEEE), AND TONI BJÖRNINEN, (Senior Member, IEEE)

Faculty of Medicine and Health Technology, Tampere University, 33720 Tampere, Finland

Corresponding author: Shahbaz Ahmed (shahbaz.ahmed@tuni.fi)

The work of Shahbaz Ahmed was supported in part by the Doctoral Program in Biomedical Sciences and Engineering through the Faculty of Medicine and Health Technology of Tampere University, in part by the Nokia Foundation, and in part by the Tekniikan Edistämissäätiö. The work of Duc Le was supported in part by the Academy of Finland under Grant 294616 and Grant 327789 and in part by the Nokia Foundation. The work of Toni Björninen was supported by the Academy of Finland under Grant 294616 and Grant 327789.

ABSTRACT We present a quasi-Yagi antenna mounted on a periodic surface for a wearable UHF RFID reader operating in the UHF RFID frequency band centered at 915 MHz. The periodic surface was co-optimized with the antenna to enhance the launching of surface waves to enable the end-fire radiation along the forearm so that a user can identify objects by pointing her/his hand towards them. In addition to the radiation pattern modification, the ground plane of the periodic surface serves the second purpose of isolating the antenna from the human body. We optimized the antenna in a full-wave EM simulator using a simplified cylindrical model of the forearm and in the simulation, it achieved the end-fire directivity of 5.9 dBi along the forearm. In the wireless testing, the quasi-Yagi antenna provided the read range of 3.8 m for a typical UHF RFID tag having 0 dBi gain when the reader's output power was 32 dBm that corresponds with EIRP = 0.56 W and SAR = 0.191 W/kg in our simulations. Considering both, the RFID emission regulations with EIRP = 3.28 W or 4 W and the SAR limit of 1.6 W/kg averaged over 1 gram of tissue, the read range could be further enhanced for reader units with higher output power.

INDEX TERMS Wearable antenna, Yagi antenna, surface wave antenna, periodic surface, UHF RFID, wireless body-area systems.

I. INTRODUCTION

During the past two decades, the versatile passive ultra-high frequency radio-frequency identification technology (UHF RFID) has been researched and developed for numerous applications that extend beyond identification to applications such as wireless sensing [1]–[5] and RFID based real-time localization and tracking of assets [6]–[10]. Most recently, RFID technology has been found a compelling approach to wireless body area systems [11]–[15] where it can be utilized, for instance, in wireless health applications [16]–[20]. Here either the tags, readers, or both, may be integrated into clothing. In this regard, much research has been conducted for achieving efficient and seamlessly cloth-integrable antennas for UHF RFID tags [21]–[25]. However, antennas for wearable RFID readers remain relatively less studied, yet they have been gaining more attention in the recent years [26]–[29].

The fundamental challenge in optimizing wearable antennas is the mitigation of the negative impact arising from the electromagnetic (EM) interaction between the antenna and the dissipative biological tissue. In contrast to wearable passive tags, which are not active transmitters but backscatter the reader's signal, the reader antenna transmits relatively high-power levels up to 4 W EIRP depending on the governing RFID emission regulations. Thus, the EM optimization of a reader antenna must also consider the specific absorption rate (SAR) in conjunction with the regular antenna performance parameters [30].

In the previous research, wearable reader antennas attached to gloves [28], wrapped around the wrist [27] and ankle [26] have been studied. They all read the tags from a direction

The associate editor coordinating the review of this manuscript and approving it for publication was Chan Hwang See.

TABLE 1. Dielectric properties of body tissue at 915 Mhz [34].

Tissue	σ (S/m)	ε_r
Skin	0.8555	41.587
Fat	0.050242	5.4673
Muscle	0.93146	55.114
Bone	0.13926	12.486

orthogonal to the body surface where the reader antenna is worn. However, few wearable antennas with end-fire radiation along the body surface have been reported. A wearable quasi-Yagi near-field UHF RFID reader antenna with end-fire radiation properties integrated into a smart glove is reported in [29], [31]. Through the analysis of the near electric and magnetic fields, the authors confirmed the end-fire property, and in experiments, the attainable tag read range was found to be 0.33 m.

In our earlier work [32], we developed a head-worn quasi-Yagi RFID tag, where the antenna included a periodic surface made up of a 2-by-2 grid of square loops. By applying the folding technique, we achieved the small antenna size of 0.25λ × 0.25λ at 915 MHz or 80 mm × 80 mm, which befits the human head. However, the antenna in this work was developed for RFID tags. As a specific feature and inductive loop was included in the driven element to achieve complex conjugate impedance matching between the antenna and the RFID IC. In another study [28], the authors developed a slotted patch and a split ring resonator RFID reader antenna integrated into work gloves. The antennas exhibit a broadside radiation pattern pointing in the direction approximately orthogonal to the hand's back. The ground plane in the slotted patch antenna suppressed the antenna-body coupling and thereby enabled better EM performance and the tag read range of 3 m with a transmission power of 30 dBm.

In this paper, we present a wearable quasi-Yagi reader antenna on a textile substrate conforming to the forearm. The antenna's radiation pattern is directive along the arm so that a user can identify objects by pointing her/his hand towards them. The novel feature of the end-fire radiation pattern along the body surface is achieved by inserting a periodic surface between the antenna and the arm and co-optimizing the two for a maximally directive radiation pattern. This way the end-fire directivity is enhanced by the periodic surface that supports the launching of the surface waves at the operating frequency of the antenna.

II. HUMAN BODY MODEL AND ANTENNA MODELLING

The human body comprises various biological materials exhibiting electrical conductivity and relative permittivity tens of times higher than most conventional electronics materials [34]. The human forearm includes multiple tissue types, such as skin, fat, muscle, and bone. Although the associated dielectric properties are available in the literature (see Table 1), in practice, the thicknesses of these layers are difficult to measure and are subjective to the human anatomy.

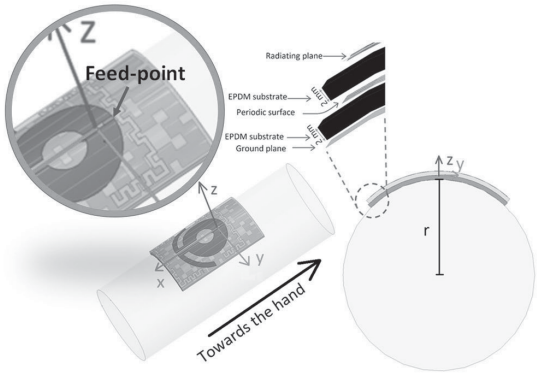

FIGURE 1. Wearable quasi-Yagi antenna mounted on the cylinder modelling the forearm (left side), the front view (right side) and exploded view of the model (top side).

Therefore, a simplistic approach is needed for modeling the electromagnetic properties of the wearable antenna effectively. To model the electromagnetic energy dissipation in the biological tissues and the relative permittivity, we used a homogenous forearm model comprising skin, which is comparatively nearest to the antenna and among most energy dissipative materials ($\sigma = 0.855$ S/m and $\varepsilon_r = 41.85$ at 915 MHz) [34]. The radius of the human forearm model estimates an average adult male. The radius and length of the cylinder was set to 46 mm and 250 mm, respectively. Figure 1 shows the forearm model, the antenna structure mounted on it, and the coordinate system which we will use throughout this work in the radiation pattern analysis.

The quasi-Yagi antenna is a planar, low-profile, structure that provides a directive end-fire beam in free space environment [32]. As shown in our previous work on the headgear RFID tag [32], in the wearable configuration, the end-fire radiation property can be restored by mounting the quasi-Yagi antenna on a periodic surface. Thus, we considered this configuration viable also for the forearm reader antenna.

The initial step of developing the quasi-Yagi antenna is considering the antenna geometry shown in Fig. 1 and Fig. 2. The quasi-Yagi antenna includes the driven element, typically a folded dipole, and parasitic elements operating as a reflector and directors. One of the most challenging tasks in this antenna development is to fit the antenna in the forearm's limited space and maintain the electrical length of 0.5λ or 80 mm of the antenna elements. To solve this, we applied the meandering and folding technique for all the antenna elements and reduced the element spacing as shown in Fig. 2. As a result, the total size of the radiator is 67 mm × 95 mm and the total lengths of the director and reflector is 243 mm (0.74λ) and 263 mm (0.8λ), respectively. The driven element was folded as two loops. The first loop with radius r_1 is optimized for impedance matching and the second loop with radius r_2 increases the total length of the driven element to 253 mm (0.77λ).

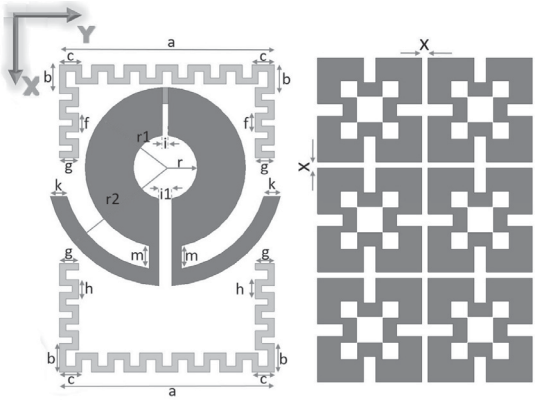

a	b	c	f	g	h	i	i_1	m	r	r_1	r_2	x
67	9	7	7	6	6	2	4	7	10	25	37	2

FIGURE 2. Top view of the quasi-Yagi antenna and periodic surface and the periodic surface with the geometrical parameters reported in millimeters.

The next step of developing the antenna on forearm is to optimize the periodic surface made up of a grid of unit cells. Following the principle from [35], we selected the non-grounded via-free configuration for the unit cells that instead of generating stop band for the surface-waves, enhances them and thereby is suitable for creating surface wave antennas. Considering the reflection phase criteria of $90° \pm 45°$ that was found to support the 50-Ω matching of wire type antenna on the periodic surface [36], we took this as the initial target. In addition to the surface-wave property, in our application the ground plane of the periodic surface helps to suppress the undesired antenna-body EM coupling.

As the unit cell structure, we selected the square loop configuration introduced in [46], because this unit cell type balances the simplicity of fabrication and the ease of adapting the geometry to obtain the targeted reflection phase. It was originally designed for 9.5 GHz, but the structure permits us to scale its dimensions to our target frequency of 915 MHz without increasing the size beyond with is feasible considering the size available on the forearm. The optimization of the unit cell geometry was done in ANSYS High-Frequency Structure Simulator (HFSS) v19.1, which is a full-wave electromagnetic field solver based on the finite element method, using the Floquet boundary condition (see Fig. 3). The target was obtaining the $90° \pm 45°$ reflection phase response in 915 MHz UHF RFID band. In the simulation, the impact of bending on unit cell reflection phase was also considered. We bent the unit cell with various radii of curvature realistic to our application and found the reflection phase to remain stable. The simulation model and the reflection phase are shown in Fig. 3 and the final layout of the unit cell is shown in Fig. 4. Next, considering the size of the forearm, we organized the unit cells into a 2-by-3 grid as shown Fig. 2 to form the periodic surface.

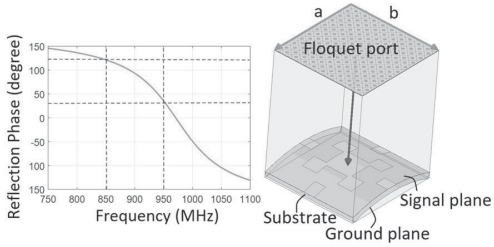

FIGURE 3. Floquet port simulation of the reflection phase of the periodic surface.

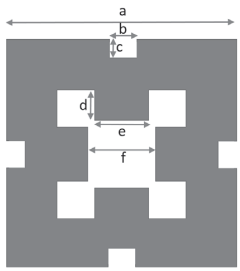

a	b	c	d	e	f
34	4	3	4.5	8	10

FIGURE 4. The unit cell of periodic surface with the geometrical parameters reported in millimeters.

Finally, we attached the radiating plane on top of the periodic surface and installed the whole antenna structure on the forearm model as shown in Fig. 1. From the cross-sectional view, the whole structure of the antenna consists of 5 layers (see Fig. 1). The first layer of the antenna is the radiating plane. The periodic surface layer was sandwiched between two textile layers of flexible, ethylene-propylene-diene-monomer (EPDM) rubber foam with a thickness of 2 mm ($\varepsilon_r = 1.53$, $\sigma = 0.01$ S/m [32]). The last layer is the ground plane that can isolate the antenna on the skin to prevent unexpected interaction between the human body and electromagnetic fields. The overall dimensions of the antenna are $0.22\lambda \times 0.33\lambda$.

We co-optimized the quasi-Yagi antenna and the periodic surface to achieve maximized realized gain and directivity exhibiting end-fire radiation pattern at 915 MHz frequency. To assess how close the directivity along the forearm (D_{arm}) comes to the peak value (D_{peak}) considering all spatial directions, we define $\Delta_{dir} = D_{arm}/D_{peak}$. In terms of our design, the target is to achieve $\Delta_{dir} = 1$ with as high as possible value of D_{peak}. Figure 5(a) shows Δ_{dir} and the quasi-Yagi antenna's peak directivity with and without the periodic surface. From the results, it is evident that without the periodic surface both D_{peak} and Δ_{dir} are tending toward local minima near the targeted 915 MHz UHF RFID band and the insertion of the periodic surface reverses this, so that the quantities attain local maxima instead, as desired. With the periodic surface we have $D_{peak} = 5.9$ dBi and $D_{arm} = 5.3$ dBi.

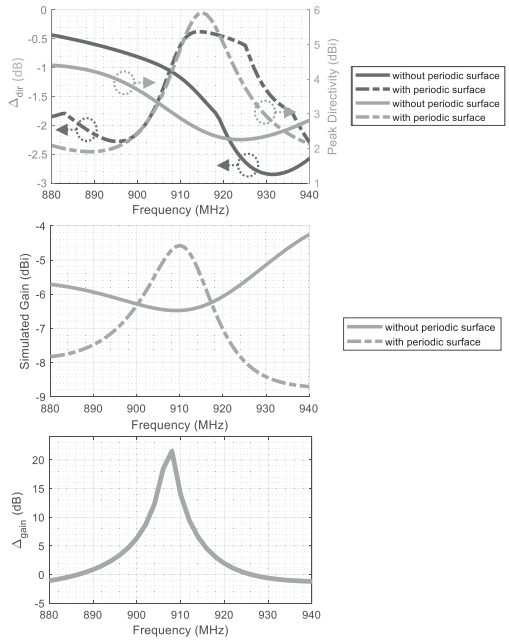

FIGURE 5. (a) Peak directivity, delta, and (b) gain of the quasi-Yagi reader antenna with and without periodic surface (c) front to back lobe ratio for simulated gain.

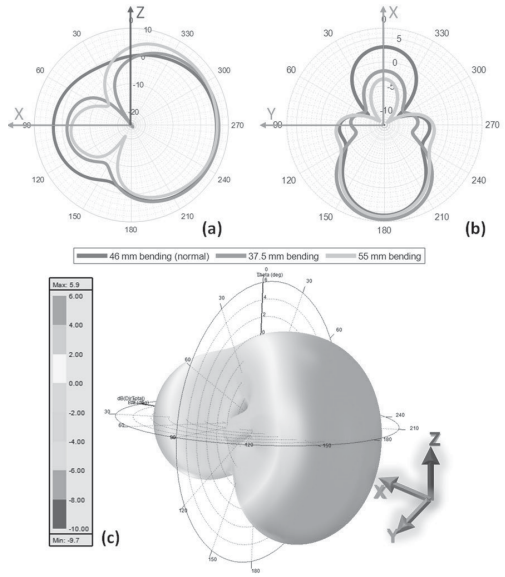

FIGURE 6. Directivity pattern in (a) XZ and (b) XY planes. (c) simulated 3D directivity pattern of quasi-Yagi antenna exhibiting end-fire radiation properties in the forearm direction (46 mm bending).

Correspondingly, Fig. 5(b) shows a comparison of the simulated gain, with and without the periodic surface, where the gain with the periodic surface is improved to a value of −5.5 dBi in the forearm direction. We defined Δ_{gain} as the ratio G_{front}/G_{back}, where the G_{front} and G_{back} is the gain in ($\theta = 90°$, $\varphi = 180°$) and ($\theta = 90°$, $\varphi = 0°$) directions, respectively. In Fig. 5(c), Δ_{gain} achieves a value of 5 dB at 915 MHz frequency indicating that maximum power is radiated in the − x direction i.e. away from the person wearing the antenna (Fig. 1).

As discussed earlier, the curvature of the forearm defines the bending degree of the antenna and may vary with the body anatomy, we have considered various radii of the human forearm i.e. r varies between 37.5 mm and 55 mm. Fig. 6(a) and Fig. 6(b) shows the 2D directivity pattern of the quasi-Yagi antenna in XZ and XY planes, respectively. Figures also elaborates the impact of bending on the antenna's peak directivity. Although the bending does not significantly impact the peak directivity or Δ_{dir} of the antenna and the reflection phase of the periodic surface, yet the end-fire radiation defined by Δ_{gain} property is improved with various bending degrees i.e. the back lobe reduces significantly. Fig. 6(c) shows the 3D directivity pattern of the quasi-Yagi antenna exhibiting the end-fire directivity pattern of the antenna along the direction of the arm ($\theta = 270°$, $\varphi = 180°$) with a peak directivity of −5.9 dBi.

The reader quasi-Yagi antenna without the periodic surface exhibits input impedance of $48 + 82j\ \Omega$, as shown in the Fig. 7(a). However, the periodic surface directs the peak surface current of 49 A/m into driver of the quasi-Yagi antenna, achieving the end-fire radiation characteristics for the antenna. Figure 8 shows the surface with and without the periodic surface when 1 W of power is fed to the antenna. With the periodic surface, the antenna exhibits input impedance of $4 + 25j\ \Omega$, as shown in Fig. 7(a). As the primary objective of our work is to achieve the end-fire radiation properties, we have used a matching circuit designed in Advanced Design System (ADS), shown in the Fig. 7(b), to resonate the antenna at the 915 MHz frequency. We also studied the impact of various curvature of the human forearm on the resonance frequency of the antenna. Figure 9 shows the simulated reflection coefficient of the antenna mounted on various forearm sizes. The antenna resonates at 915 MHz with a reflection coefficient of −25 dB at standard bending of 46 mm. The simulation results also show that the antenna's frequency bandwidth splits into a dual band with the change in the bending curvature. However, the targeted frequency of 915 MHz remains inside the −10 dB S_{11} bandwidth under the various curvatures of the forearm.

For the antennas operation in the human body's proximity, the transmission power is limited by the specific absorption rate and is regulated by the US FCC [37], limiting SAR to 1.6 W/kg averaged over 1 g of tissues. Consequently, to determine the maximum SAR complaint transmission power ($P_{t,max}$) for the quasi-Yagi reader antenna is expressed as [38]

$$P_{t,max} = \frac{1.6W/kg\left(1 - |S_{11}|^2\right)P_{test}}{SAR_{max}}, \tag{1}$$

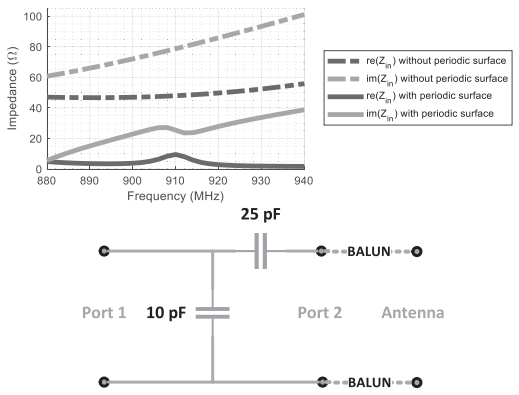

FIGURE 7. (a) Input impedance of the antenna with and without the periodic surface (b) schematic of the matching circuit designed to resonate the antenna at 915 MHz frequency.

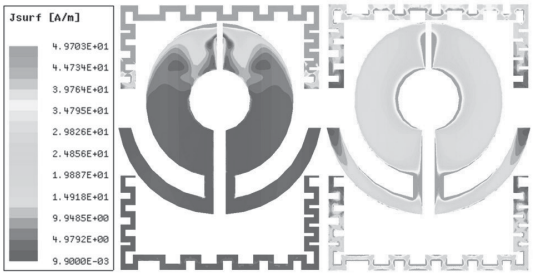

FIGURE 8. Surface current distribution at the quasi-Yagi antenna with and without the periodic surface (left to right).

where P_{test} is the power available from the numerical test source that we set to 1 W. In the simulation, the maximum SAR that occurs in the tissue nearest to the radiating antenna is 0.9 W/kg, and the maximum SAR compliant transmission power is calculated as 41.2 dBm using (1). This is comparatively higher than reported in the previous works, indicating our antenna exhibits lower SAR. Considering the emission limits of EIRP = 3.28 W or EIRP = 4 W set for UHF RFID systems, the antenna could transmit 40.6 dBm or 41.5 dBm, respectively. Overall, we conclude the that the output power is limited nearly equally by both, the SAR and emission limits. However, this output power limit is notably high and especially for mobile RFID reader units, the output power is expected to be an order of lower magnitude. Thus, in the wireless testing we present in Section IV, we have used the output power of 32 dBm.

III. TEST TAG FOR THE READER ANTENNA CHARACTERIZATION

One of the most significant parameters of a body-worn antenna is its realized gain, which is determined by the input reflection coefficient, directivity, and the radiation efficiency of the antenna. However, the measurement of the realized gain a wearable antenna in body-worn configuration by using conventional techniques becomes significantly difficult. Therefore, in this work we have adopted an alternative approach applicable specifically to RFID reader antennas by utilizing an RFID tag analogous to the reference gain antenna in the classical far field antenna measurement.

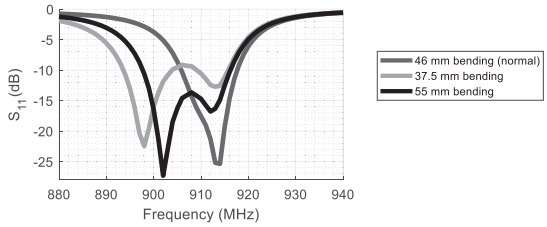

FIGURE 9. Reflection coefficient of the quasi-Yagi antenna mounted on various forearm sizes.

For this purpose, we have first designed and implemented a dipole type test tag antenna shown in Fig. 10. The test tag was designed based on the regular embedded inductive loop matching method [39]. The main target of the design was to achieve the antenna input impedance that equals the complex conjugate impedance of the NXP UCODE G2iL series RFID IC [40] having the turn on power of $P_{ic0} = -18$ dBm. For this purpose, the antenna geometry (primarily the parameters L_{s1}, W_{s1} and W_{s2}) was adapted in ANSYS High-Frequency Structure Simulator (HFSS) v19.1. The impedance of the chip was estimated by using an equivalent circuit comprising capacitance and resistance connected in parallel [28].

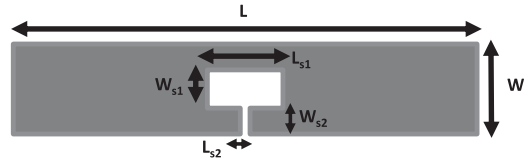

L	W	L_{S1}	W_{S1}	L_{S2}	W_{S2}
95	25	15.5	8.5	2	5.75

FIGURE 10. Structure of the test tag antenna and its dimensional parameters given in millimeters.

The manufactured test tag was characterized using Voyantic Tagformance Pro measurement system [27]. For the characterization of fully assembled UHF RFID tags, the system enables the recording of the lowest continuous-wave output power (threshold power: P_{th}) of the reader for which the tag under test backscatters a valid 16-bit random number as a response to the reader's query command in ISO 18000-6C communication standard. It also provides the estimation of the path loss factor L_{iso} from the device output to the location of the tag under test. This is achieved through the threshold power measurement performed on the manufacturer's system reference tag with accurately known properties that enable the computation of L_{iso}. This enables us to compute the realized

TABLE 2. Comparison with the contemporary research work.

Ref.	Freq. (GHz)	Gain (dBi)	Size (mm)	Thickness (mm)	Relative size	Read range (m)*	RFID reader	Pattern type
[28]	0.866	−4	80×62	4	$0.23\times0.18\ \lambda_o$	1.5	Yes	1
[26]	0.866	2	80×70	1.52	$0.23\times0.20\ \lambda_o$	1.45	Yes	2
[31]	0.880	−5	63×65	--	$0.18\times0.19\ \lambda_o$	2	Yes	1
[42]	0.866	−1.31	140×100	4	$0.40\times0.29\ \lambda_o$	2.3	Yes	1
[45]	0.915	−10.9	360×360	5	$1.19\times1.1\ \lambda_o$	2.1	No	1
[47]	2.47	0.1	50×50	9.5	$0.41\times0.41\ \lambda_o$	1.29	No	2
[48]	0.860	1	90×49	4	$0.25\times0.14\ \lambda_o$	4.23	No	1
[49]	0.868	−2.6	87×77	4	$0.25\times0.22\ \lambda_o$	2.76	No	1
Our work	0.915	−5.5	67×108	4	$0.22\times0.33\ \lambda_o$	2	Yes	2

*Estimated read ranges (S_{max}) based on the test tag used in our work ($P_{rx} = -18$ dBm) and calculated by equation (5) assuming $P_{tx} = 25$ dBm.

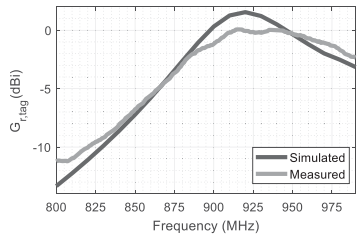

FIGURE 11. Measured and simulated realized gain of the test tag antenna.

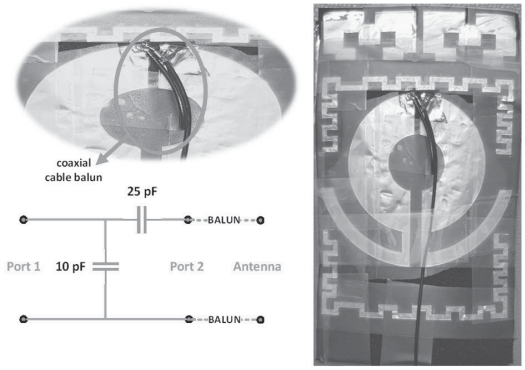

FIGURE 12. Matching network, balun, and the antenna connection configuration for the reflection coefficient measurement (left), and the fabricated wearable quasi-Yagi reader antenna (right).

gain $G_{r,tag}$ of the test tag antenna as detailed in [40]

$$G_{r,tag} = \frac{P_{ic0}}{L_{iso}P_{th}}, \tag{2}$$

where P_{th} is the threshold power of the test tag. Fig. 15(a) shows the measurement setup for the characterization of the test tag. First the Tagformance is calibrated using the reference tag and later, the test tag is measured. As seen from the results in Fig. 11, the realized gain versus frequency peaks at 915 MHz, as desired, with the simulated and measured values of 1 dBi and 0 dBi, respectively. Later, we will utilize the measured realized gain of the test tag in the characterization of the quasi-Yagi reader antenna and to demonstrate the attainable read range of a common RFID tag.

IV. READER ANTENNA MEASUREMENT AND RESULTS

As the primary aim of our work is to demonstrate the end-fire radiation property of the reader antenna achieved by utilizing the periodic surface, the reader antenna is not self-matched to 50 Ω. Thus, a matching circuit is used to match the input impedance of the reader antenna to the standard 50 Ω impedance. To achieve this, we first measured the feed-point impedance of the antenna ($8 + 9j$ Ω at 915 MHz) through a balun made-up of a coaxial cable. The impedance of the antenna through a balun made-up of coaxial cable (see Fig. 13), that suppresses the common mode currents as the driven element of the quasi-Yagi antenna is a dipole (differential antenna) [42]. After this we developed a simple two-component L-matching circuit [43] that is shown in Fig. 12 to transform the antenna's feedpoint impedance

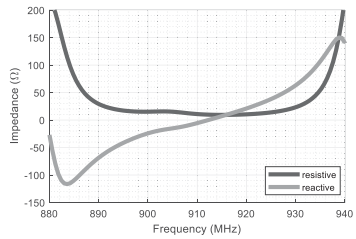

FIGURE 13. Input impedance of the antenna before matching network.

of $8 + 9j$ Ω at 915 MHz to the input impedance of 50 Ω seen through the matching circuit. As seen from Fig. 13, both the simulation and measurement show that the matching circuit provides the desired impedance transformation at 915 MHz.

Next, we measured the realized gain (G_R) of the wearable quasi-Yagi antenna using the test tag presented in Section III. In the experimental arrangement shown in Fig. 15b, the reader antenna was attached on the forearm which was pointed towards the test tag that was placed at distance of 1 meter from the reader antenna. In the experiment the reader antenna was placed directly on the skin to achieve an identical scenario to the simulation. We then connected the reader antenna to the

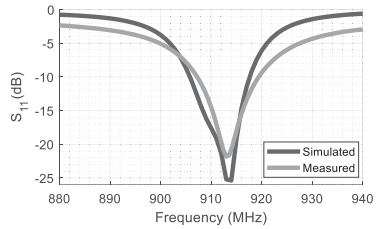

FIGURE 14. Simulated and measured reflection coefficient of the quasi-Yagi antenna in body worn condition.

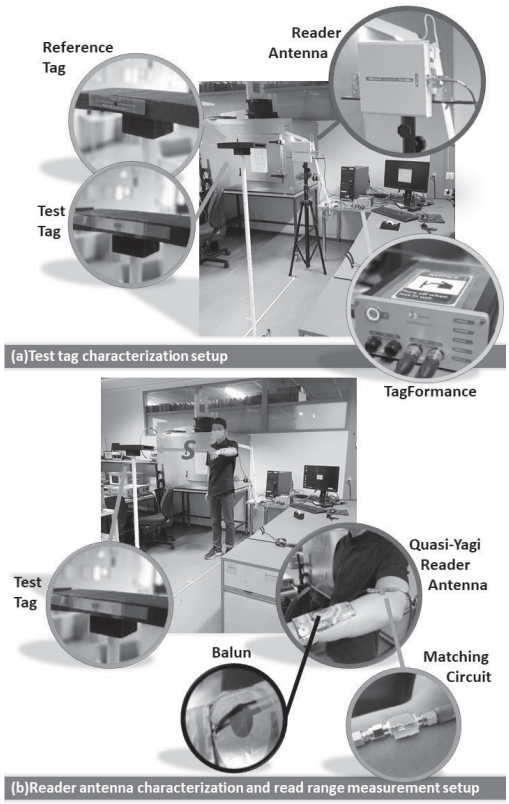

FIGURE 15. The measurement setup for (a) test tag antenna characterization (b) reader antenna characterization and read range measurement.

Voyantic Tagformance Pro measurement system introduced in Section III and recorded the threshold power of the test tag using the wearable reader. This enables us to solve the realized gain of the wearable quasi-Yagi reader antenna (G_R) from Friis' transmission formula

$$P_{rx} = G_R G_{r,tag} L_{cab} \left(\frac{\lambda}{4\pi s}\right)^2 P_{tx}, \tag{3}$$

where $L_{cab} = -1.1$ dB is the power loss factor, we measured for the cable connecting the quasi-Yagi antenna to the

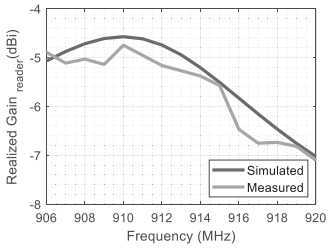

FIGURE 16. Realized gain of the quasi-Yagi reader antenna in the body-worn configuration.

RF output of the Tagformance device. For comparison, the simulated realized gain of the reader antenna is given by

$$G_R = G\left(1 - |s_{11}|^2\right), \tag{4}$$

where G and s_{11} are the simulated gain and reflection coefficient of the quasi-Yagi antenna. In Fig. 16, the simulated realized gain shows good agreement with the calculated realized gain over the -10 dB S_{11}-bandwidth of the antenna at the end-fire direction (see Fig. 14). The measured realized gain of the quasi-Yagi antenna is -5.5 dBi at the operating frequency of 915 MHz. To estimate the corresponding attainable tag read range versus transmission power, we varied the transmission power P_{tx}, so that, the power delivered to the quasi-Yagi antenna ($P_{tx}L_{cab}$) was between 5 dBm and 32 dBm. We then manually moved the test tag further away from the reader antenna and measured the critical antenna separation (s_{max}) that corresponds with the scenario that the tag antenna captures barely enough power to turn on the RFID IC; i.e. $P_{rx} = P_{ic0} - 18$ dBm. This distance is the attainable read range of the tag for a given transmission power. For the comparison with the simulation, we have

$$s_{max} = \frac{\lambda}{4\pi}\sqrt{\frac{G_{r,tag} G_R L_{cab} P_{tx}}{P_{rx}}}, \tag{5}$$

from equation (3) and we can compute s_{max} using the simulated realized gains of the test tag and the quasi-Yagi reader antenna. Fig. 17 shows the results. The measured and calculated read range shows good agreement with an approximately constant relative difference that is 150 cm at 32 dBm transmission power. Since both graphs show the same trend versus the transmission power, we expect the difference to the primarily due to the lower measured realized gains of the tag and reader antennas as compared with the simulation and not because of multipath propagation effects.

Table 2 summarizes some of the contemporary wearable reader antennas with estimated attainable read ranges for the test tag, introduced in the section III. We calculated the attainable read ranges of the wearable antenna through equation (5), when 25 dBm transmission power is fed to the antenna. Moreover, we classified the antennas based on the radiation pattern to Type 1 and Type 2, which denote radiation

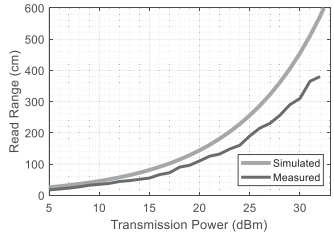

FIGURE 17. Attainable read range of the tag ($G_{r,tag} = 0$ dBi) with the quasi-Yagi reader antenna at 915 MHz.

to an off-body direction and along the body surface, respectively. Even though the antennas from several other works, especially [26], [47], and [48], provide notably high gain, among the radiation pattern Type 2 antennas, our antenna provides the highest read range. However, it should be noted that the antenna [47] is not originally proposed as a reader antenna, operates at 2.47 GHz and thus it's hypothetical read range is affected also by the shorter operating wavelength.

V. CONCLUSION

Wearable antennas are fundamental to smart clothing in wireless body-area systems. We have presented, a metasurface-enabled quasi-Yagi UHF RFID reader antenna worn on the forearm and optimized to detect RFID tags in the pointing direction of the arm. The antenna that conforms on the forearm, comprises two layers of low-permittivity textile material, where the bottom layer is a periodic surface on a ground plane. The top layer that carries the quasi-Yagi radiator, is suspended on the periodic surface. Due to the body proximity, the quasi-Yagi radiator alone does not provide end-fire radiation along the body surface, but by co-optimizing the periodic surface for the enhanced launching of the surface waves with the quasi-Yagi radiator, we achieved the end-fire directivity of 5.5 dBi. The ground plane of the periodic surface also decouples the radiator from the body and reduces the SAR. Our simulations showed that the maximum SAR-compliant power of the antenna is 41 dBm, which is an order of magnitude higher than a typical output power level of a mobile RFID reader. In our practical testing, we were able to detect a regular dipole type RFID tag at 3.8 meters with the reader's output power of 32 dBm (EIRP = 0.56 W) at 915 MHz.

ACKNOWLEDGMENT

(Shahbaz Ahmed and Duc Le contributed equally to this work.)

REFERENCES

[1] S. Genovesi, F. Costa, M. Borgese, F. A. Dicandia, A. Monorchio, and G. Manara, "Chipless RFID sensor for rotation monitoring," in *Proc. IEEE Int. Conf. RFID Technol. Appl. (RFID-TA)*, Warsaw, Poland, Sep. 2017, pp. 233–236.

[2] H. He, X. Chen, L. Ukkonen, and J. Virkki, "Clothing-integrated passive RFID strain sensor platform for body movement-based controlling," in *Proc. IEEE Int. Conf. RFID Technol. Appl. (RFID-TA)*, Pisa, Italy, Sep. 2019, pp. 236–239.

[3] S. Amendola, L. Bianchi, and G. Marrocco, "Movement detection of human body segments: Passive radio-frequency identification and machine-learning technologies," *IEEE Antennas Propag. Mag.*, vol. 57, no. 3, pp. 23–37, Jun. 2015.

[4] H. Ding, J. Han, L. Shangguan, W. Xi, Z. Jiang, Z. Yang, Z. Zhou, P. Yang, and J. Zhao, "A platform for free-weight exercise monitoring with passive tags," *IEEE Trans. Mobile Comput.*, vol. 16, no. 12, pp. 3279–3293, Dec. 2017.

[5] A. E. Abdulhadi and T. A. Denidni, "Self-powered multi-port UHF RFID Tag-Based-Sensor," *IEEE J. Radio Freq. Identificat.*, vol. 1, no. 2, pp. 115–123, Jun. 2017.

[6] J. Zhang, X. Wang, Z. Yu, Y. Lyu, S. Mao, S. C. Periaswamy, J. Patton, and X. Wang, "Robust RFID based 6-DoF localization for unmanned aerial vehicles," *IEEE Access*, vol. 7, pp. 77348–77361, Jun. 2019.

[7] L. Shen, Q. Zhang, J. Pang, H. Xu, and P. Li, "PRDL: Relative localization method of RFID tags via phase and RSSI based on deep learning," *IEEE Access*, vol. 7, pp. 20249–20261, Jan. 2019.

[8] A. Fahim, T. Elbatt, A. Mohamed, and A. Al-Ali, "Towards extended bit tracking for scalable and robust RFID tag identification systems," *IEEE Access*, vol. 6, pp. 27190–27204, May 2018.

[9] F. Xiao, Z. Wang, N. Ye, R. Wang, and X.-Y. Li, "One more tag enables fine-grained RFID localization and tracking," *IEEE/ACM Trans. Netw.*, vol. 26, no. 1, pp. 161–174, Feb. 2018.

[10] X. Liu, X. Xie, K. Li, B. Xiao, J. Wu, H. Qi, and D. Lu, "Fast tracking the population of key tags in large-scale anonymous RFID systems," *IEEE/ACM Trans. Netw.*, vol. 25, no. 1, pp. 278–291, Feb. 2017.

[11] A. Sani, M. Rajab, R. Foster, and Y. Hao, "Antennas and propagation of implanted RFIDs for pervasive healthcare applications," *Proc. IEEE*, vol. 98, no. 9, pp. 1648–1655, Sep. 2010.

[12] R. Lodato, V. Lopresto, R. Pinto, and G. Marrocco, "Numerical and experimental characterization of through-the-body UHF-RFID links for passive tags implanted into human limbs," *IEEE Trans. Antennas Propag.*, vol. 62, no. 10, pp. 5298–5306, Oct. 2014.

[13] R. C. Hadarig, M. E. de Cos, and F. Las-Heras, "UHF dipole-AMC combination for RFID applications," *IEEE Antennas Wireless Propag. Lett.*, vol. 12, pp. 1041–1044, Aug. 2013.

[14] M. A. S. Tajin and K. R. Dandekar, "Pattern reconfigurable UHF RFID reader antenna array," *IEEE Access*, vol. 8, pp. 187365–187372, Oct. 2020.

[15] Y. Kuang, L. Yao, W. Zhang, D. Zhou, H. Luan, and Y. Qiu, "A novel textile dual-polarized antenna potentially used in body-centric system," in *Proc. IEEE Int. Conf. RFID Technol. Appl. (RFID-TA)*, Foshan, China, Sep. 2016, pp. 77–80.

[16] E. Moradi, L. Sydanheimo, G. S. Bova, and L. Ukkonen, "Measurement of wireless power transfer to deep-tissue RFID-based implants using wireless repeater node," *IEEE Antennas Wireless Propag. Lett.*, vol. 16, pp. 2171–2174, May 2017.

[17] J. J. Baek, S. W. Kim, K. H. Park, M. J. Jeong, and Y. T. Kim, "Design and performance evaluation of 13.56-MHz passive RFID for E-Skin sensor application," *IEEE Microw. Wireless Compon. Lett.*, vol. 28, no. 12, pp. 1074–1076, Dec. 2018.

[18] G. Scotti, S.-Y. Fan, C.-H. Liao, and Y. Chiu, "Body-implantable RFID tags based on ormocer printed circuit board technology," *IEEE Sensors Lett.*, vol. 4, no. 8, pp. 1–4, Aug. 2020.

[19] C. Miozzi, S. Nappi, S. Amendola, C. Occhiuzzi, and G. Marrocco, "A general-purpose configurable RFID epidermal board with a two-way discrete impedance tuning," *IEEE Antennas Wireless Propag. Lett.*, vol. 18, no. 4, pp. 684–687, Apr. 2019.

[20] I. Bouhassoune, R. Saadane, and A. Chehri, "Wireless body area network based on RFID system for healthcare monitoring: Progress and architectures," in *Proc. 15th Int. Conf. Signal-Image Technol. Internet-Based Syst. (SITIS)*, Sorrento, Italy, Nov. 2019, pp. 416–421.

[21] H. Xiaomu, S. Yan, and G. A. E. Vandenbosch, "Wearable button antenna for dual-band WLAN applications with combined on and off-body radiation patterns," *IEEE Trans. Antennas Propag.*, vol. 65, no. 3, pp. 1384–1387, Mar. 2017.

[22] C. Mao, P. L. Werner, and D. H. Werner, "Low-profile textile antenna with omni-directional radiation for wearable applications," in *Proc. Int. Appl. Comput. Electromagn. Soc. Symp. (ACES)*, Miami, FL, USA, Apr. 2019, pp. 1–2.

[23] S. Kumar, P. Ranjan, S. Arava, K. P. Kalyan, and T. S. Chand, "Design and analysis of dielectric resonator antenna for wearable applications," in *Proc. Int. Conf. Vis. Towards Emerg. Trends Commun. Netw. (ViTECoN)*, Vellore, India, Mar. 2019, pp. 1–3.

[24] F. Lagha, S. Beldi, and L. Latrach, "Design of UHF RFID body-worn textile tag for wireless applications," in *Proc. IEEE Int. Conf. Design Test Integr. Micro Nano-Syst. (DTS)*, Gammarth-Tunis, Tunisia, Apr. 2019, pp. 1–4.
[25] H. He, X. Chen, O. Mokhtari, H. Nishikawa, L. Ukkonen, and J. Virkki, "Fabrication and performance evaluation of carbon-based stretchable RFID tags on textile substrates," in *Proc. Int. Flexible Electron. Technol. Conf. (IFETC)*, Ottawa, ON, Canada, Aug. 2018, pp. 1–5.
[26] K. Jebbawi, M. Egels, and P. Pannier, "Design of an ultra-wideband UHF RFID reader antenna for wearable ankle tracking applications," in *Proc. Eur. Microw. Conf. Central Eur. (EuMCE)*, Prague, Czech Republic, May 2019, pp. 525–528.
[27] M. Daiki and E. Perret, "Segmented solenoid coil antenna for UHF RFID near-field reader applications," *IEEE J. Radio Freq. Identificat.*, vol. 2, no. 4, pp. 210–218, Dec. 2018.
[28] S. Ahmed, S. T. Qureshi, L. Sydanheimo, L. Ukkonen, and T. Bjorninen, "Comparison of wearable E-textile split ring resonator and slotted patch RFID reader antennas embedded in work gloves," *IEEE J. Radio Freq. Identificat.*, vol. 3, no. 4, pp. 259–264, Dec. 2019.
[29] R. K. Singh, A. Michel, P. Nepa, and A. Salvatore, "Glove integrated dual-band Yagi reader antenna for UHF RFID and Bluetooth application," in *Proc. Int. Workshop Antenna Technol. (iWAT)*, Bucharest, Romania, Feb. 2020, pp. 1–3.
[30] A. S. Andrenko, Y. Shimizu, and K. Wake, "SAR measurements of UHF RFID reader antenna operating in close proximity to a flat phantom," in *Proc. IEEE Int. Conf. RFID Technol. Appl. (RFID-TA)*, Pisa, Italy, Sep. 2019, pp. 297–300.
[31] R. K. Singh, A. Michel, P. Nepa, and A. Salvatore, "Compact Quasi-Yagi reader antenna for UHF RFID smart-glove," in *Proc. 5th Int. Conf. Smart Sustain. Technol. (SpliTech)*, Split, Croatia, Sep. 2020, pp. 1–4.
[32] N. Kaneda, W. R. Deal, Y. Qian, R. Waterhouse, and T. Itoh, "A broadband planar Quasi-Yagi antenna," *IEEE Trans. Antennas Propag.*, vol. 50, no. 8, pp. 1158–1160, Aug. 2002.
[33] D. Le, L. Ukkonen, and T. Bjorninen, "A dual-ID RFID tag for headgear based on Quasi-Yagi and dipole antennas," *IEEE Antennas Wireless Propag. Lett.*, vol. 19, no. 8, pp. 1321–1325, Aug. 2020.
[34] *IT'IS Foundation, Tissue Properties*. Accessed: Apr. 5, 2021. [Online]. Available: https://www.itis.ethz.ch/virtual-population/tissue-properties/downloads
[35] F. Yang, A. Aminian, and Y. Rahmat-Samii, "A novel surface-wave antenna design using a thin periodically loaded ground plane," *Microw. Opt. Technol. Lett.*, vol. 47, no. 3, pp. 240–245, Nov. 2005.
[36] F. Yang and Y. Rahmat-Samii, "Reflection phase characterizations of the EBG ground plane for low profile wire antenna applications," *IEEE Trans. Antennas Propag.*, vol. 51, no. 10, pp. 2691–2703, Oct. 2003.
[37] *Radiofrequency Radiation Exposure Evaluation: Portable Devices*, U.S. Code of Federal Regulations 47, document CFR 2.1093, Oct. 2010.
[38] E. Moradi, S. Amendola, T. Bjorninen, L. Sydanheimo, J. M. Carmena, J. M. Rabaey, and L. Ukkonen, "Backscattering neural tags for wireless brain-machine interface systems," *IEEE Trans. Antennas Propag.*, vol. 63, no. 2, pp. 719–726, Feb. 2015.
[39] G. Marrocco, "The art of UHF RFID antenna design: Impedance-matching and size-reduction techniques," *IEEE Antennas Propag. Mag.*, vol. 50, no. 1, pp. 66–79, Feb. 2008.
[40] T. Björninen, L. Sydänheimo, and L. Ukkonen, "Development and validation of an equivalent circuit model for UHF RFID IC based on wireless tag measurements," in *Proc. Antenna Meas. Techn. Assoc. Symp.*, Bellevue, WA, USA, Oct. 2012, pp. 480–485.
[41] *NXP Semiconductors, Eindhoven, Netherlands, UCODE G2iL(+) Series ICs*. Accessed: Apr. 6, 2021. [Online]. Available: http://www.nxp.com/products/identification_and_security/smart_label_and_tag_ics/ucode/
[42] R. Bourtoutian, C. Delaveaud, and S. Toutain, "Differential antenna design and characterization," in *Proc. 3rd Eur. Conf. Antennas Propag.*, Berlin, Germany, Mar. 2009, pp. 2398–2402.
[43] D. M. Pozar, *Microwave Engineering*, 4th ed. Hoboken, NJ, USA: Wiley, 2012.
[44] S. Ahmed, A. Mehmood, L. Sydanheimo, L. Ukkonen, and T. Bjorninen, "Glove-integrated textile antenna with reduced SAR for wearable UHF RFID reader," in *Proc. IEEE Int. Conf. RFID Technol. Appl. (RFID-TA)*, Pisa, Italy, Sep. 2019.
[45] H. Lee, J. Tak, and J. Choi, "Wearable antenna integrated into military berets for indoor/outdoor positioning system," *IEEE Antennas Wireless Propag. Lett.*, vol. 16, pp. 1919–1922, 2017.
[46] A. Foroozesh and L. Shafai, "Investigation into the application of artificial magnetic conductors to bandwidth broadening, gain enhancement and beam shaping of low profile and conventional monopole antennas," *IEEE Trans. Antennas Propag.*, vol. 59, no. 1, pp. 4–20, Jan. 2011.
[47] K. Agarwal, Y.-X. Guo, and B. Salam, "Wearable AMC backed near-endfire antenna for on-body communications on latex substrate," *IEEE Trans. Compon., Packag., Manuf. Technol.*, vol. 6, no. 3, pp. 346–358, Mar. 2016.
[48] C. Occhiuzzi, S. Cippitelli, and G. Marrocco, "Modeling, design and experimentation of wearable RFID sensor tag," *IEEE Trans. Antennas Propag.*, vol. 58, no. 8, pp. 2490–2498, Aug. 2010.
[49] G. A. Casula, G. Montisci, and H. Rogier, "A wearable textile RFID tag based on an eighth-mode substrate integrated waveguide cavity," *IEEE Access*, vol. 8, pp. 11116–11123, Jan. 2020.

SHAHBAZ AHMED (Student Member, IEEE) received the B.E. degree in electronics engineering from AIR University, Islamabad, Pakistan, in 2013, and the M.Sc. degree in electrical engineering with major in electronics from Tampere University, Tampere, Finland, in 2018, where he is currently pursuing the Ph.D. degree with the Wireless Identification and Sensing Systems Research Group.

He has been a Network Support Engineer with Alcatel Lucent, Pakistan. His research interests include antenna designing, electromagnetic modeling, implantable and wearable biomedical systems, RFID systems, and low-profile antennas. He was a recipient of the Nokia Foundation Scholarship and the Finnish Foundation for Technology Promotion (Tekniikan edistämissäätiö) to support his research studies in the chosen area of interest.

DUC LE (Student Member, IEEE) received the B.S. degree (Hons.) in electrical engineering from the HCMC University of Technology and Education, Ho Chi Minh, Vietnam, in 2014, and the M.S. degree (Hons.) in electrical engineering from the Tampere University of Technology, Tampere, Finland, in 2018, where he is currently pursuing the Ph.D. degree with the Wireless Identification and Sensing Group. He was a Research Assistant with the Tampere University of Technology, from 2016 to 2018. His research interests include technology for wireless health, wearable antenna development, electromagnetic modelling, RF circuits, RFID tag, and low-profile antennas. He was a recipient of prestigious award, including the HPY Research Foundation of Elisa and the Nokia Foundation Scholarship to support research studies of telecommunications technology, studies closely related to telecommunications.

LAURI SYDÄNHEIMO (Member, IEEE) received the M.Sc. and Ph.D. degrees in electrical engineering from the Tampere University of Technology (TUT), Tampere, Finland. He is currently a Professor with the Faculty of Biomedical Sciences and Engineering, TUT. He has authored more than 200 publications in radio-frequency identification tag, reader antenna design, and wireless system performance improvement. His current research interests include wireless data communication and wireless identification and sensing.

LEENA UKKONEN (Member, IEEE) received the M.Sc. and Ph.D. degrees in electrical engineering from the Tampere University of Technology, Tampere, Finland, in 2003 and 2006, respectively. She is currently a Professor with the Faculty of Medicine and Health Technology, Tampere University, Tampere. She is leading the Wireless Identification and Sensing Systems Research Group. She has authored more than 300 scientific publications in radiofrequency identification (RFID), antenna design, and biomedical and wearable sensors. Her current research interests include RFID antennas, RFID sensors, implantable biomedical systems, and wearable antennas.

TONI BJÖRNINEN (Senior Member, IEEE) received the M.Sc. and Ph.D. degrees in electrical engineering from the Tampere University of Technology, Tampere, Finland, in 2009 and 2012, respectively.

He is currently an Academy of Finland Research Fellow with the Faculty of Medicine and Health Technology, Tampere University, Tampere. He has been a Visiting Postdoctoral Scholar with the Berkeley Wireless Research Center, UC Berkeley, and with the Microwave and Antenna Institute in Electronic Engineering Department, Tsinghua University, Beijing. He has coauthored 178 peer-reviewed scientific publications and given over 50 presentations in scientific symposia worldwide. His research interest includes microwave technology for wireless health, including implantable and wearable antennas, wireless power transfer, sensors, and RFID-inspired wireless solutions.

Dr. Björninen was a member of the editorial boards of *International Journal of Antennas and Propagation*, from 2014 to 2018, *IET Electronics Letters*, from 2016 to 2018, and IEEE Journal of Radio Frequency Identification, from 2017 to 2020. He is serving as an Associate Editor for *Applied Computational Electromagnetics Society Journal*.

PUBLICATION V

Circularly Polarized Corner-Truncated and Slotted Microstrip Patch Antenna on Textile Substrate for Wearable Passive UHF RFID Tags

Duc Le, Leena Ukkonen, Toni Björninen

European Conference on Antennas and Propagation

March 2020, doi: 10.23919/EuCAP48036.2020.9135984

Circularly Polarized Corner-Truncated and Slotted Microstrip Patch Antenna on Textile Substrate for Wearable Passive UHF RFID Tags

Duc Le, Leena Ukkonen, Toni Björninen
Faculty of Medicine and Health Technology, Tampere University, Tampere, Finland,
{vietduc.le, leena.ukkonen, toni.bjorninen}@tuni.fi

***Abstract*—We present a compact circularly polarized (CP) antenna for wearable passive UHF RFID tags. The antenna is a square-shaped microstrip patch antenna where we have applied corner truncation and slotting techniques in the top layer conductor for achieving the CP property and a shorting pin and loop structure for impedance matching. Despite using a low-permittivity textile as antenna substrate, the antenna's footprint size is only 5-by-5 cm, which is approximately 15% of the operating wavelength. At the same time, the on-body measurements, the antenna's axial ratio is 0.9 dB and the measured attainable read range (reader's EIRP = 3.28 W) of the tag reaches 4.2 meters with a CP reader antenna and ranges from 2.9 meters to 3.4 meters for a linear reader antenna, depending on the rotation angle between the antennas.**

***Index Terms*—wearable antenna, circular polarization, *RFID tag, RFID tag, UHF*.**

I. Introduction

Nowadays, the microwave and the antenna technology has been recognized as a compelling approach to achieve the versatile energy- and cost-efficient wireless platforms for body-centric applications. Such technology is at demand in several application areas including i.e. wireless health monitoring. With the assistance of wearable radio frequency identification (RFID) and RFID-inspired backscattering communications, the identification, the access control and the localization can be achieved unobtrusively.

Recently, due to great capabilities of textile-integrated passive wireless platforms, the development and manufacturing of the wearable antennas and interconnections have been an active research [1-3]. It is noted, however, that these wearable antennas are linearly polarized (LP), which may cause unreliable wireless links due to possible polarization mismatch caused by the constant human body movement in realistic scenarios. Currently, most of the passive RFID tags in the commercial domain are based on dipole antennas having linear polarization (LP). In a system with a CP reader, they can be detected with 50% polarization efficiency. The maximum efficiency of 100% could be achieved with LP reader, but there would also be a risk of cross-polarization depending on the mutual antenna rotation angle. For this reason, most RFID systems rely on CP readers despite lower polarization efficiency. Thus, the development of passive UHF RFID tags based on CP antennas has been drawing attention in the RFID research community. There are have been many research to develop this antenna form for applying to on-body wearable applications for wireless body area network (WBAN) [4-7], but overall footprint of these antennas is rather large, it may unreasonably fit to some parts of body such as head, forearm or wrist and it may suffer from significant frequency shift or unpredicted radiation pattern due to structural deformation. Previously, a small size dual-layer split ring resonator was shown to produce circular polarization [8]. However, the attainable read range of RFID tag antenna is only around 2-3 meters.

To advance upon these works, we proposed a wearable circularly polarized patch antenna for RFID tag. The novelty of the proposed antenna lies in its simplistic structure, enhanced miniaturization and higher read range (4.2 meters). Besides, since all parts of this antenna is made by flexible and bendable materials for substrate and conducting plane, this antenna is appropriate to seamlessly integrate to wearable identification and sensing applications. The motivation of developing the antenna structure is based on the compact circularly polarized square microstrip antenna introduced in [9]. For achieving the circular polarization, the antenna geometry consists mainly of two main parts, namely a corner-truncated square patch and a fully ground plane. The miniaturization is solely obtained by applying hexagonal slots in the radiating patch [10]. Since we utilize this antenna for RFID applications with inductive feeding network technique based on our previous study to attain a high-performance metal mountable tag [11].

II. Attainable Read Range of a Tag with Arbitrary Polarization

The primary performance indicator of a passive UHF RFID tag is the attainable read range (d_{tag}). It is determined by the sensitivity of the RFID integrated circuit (IC) and the efficiency of tag antenna to capture and transfer energy from the reader's carrier signal to the IC for turning it on. For a free space communication link,

$$d_{tag} = \frac{\lambda}{4\pi}\sqrt{\left\{\frac{4Re(Z_a)Re(Z_{ic})}{|Z_a+Z_{ic}|^2}\right\}\frac{\chi \cdot G \cdot EIRP}{P_{ic}}}, \quad (1)$$

where λ is the wavelength of the reader's signal, the factor in the curly brackets is the antenna-IC power transmission efficiency (τ) determined by the impedance of the tag antenna and the RFID-IC Z_a and Z_{ic} defined as $Z_{ic} = R_{ic} + jX_{ic}$ and

$Z_a = R_a + jX_a$, respectively, χ is the polarization efficiency between the tag antenna and the incident wave. *G* is the gain of the tag antenna, and *EIRP* is the equivalent isotropic radiated power of the reader and P_{ic} is the turn-on power of the tag IC [12]. The polarization efficiency $0 \leq \chi \leq 1$ in (1) is determined by the polarizations of the tag antenna and the incident wave.

The complex electric field vector (**E**) of an electromagnetic wave can be expressed as a sum of orthogonal left and right hand circularly polarized components $\mathbf{E}_L$ and $\mathbf{E}_R$, respectively, by introducing a complex scalar (γ) called circular polarization ratio such that: $\mathbf{E} = \mathbf{E}_L + \mathbf{E}_R = \mathbf{E}_L + \gamma\mathbf{E}$ [13]. With this notion, the maximum (Γ_+) and minimum (Γ_-) polarization efficiency is given by [13]

$$\Gamma_{\pm} = \frac{\left(1 \pm |\gamma_{tag}||\gamma_{inc}|\right)^2}{\left(1+|\gamma_{tag}|^2\right)\left(1+|\gamma_{inc}|^2\right)}, \tag{2}$$

where the complex scalars γ_{tag} and γ_{inc} are the circular polarization ratios of the tag antenna and the incident wave, respectively [10]. For a linearly polarized incident wave γ_{inc}=1 and thus (2) becomes

$$\Gamma_{\pm LIN} = \frac{\left(1 \pm |\gamma_{tag}|\right)^2}{2\left(1+|\gamma_{tag}|^2\right)}. \tag{3}$$

For left and right hand circularly polarized incident wave, γ_{inc}=0 and $|\gamma_{inc}| \to \infty$, respectively. In these cases, (2) reduces to

$$\Gamma_{LHC} = \frac{1}{1+|\gamma_{tag}|^2} \text{ and } \Gamma_{RHC} = \frac{1}{1+|\gamma_{tag}|^{-2}}. \tag{4}$$

Here, the polarization efficiency is independent of the rotation angle between the tag and the reader antennas due to the perfect circular polarization of the incident wave, and thus the minimum and maximum polarization efficiencies are equal. Finally, the connection between the circular polarization ratio and the axial ratio of the tag antenna is given by [13]

$$A_{tag} = \frac{1+|\gamma_{tag}|}{1-|\gamma_{tag}|} \text{ and } A_{tag} = \frac{|\gamma_{tag}|+1}{|\gamma_{tag}|-1}, \tag{5}$$

for left- and right-handed antenna polarizations, respectively. This enables alternative formulation of the above analysis using the axial ratio value, instead of the circular polarization ratio.

Overall, the formulation (1)-(5) provides the estimation of attainable read range of a tag with arbitrary polarization assuming the reader is transmitting either linearly or circularly polarized wave. In case of the linear wave polarization, (1) and (3) give the minimum and maximum read range under all possible rotations of the tag antenna with-respect-to polarization of the incident wave.

III. Tag Antenna Structure, Optimisation and Tag's Performance Evaluation

This section shows the optimized antenna model and practical implementation structure. Additionally, the description of the measurement setup and procedures are one part of this section. Lastly, the comparison of measurement and simulation outcomes will be presented.

A. Numerical Modeling

The modeling and the optimization of the CP patch RFID tag antenna was conducted in ANSYS High Frequency Structure Simulator (HFSS), which is a full-wave electromagnetic field solver based on the finite element method.

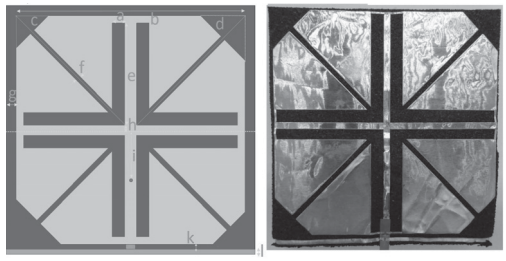

Fig. 1. The geometry and dimension of the antenna in details.

TABLE I
Value of Antenna Dimension in Millimeters

a	b	c	d	e	f	g	h	i	k	l
2.5	-7.5	7.2	5.5	21	1.5	2	1	9	1	1

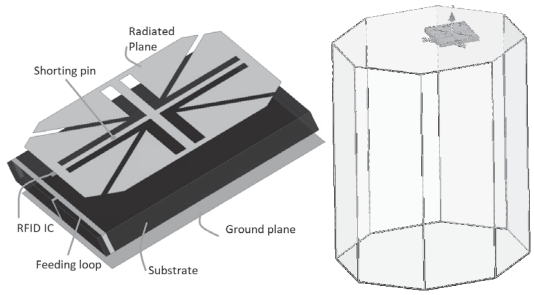

Fig. 2. Exploded view of the antenna and Polygonal cylinder model of the human body

As shown in Fig. 2, the optimized antenna dimension is maintained at 50 mm by 50 mm with 4 mm thickness (0.1525 $\lambda_0 \times 0.1525\ \lambda_0 \times 0.0091\ \lambda_0$, where λ_0 is the wavelength at the center frequency of 0.915 GHz). With that size, this RFID tag can fit in the limited dimension of almost of body parts such as head, arm, chest or foot. Due to the conducting plane is practically fabricated by flexible copper foil, some area of the surface appears to be fragile. To maximize the readable range and attainable gain of the tag, we antenna impedance is bi-conjugately matched to the impedance of the RFID IC chip (red point in Fig. 1). This is achieved by shorting the radiated plane to the ground plane using a shorting pin. The UHF RFID microchip (NXP UCODE G2iL; turn-on power −18 dBm [17]) is mounted at the feeding point. The distance between the shorting pin and the middle of the antenna is *i*=9mm. One of the novelty elements of this antenna is the four truncated corners for achieving the right-hand circularly polarization and consumes less space of the total area of

antenna. The tuned side length of these corners is c = 6 mm for the left side and d= 9mm for the right side. Four cross slots with the width a = 1.5 mm combining to 4 L-type slots (installed diagonally) for obtaining circular polarization and miniaturize the antenna. The main idea behind these L- type slots is to alter the current density on the radiated surface because it changes the effective inductance and capacitance of the antenna, hence, the size of antenna is minimized with respect to the resonance frequency [10].

The exploded view of the antenna in Fig. 2 demonstrates the number and the order of antenna layers. The first layer is the radiating patch, the total size of this plane is 46 mm by 46 mm by 40 µm. The second layer is the substrate that size is 50 mm by 50 mm by 4 mm. Considering on-body wearable applications, the flexible ethylene-propylene-diene-monomer (EPDM) rubber foam (ε_r = 1.53, σ = 0.01 S/m [14]) is used as substrate. The last layer is the ground plane, which isolates the human body to the antenna. Thus, the antenna performance is less effected by the electromagnetic properties of the human body. Furthermore, three narrow grounding strips at the edge of the substrate directly connected to the ground plane are the feeding network. In the simulation environment, we applied the simple human body as the polygonal cylinder. The cylinder material is assigned as skin (ε_r = 41.6, σ = 0.86 S/m [15]), since it is the tissue closest to the antenna and electromagnetically most lossy in nature. The antenna placement on the head model is shown in Fig. 2.

B. Experimental Characterization

All measurements were conducted with Voyantic Tagformance measurement system in an anechoic chamber with the tag under body worn conditions as indicated in Fig. 3. The measurement system contains an RFID reader with adjustable transmission frequency and output power and provides the measurement of the backscattered signal power at the receiver.

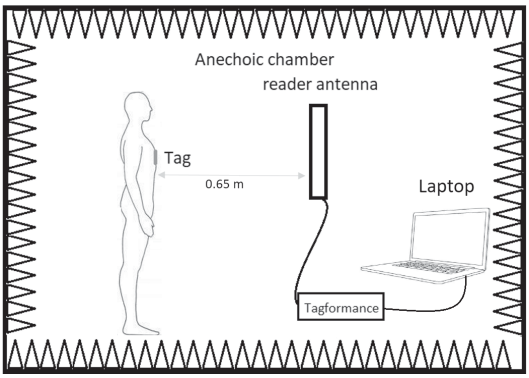

Fig. 3. The measurement setup in the anechoic chamber

In the measurement of the axial ratio of the tag, we connected a linearly polarized antenna with the reader and recorded the lowest continuous-wave transmission power (threshold power: P_{th}) at which the tag remained responsive at different rotation angles with-respect-to the reader antenna. Here we defined P_{th} as the lowest power at which valid 16-bit random number from the tag is received as a response to the *query* command in ISO 18000-6C communication standard. At each frequency, the ratio of the maximum and minimum values of P_{th} over all rotation angles, corresponds with the ratio $\Gamma_{+LIN}/\Gamma_{-LIN}$ obtained from (3). Therefore,

$$\frac{P_{th,max}}{P_{th,min}} = \frac{\Gamma_{+LIN}}{\Gamma_{-LIN}} = \frac{(1+|\gamma_{tag}|)^2}{(1-|\gamma_{tag}|)^2}. \quad (6)$$

Because the polarization of our tag antenna is right-handed, $1<|\gamma_{tag}|$ and (5)-(6) imply

$$A_{tag} = \sqrt{\frac{P_{th,max}}{P_{th,min}}} \text{ and } |\gamma_{tag}| = \frac{A_{tag}+1}{A_{tag}-1}. \quad (7)$$

For estimating the read range of the tag we used a right hand circularly polarized reader antenna. In this experiment, we first characterized the wireless channel from the reader antenna to the location of the tag under test using the measurement system's reference tag with known properties. As detailed in [16], this enables the estimation of the attainable read range of the tag under test as

$$d_{tag} = \frac{\lambda}{4\pi}\sqrt{\frac{EIRP}{\Lambda}\frac{P_{th*}}{P_{th}}}, \quad (8)$$

where P_{th} is the measured threshold power of the tag, Λ is a known constant describing the sensitivity of the system reference tag, and P_{th*} is the measured threshold power of the reference tag. Given that the reference tag is linearly polarized (dipole type antenna), we compensated the linear-to-circular antenna polarization mismatch loss included in P_{th*} by diving it with a factor of two.

In addition, we estimated the attainable read range for a linearly polarized reader antenna. To achieve this, we first computed $\Gamma_{\pm LIN}$ and Γ_{RHC} from (3) and (4) using the measured $|\gamma_{tag}|$ computed from (6). As presented in (1), d_{tag} is proportional to the square root of the polarization efficiency. Thus, first diving the measured d_{tag} from (8) with $\sqrt{\Gamma_{RHC}}$ compensates the polarization mismatch loss with the right hand circularly polarized reader antenna used in the experiment. Secondly, subsequent multiplication by $\sqrt{\Gamma_{\pm LIN}}$ scales the result to the attainable read range for a linearly polarized reader antenna.

C. Results and Discussion

For evaluating the performance of the CP RFID antenna, this part focuses on the simulation and measurement outcomes, namely the impedance, surface current density, axial ratio and attainable read range.

Fig. 4 shows the input impedance of antenna and IC along with the corresponding power transfer efficiency. The graph shows how the tag antenna parameters are carefully optimized to provide good bi-conjugate matching with the RFID IC chip at 925-932 MHz. It leads to the power transmission coefficient of the antenna that is above 80%

over the frequency band. The model of IC chip impedance value is based on the previous research [17]. The chip is modelled as a parallel connection of R = 2.85 KΩ and C = 0.91 pF [18].

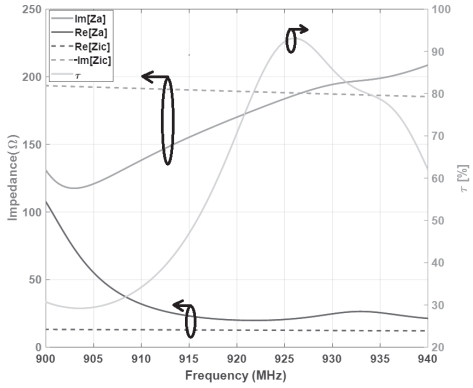

Fig. 4. Simulated IC chip and antenna impedance and power transfer efficiency.

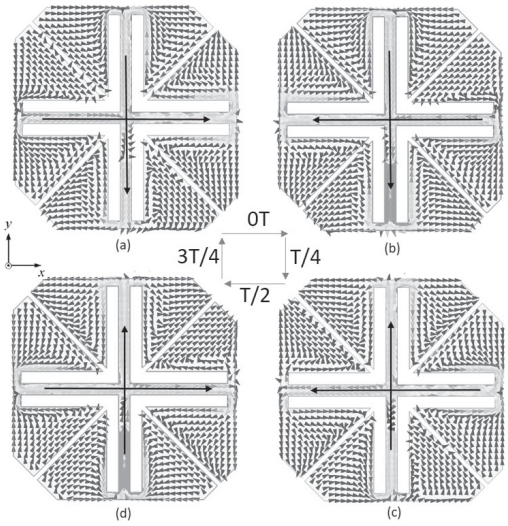

Fig. 5. Simulated surface current density at different phases of 930 MHz. (a) Phase = 10°. (b) Phase = 100°. (c) Phase =190°. (d) Phase = 280°

For the purpose of visualizing how the circular polarization is generated, the simulated surface current density on the patch at 930 MHz for four moments 0T, T/4, T/2, and 3/4T are illustrated in Fig.5. It can be seen that the current distributions at cross-section in the middle of the antenna are orthogonal and 90° phase difference to each other. With the increasement of time by a step of T/4, the current rotate counter-clockwise confirming right-hand circularly polarization (RHCP) in the boresight direction. Based on the results presented in Fig. 6, the lowest axial ratio of this antenna in simulation and measurement is at 930 MHz. The axial ratio of practical measurement results is even lower than 0.9 dB, which is nearly perfect circular polarization. The bandwidth of the below 3dB axial ratio of simulation and measured results is 0.5 MHz and 5 MHz. The different between the measured and simulated outcomes because the simulations were conducted in a simplified head model whereas the measurements were conducted on an actual person.

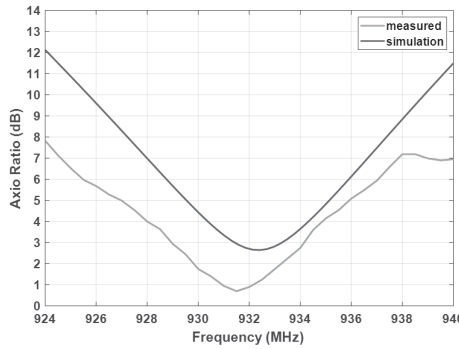

Fig. 6. The axial ratio of te RFID tag antenna

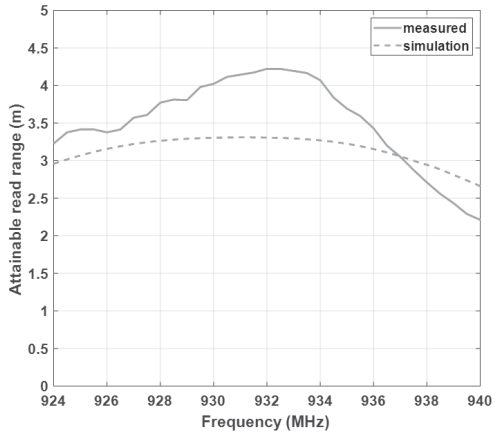

Fig. 7. The read range of CP tag when the reader antenna is circularly polarized

In addition to the above-described antenna performance parameters, an intuitive way to evaluate the performance of the RFID tag is the read range. Fig. 7 shows the attainable read range of the CP antenna tag when the reader antenna is circular polarization. Overall, the read range measurement result is approximate to those of simulation with varying from 2.5 meters to around 4 meters from 924 MHz to 940 MHz. It can be observed that both measured, and simulation read range reach the peak at 932 MHz with 4.3 meters and 3.2 meters respectively. When the reader antenna is linearly

polarization antenna, there are two results; maximum read range and minimum read range corresponding to the maximum (Γ_{+LIN}) and minimum (Γ_{-LIN}) polarization efficiency as Fig. 8. As shown, the maximum read range of the antenna is approximately 4 meters and 3 meters with measured and simulation cases respectively. The attainable read range corresponding minimum polarization efficiency varies from 0.5 meter at 924 MHz and 940 MHz and reaches ssthe peak at around 2.8 meters at 932 MHz.

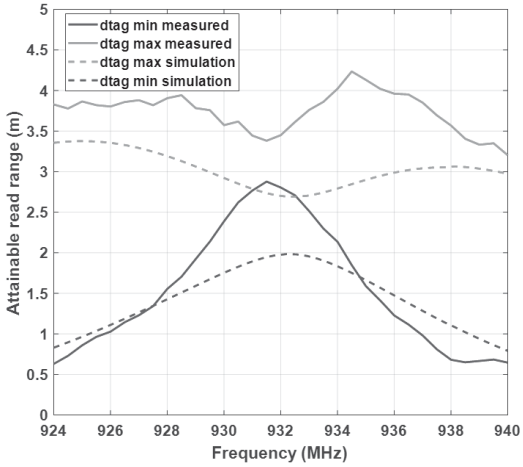

Fig. 8. The read range of the CP antenna

TABLE I. SUMARY OF ANTENNA PERFORMANCE

Frequency (MHz)	*Gain (dB)*	*Directivity (dBi)*	*Radiation efficiency (%)*
900	-9.3	3	3.2
915	-9.5	4	3.2
925	-9	3	3.1
932	-9.2	3.15	4

Table I demonstrates the gain, directivity and radiation efficiency of the antenna. The gain of the antenna is around -9.1 dB. The maximum directivity of this antenna is D = 4 dBi at 915 MHz and the radiation efficiency is e_r= 4 % at 932 MHz.

IV. CONCLUSION

Wearable antennas are core technology for modern wireless body-area systems that enable important applications for instance in the healthcare and medicine. We have presented a small-sized circularly polarized antenna that maintains low axial ratio value in body-worn configuration. Moreover, we have shown that the antenna can be self-matched to an RFID integrated circuit that exhibits a low-resistance and capacitive impedance, like typical energy harvesting systems. The measured read range of the RFID tag is 4.2 meters with a CP reader antenna and ranges from 2.9 meters to 3.4 meters for a linear reader antenna. Thus, the antenna is suitable for RFID systems with either type of reader antennas. Finally, as the antenna comprises a textile substrate, it benefit the wearable applications.

REFERENCES

[1] T. Björninen and F. Yang, "Low-profile head-worn antenna with a monopole-like radiation pattern," IEEE Antennas Wireless Propag. Lett., vol. 15, pp. 794-797, 2016.

[2] X. Chen, L. Aruhan, W. Zhigang, L. Ukkonen, and J. Virkki, "Experimental study on strain reliability of embroidered passive UHF RFID textile tag antennas and interconnections," Journal of Engineering, 2017.

[3] H. Lee, S. Kim, D. De Donno, and M. M. Tentzeris, "A novel "universal" inkjet-printed EBG-backed flexible RFID for rugged on-body and metal mounted applications," In IEEE/MTT-S International Microwave Symposium Digest, pp. 1-3, 2012.

[4] H. D. Chen, C. H. Tsai, C. Y. Kuo, "Circularly polarized loop tag antenna for long reading range RFID applications," in IEEE Antennas and Wireless Propagation Letters, 2013, pp. 1460-1463.

[5] E. K. Kaivanto, M. Berg, E. Salonen, P. De Maagt, "Wearable circularly polarized antenna for personal satellite communication and navigation," in IEEE Trans. Antennas Propag., vol. 59, no. 12, pp. 4490-4496, 2011.

[6] M. S. Shakhirulel at.. , "1.575 GHz circular polarization wearable antenna with three different substrate materials," In 2014 IEEE Asia-Pacific Conference on Applied Electromagnetics (APACE), pp. 43-46, 2014.

[7] Y. Kuang, S. Ma, L. Ukkonen, J. Virkki, T. Björninen, "Circularly polarized textile tag antenna for wearable passive uhf rfid systems," In 2018 International Applied Computational Electromagnetics Society Symposium-China (ACES), pp. 1-2, 2018.

[8] S. Ma, L. Ukkonen, , L. Sydänheimo, T. Björninen, "Dual-Layer circularly polarized split ring resonator inspired antenna for wearable uhf rfid tag," In 2018 IEEE International Symposium on Antennas and Propagation & USNC/URSI National Radio Science Meeting, pp. 683-684, 2018.

[9] W.S. Chen, C.K. Wu, and K.L. Wong, "Novel compact circularly polarized square microstrip antenna," IEEE Trans. Antennas Propag., vol. 49, no. 3, pp. 340–342, Mar. 2001.

[10] T. Ali, R. C. Biradar, "A compact hexagonal slot dual band frequency reconfigurable antenna for WLAN applications," in Microwave and Optical Technology Letters, vol. 59, no. 4, pp. 958-964, 2017.

[11] T. Björninen, K. E. Delzo, L. Ukkonen, A. Z. Elsherbeni, and L. Sydänheimo, "Long range metal mountable tag antenna for passive UHF RFID systems," in 2011 IEEE International Conference on RFID Technologies and Applications, 15–16 Sep. 2011, Sitges, Spain, pp. 202–206.

[12] P. V. Nikitin, "Antennas and propagation in UHF RFID systems," in Proc. IEEE International Conference on RFID, 16-17 Apr. 2008, Las Vegas, NV, USA, pp. 277-288.

[13] Thomas A. Milligan, Modern Antenna Design, 2nd ed., vol. 2. John-Wiley & Sons, Inc., pp. 18-24.

[14] D. Le, Y. Kuang, L. Ukkonen, and T. Björninen, "Microstrip transmission line model fitting approach for characterization of textile materials as dielectrics and conductors for wearable electronics", Intl. J. Numerical Modelling Electronic Netw. Dev. Fields, 2019.

[15] IT'IS Foundation, Tissue Properties [Online accessed: Sep. 20, 2019]. Available: https://www.itis.ethz.ch/virtual-population/tissue-properties/downloads.

[16] J. Virkki, T. Björninen, S. Merilampi, L. Sydänheimo, L. Ukkonen, "The effects of recurrent stretching on the performance of electro-textile and screen-printed ultra-high-frequency radio-frequency identification tags," Text. Res. J., vol. 85, no. 3, pp. 294-301, Feb. 2015.

[17] T. Björninen, M. Lauri, L. Ukkonen, R. Ritala, A. Z. Elsherbeni, L. Sydänheimo, "Wireless measurement of RFID IC impedance," IEEE Transactions on Instrumentation and Measurement, vol. 60, no. 9, pp. 3194-3206, 2011.

[18] NXP Semiconductors, "UCODE G2iL and G2iL+", 2019.

PUBLICATION VI

A Small All-Corners-Truncated Circularly Polarized Microstrip Patch Antenna on Textile Substrate for Wearable Passive UHF RFID Tags

Duc Le, Leena Ukkonen, Toni Björninen

IEEE Journal of Radio Frequency Identification

April 2021, doi: 10.1109/JRFID.2021.3073457

A Small All-Corners-Truncated Circularly Polarized Microstrip Patch Antenna on Textile Substrate for Wearable Passive UHF RFID Tags

Duc Le, *Student Member, IEEE*, Shahbaz Ahmed, *Student Member, IEEE*, Leena Ukkonen, *Member, IEEE*, Toni Björninen, *Senior Member, IEEE*

***Abstract*—We present a wearable passive UHF RFID tag based on a circularly polarized (CP) patch antenna on a textile substrate. The antenna miniaturization is based on applying a combination of the cross- and L-shaped slots in the radiator. In conjunction, the right-hand circular polarization is achieved by asymmetrically truncating all four corners of the square-shaped radiator. Despite using a regular low-permittivity textile as the antenna substrate, we downsized the antenna to a 5 cm × 5 cm footprint with the thickness of 4 mm, which is equal to 0.1525λ × 0.1525λ × 0.0091λ, where λ is the free space wavelength at 915 MHz. In the numerical modeling and optimization of the antenna, we used a simplified cuboid-shaped and anatomical human body models. In addition to simulated conventional antenna performance indicators, we introduce spatial coverage as a new parameter for assessing the detection reliability of UHF RFID tags. Finally, we measured a manufactured tag worn in four different configurations on the body. The measured axial ratio value was approximately 2 dB in all cases and the tag provided a high attainable read range of around 5.8 meters for a right-hand CP reader emitting 3.28 W EIRP.**

***Index Terms*—*W*earable antenna, circular polarization, p*assive UHF RFID tag, wearable RFID tag*, wireless body-area systems.**

I. Introduction

Microwave and antenna technology has become widely applied in wireless body area systems [1-4]. Here the versatile and energy- and cost-efficient passive ultra-high frequency (UHF) radio-frequency identification (RFID) technology and RFID-inspired backscattering communications and sensing systems have been recognized as a compelling approach. The relevant applications range from identification, access control, and localization to wireless health, including wearable and implantable devices [5-7]. The two fundamental challenges related to wearable antennas are the mitigation of the negative impact arising from the electromagnetic (EM) interaction between the antenna and the dissipative biological tissue and applying textile materials and compatible manufacturing methods to achieve practical cloth-integration of antennas.

In the most of the commercial domain UHF RFID systems deployed for item-level tracking, tags comprise miniaturized dipole antennas, which are inherently linearly polarized [8], but single-layer CP tag antennas have also been studied [9][10][11][12]. However, due to the well-known miniaturization methods available for the dipole antennas and the cost-efficient mass production of the single-layer label-type dipole tags [13][14], they remain the most common type of antennas for UHF RFID tags. Under this paradigm, the reader antennas are normally CP for avoiding the chance of cross-polarization [8] with linearly polarized tags. In contrast, in wireless body area systems where the unavoidable antenna-body EM coupling limits the performance and robustness of single-layer antennas [15][16], structures including a ground plane or other types of decoupling metallic structures are preferred. This approach has been used to create well-performing textile-based 50-Ω-matched wearable CP antennas at mid- and high-UHF frequencies, e.g. GPS and 2.4 GHz ISM band applications [17][18][19]. Recently, also the development of wearable CP antennas for UHF RFID tags operating in the lower UHF band (866/915 MHz) has been gaining attention [20][21]. This provides a new alternative for the wireless body-area UHF RFID systems by improving the polarization efficiency and thereby the tag's peak read range and detection reliability.

In our previous work [21], we studied a CP microstrip patch antenna for a wearable passive UHF RFID tag attached to the upper back of a person. In this article, we report a new wearable CP patch antenna for wearable tags along with numerous other advancements, including more accurate numerical models, a more accurate measurement technique and a practical evaluation of the robustness of the tag's performance when placed at various locations on body.

For the numerical modeling, we have used realistically sized simplified cuboid-shaped and anatomical human body models. Regarding the antenna structure, by truncating all four corners of the radiating patch asymmetrically, in contrast to two in [21], allowed us to completely remove the inductive matching loop

Manuscript received January 14, 2021; revised March 17, 2021; accepted April 6, 2021. Date of publication April 24, 2021; date of current version April 24, 2021. The work of D. Le and T. Björninen was funded by Academy of Finland (funding decisions 294616 and 327789). Additionally, Duc Le was supported by Nokia Foundation.

D. Le, S. Ahmed, L. Ukkonen and T. Björninen are with Faculty of Medicine and Health Technology, Tampere University, Tampere, Finland. (e-mail: toni.bjorninen@tuni.fi).

structure from the antenna and avoid the narrow traces included in the radiating patch in [21]. This maximized the size of the radiating patch without increasing the size of the antenna for enhanced EM performance and improved the tag's structural durability. In the numerical analysis, we introduce spatial coverage as a new parameter for assessing the detection reliability of UHF RFID tags. For the wireless testing of the fully assembled prototype tag, we have formulated and implemented a new improved approach to measuring the tag antenna's axial ratio and the attainable read range of the tag for a CP reader antenna. Finally, as a crucial practical aspect, we studied the robustness of the tag by measuring it at various locations on the body and with different clothing thickness to prove its applicability for wearable systems.

II. Tag Antenna Structure, Numerical Modeling, and Performance Evaluation

A. Numerical Modeling

We used ANSYS High-Frequency Structure Simulator (HFSS) with a full-wave electromagnetic field solver based on the finite element method in modeling and optimization of the antenna. The optimization target was to obtain the frequency of the minimum axial ratio and peak read range at 915 MHz by tuning the L-slots' length and the truncation of the four corners of the radiating patch. Fig. 1 demonstrates the geometry of the antenna in detail with side and front views. As shown in Fig. 1, the UHF RFID microchip (NXP UCODE G2iL; turn-on power −18 dBm) was attached on the vertical wall of the substrate. In the numerical modeling, we used the parallel connection of the resistance R = 2850 Ω and capacitance C = 0.91 pF as an equivalent circuit giving the frequency-dependent impedance for the microchip [22]. At 915 MHz the impedance is 12.8−*j*191 Ω. The total size of the antenna is 5 cm × 5 cm with the thickness of 4 mm, which is equal to 0.1525λ × 0.1525λ × 0.0091λ, where λ is the free space wavelength at 915 MHz. With this small size, the antenna can be readily worn on various parts of the body, for instance, arm, thigh, and back. As compared with [20], in this work, we totally removed the inductive matching loop from the antenna to increase space for the signal plane and simplify the fabrication process. The four truncated corners (parameters *i*, *k*, *g* and *h* in Fig. 1) and the spacing between the L-shaped slots (parameter *x* in Fig. 1) played the key role in optimizing the axial ratio at 915 MHz.

The miniaturization of the antenna was achieved by combining the cross slots cutting the radiating patch diagonally and the four L-shaped slots; a technique proposed in [23] for a 50-Ω-matched two-corners truncated patch on a high-permittivity microwave laminate as the substrate and superstrate. The slots modify the distribution of the surface current density on the radiating patch in a strategic way, such that the resonance frequency of the antenna is considerably lowered while the radiation efficiency is reduced proportionally much less [23]. Our antenna does not include a superstrate and the substrate material we used was low-permittivity ethylene propylene diene monomer (EPDM) foam (ε_r = 1.53, tanδ = 0.02 at 915 MHz [24]), which was sandwiched between the ground plane and radiating patch. The conductors are made of 40-μm copper foil (conductivity: 58 MS/m). Following the antenna self-matching principle commonly applied in RFID tag antennas to avoid lumped component matching circuits between the antenna and the microchip, we adjusted the distance between the middle of the antenna and the shorting pin (parameter *e* in Fig. 1).

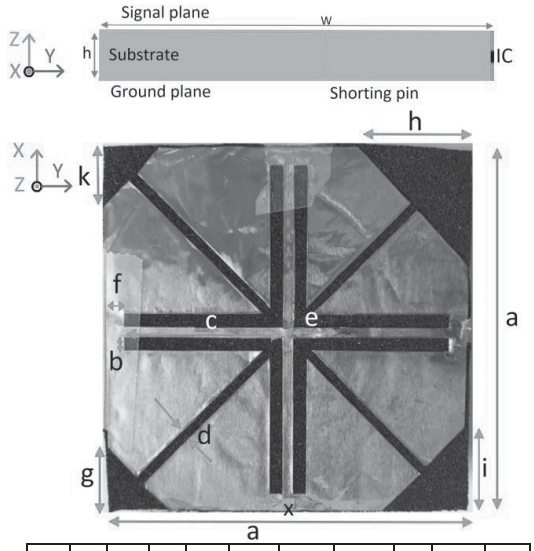

a	*b*	*c*	*d*	*e*	*f*	*g*	*h*	*i*	*k*	*x*
50	2	21	2	7	2.5	11.8	15.8	5	8.9	2.6

Fig. 1. The side view of the tag (top) and the top view (bottom) with the geometrical parameters reported in millimeters.

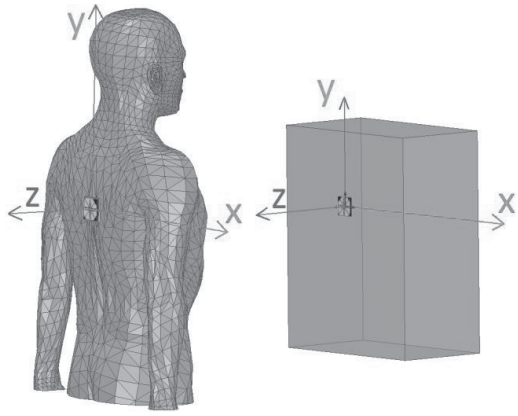

Fig. 2. The anatomical model (left side) and the cuboid model (right side).

To account for the impact of the person wearing the tag on the electromagnetic properties of the antenna, we modelled the antenna on two different body models in our numerical simulations: a simplified cuboid-shape and an anatomical model of an adult male as shown in Fig. 2. The simplified model, originating from [16], has the dimensions of 480 mm ×

59.5 mm × 44.5 mm and the dielectric properties of skin (ε_r = 41.6, σ = 0.86 S/m at 915 MHz [26]). The four-term Cole-Cole dielectric relaxation model [25] with the model parameters available from the IT'IS online library [26] was used to model the frequency-dependent dielectric properties of the skin. The skin was selected as the filling material of both models since it is the closest human tissue type to the antenna and its dielectric properties are representative to the whole body. As reported in [16], the inclusion of the internal structures in the anatomical model with their respective dielectric properties, yielded little difference in comparison with a model having homogenous skin filling when modeling a wearable antenna for off-body communications operating at 915 MHz. The antenna optimization was conducted using the cuboid model, because it provided the reduction in the simulation time and mesh size by the factors of 0.77 and 0.7, compared with the anatomical model, respectively. The optimization outcome was finally verified in the anatomical model.

The attainable read range (d_{tag}) of the tag is the primary performance indicator for passive UHF RFID tags. It depends on the properties of the tag and reader antennas, the RFID microchip, and the governing emission regulations. For a free space wireless link [8][13]

$$d_{tag} = \frac{\lambda}{4\pi}\sqrt{\frac{\tau \cdot \Gamma \cdot G \cdot EIRP}{P_{ic}}}\ ,\ \tau = \frac{4Re(Z_a)Re(Z_{ic})}{|Z_a+Z_{ic}|^2}, \quad (1)$$

where λ is the wavelength of the reader's signal, τ is the antenna-IC power transfer efficiency determined by the impedance of the tag antenna (Z_a) and the RFID microchip (Z_{ic}), Γ is the polarization efficiency between the tag antenna and the incident wave, G is the gain of the tag antenna, $EIRP$ is the equivalent isotropic radiated power of the reader and P_{ic} is the turn-on power of the RFID microchip. The polarization efficiency $0 \le \Gamma \le 1$ in (1) is determined by the polarization properties of the tag antenna and the incident wave sent by the reader. The explicit relationship between Γ, axial ratio and the circular polarization ratio are given in Section II.B.

For further assessment, we define the read range coverage C_α with $0<\alpha<1$, so that in $\alpha\cdot100\%$ of the spatial observation angles $C_\alpha < d_{tag}(\theta,\phi)$. This means that when an incident wave from the reader at an unspecified location impinges the tag, there is an $\alpha\cdot100\%$ probability for detecting the tag at a distance longer than C_α. This parameter enables the assessment of the tag's detection reliability in addition to the conventional antenna parameters and the attainable read range. Because we have considered the upper back as the nominal location for the wearable tag, in the further analysis of the spatial coverage, we assume that the reader may be located anywhere behind the person with an equal probability. Thus, we limit the analysis to the spatial directions of a spherical coordinate system centered at the origin in Fig. 2, where $-90° \le \theta \le 90°$ (elevation angle; θ=0 at z-axis) and $0° \le \phi \le 180°$ (azimuth angle; ϕ=0 at x-axis). For computing C_α, we used the step one degree in formation of the angular grid over the given intervals for θ and ϕ.

B. Experimental Characterization

We patterned the metallic parts of the antenna from copper foil using Summa Cut D60R vinyl plotter and adhered them on the substrate. The RFID microchip was mounted by the manufacturer on a 3 mm × 3 mm copper fixture patterned on plastic film, which we soldered to the antenna. All the measurements were conducted in an anechoic chamber using Voyantic Tagformance Pro measurement system [28]. For the characterization of fully assembled UHF RFID tags, the system enables the recording of the lowest continuous-wave output power (threshold power: P_{th}) of the reader for which the tag under test backscatters a valid 16-bit random number as a response to the reader's query command in ISO 18000-6C communication standard. The attainable read range of the tag, which includes the impact of polarization mismatch between the tag under test and the reader antenna, is estimated from the measured threshold power as

$$d_{tag} = \frac{\lambda}{4\pi}\sqrt{\frac{EIRP}{\Lambda}\frac{P_{th*}}{P_{th}}}, \quad (2)$$

where P_{th} is the measured threshold power of the tag, Λ is a known constant describing the system reference tag's sensitivity, and P_{th*} is the reference tag's measured threshold power [20]. All the read range results we report in Section IV are measured from the direction z-axis in Fig. 2.

For the assessment of the circular polarization property of the tag, we aligned a linear reader antenna on the z-axis of Fig. 2 with its main beam pointing towards the tag and rotated the reader antenna 360° about the z-axis with a step of 10°. Importantly, by rotating the reader antenna instead of the tag on body during the testing, we capture accurately the axial ratio of the tag while considering the whole body as the antenna platform. In contrast, in [20] we rotated the tag, which may have yielded less accurate results. From the rotation measurement, we extracted the maximum and minimum attainable read ranges $d_{tag,max}$ and $d_{tag,min}$, respectively, over the all the rotation angles. They corresponded with the maximum and minimum polarization efficiencies Γ_{+LIN} and Γ_{-LIN} between the tag antenna and the linear reader antenna, given by

$$\Gamma_{\pm LIN} = \frac{(1\pm|\gamma_{tag}|)^2}{2\left(1+|\gamma_{tag}|^2\right)}, \quad (3)$$

where γ_{tag} is the circular polarization ratio of the tag antenna [27]. Because d_{tag} is proportional to the square root of the power received by the tag, we have

$$\frac{\Gamma_{+LIN}}{\Gamma_{-LIN}} = \left(\frac{d_{tag,max}}{d_{tag,min}}\right)^2 = \left(\frac{1+|\gamma_{tag}|}{1-|\gamma_{tag}|}\right)^2, \quad (4)$$

where the last equality follows from equation (3). Because the polarization of our antenna is right-handed (reasoning for this is provided in Section IV), we solve $|\gamma_{tag}|$ from equation (4) under the assumption $|\gamma_{tag}| > 1$, and compute the axial ratio and polarization efficiency between the tag and an RHCP reader as

$$A_{tag} = \frac{|\gamma_{tag}|+1}{|\gamma_{tag}|-1} \quad \text{and} \quad \Gamma_{RHC} = \frac{1}{1+|\gamma_{tag}|^{-2}}, \quad (5)$$

respectively [21][27]. With this information, we can estimate the attainable read range of the tag referred to an ideal RHCP reader antenna as

$$d_{tag,RHC} = d_{tag,max}\sqrt{\frac{\Gamma_{RHC}}{\Gamma_{+LIN}}} = d_{tag,min}\sqrt{\frac{\Gamma_{RHC}}{\Gamma_{-LIN}}}, \quad (6)$$

where $\Gamma_{\pm LIN}$ are computed from equation (3).

C. Results and Discussion

As shown in Fig. 3 the highest power transfer efficiency of 98%

between the antenna and the IC occurs at 912 MHz and good complex conjugate matching ($\tau \geq 90\%$) is achieved over the frequency range of 908…924 MHz. In terms of the impedance matching, there is little difference between the predictions from the two different simulation models. From the cuboid model, the cuboid and anatomical models, respectively. However, the peak directivity over all spatial angles occurs approximately at $\theta = 20°$ and $\theta = 15°$ in the xz-plane in the cuboid and anatomical models, respectively with the corresponding peak values of 6.7 dBi and 5.4 dBi. The slight offset between the directivity in the direction of z-axis (boresight directivity) and the peak directivity originates from the asymmetrically truncated corners of the radiating patch.

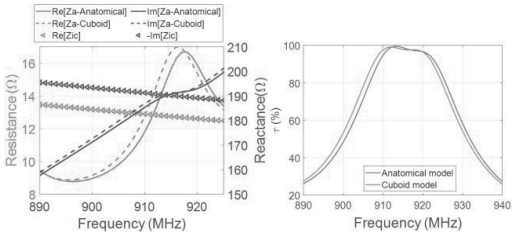

Fig. 3. Simulated antenna impedance and the IC chip impedance (left) and the antenna-IC power transfer efficiency (right).

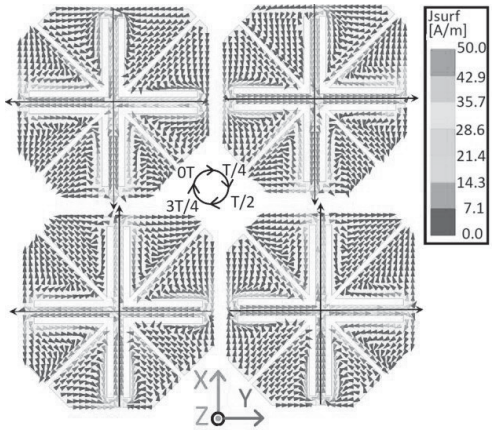

Fig. 4. Simulated surface current density from the cuboid model at different phases of 915 MHz. (a) Phase = 0°. (b) Phase = 90°. (c) Phase =180°. (d) Phase = 270°.

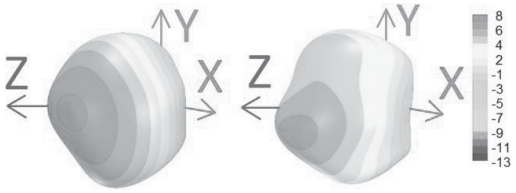

Fig. 5. Simulated 3D RHCP directivity pattern of the antenna from the cuboid model (left) and anatomical model (right) at 915 MHz.

the surface current density distribution of the antenna at the feeding phases of 0°, 90°, 180°, and 270° at 915 MHz is depicted in Fig. 4. The frequency coincides with the lowest axial ratio value. As can be seen, the current vectors at the cross-section in the middle of the antenna are orthogonal, rotating counterclockwise, which indicates right-hand circular polarization in the direction of z-axis [27]. Figure 5 shows the 3D RHCP directivity pattern of the antenna from the two models at 915 MHz. The directivity is high in the direction of z-axis, as desired, with the values of 5.5 dBi and 4.7 dBi from

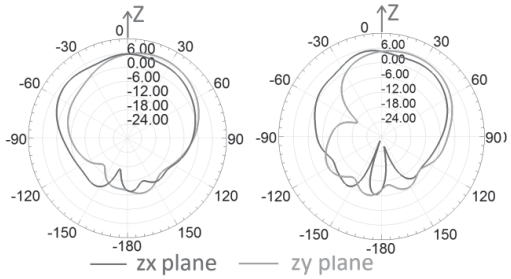

Fig. 6. Simulated (simple model) 2D RHCP directivity with cuboid model (left) and anatomical model (right) at 915 MHz. yz-plane where θ = 0° is at z-axis and swept around the yz-plane and xz-plane is plane where θ = 0° at z-axis and swept around the xz-plane.

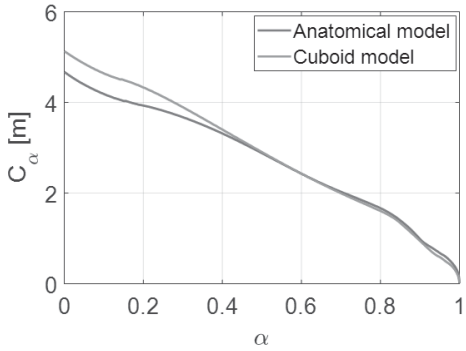

Fig. 7. Spatial coverage of the tag at 915 MHz in the region where θ = −90°…90° and ϕ = 0°…180°.

Overall, the 3D RHCP directivity demonstrates wide angular span. In terms of the 2D pattern cuts shown in Fig. 6, the simulated 3 dB beam width of the antenna from the cuboid model is approximately 76° and 118° in xz- and yz-plane, respectively. In comparison, the anatomical model provides the corresponding values of 78° and 81° xz- and yz-plane. The simulated radiation efficiency of the antenna is approximately 4.2% from both models. Overall, the prediction difference between the two models is small in terms of both impedance matching and radiation characteristics.

As shown in Fig. 7, the read range coverage obtained from both models is highly similar especially for $\alpha \geq 0.4$. This confirms that both models predict similar radiation properties at the considered observation angles. However, the peak read range which coincides with $\alpha = 0$, is slightly higher from the cuboid model. For $\alpha \geq 0.5$, both models provide nearly equal spatial coverage and from the value at $\alpha = 0.5$, we conclude that there is 50% probability that the tag can be detected from a

distance longer than 2.3 meters with an RHCP reader. This demonstrates good reliability for tag detection in practical scenarios where the alignment between the person and the reader normally varies with the movement of a person wearing the tag.

Finally, to provide further guidelines for tuning the antenna, we conducted the parametric analysis for the shorting pin position (parameter *e* in Fig. 1) and the spacing of the L-slots (parameter *x* in Fig. 1). While sweeping a particular dimensional parameter, we kept all the other ones fixed to the nominal values listed in Fig. 1. The results are shown in Fig. 8 and Fig. 9. As seen from Fig. 8, as *x* increases by 0.4 mm, the optimum axial ratio frequency increases by 37 MHz. At the same time, the frequency of the maximum attainable read range increases. In contrast, Fig. 9 shows that as the parameter *e* varies, the axial ratio remains approximately constant whereas notable level-shifts in the attainable read range emerge through the modification of the antenna impedance. Thus, the parameters *x* and *e* can be used as approximately independent parameters in the post-manufacturing tuning of the antenna to counter the impact of possible modeling uncertainty in the antenna development. As discussed below, we utilized this approach in our experiments.

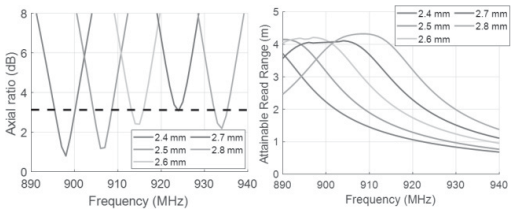

Fig. 8. Simulated (cuboid model) axial ratio and read range of the CP patch tag with various values of the spacing between L-slots (parameter

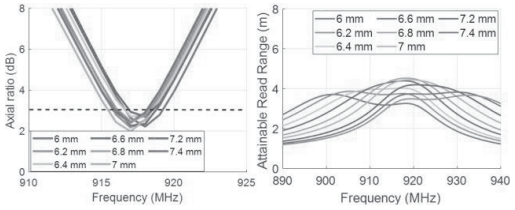

Fig. 9. Simulated (cuboid model) axial ratio and read range of the CP patch tag with various values of the shorting pin position (parameter *e* in Fig. 1).

In the experimental characterizations, we attached the tag at various locations on the body on a T-shirt and at the nominal location at the upper back also on a winter coat. As seen from the results in Fig. 10, in the measurement of the initial sample shows a downwards shift in frequency compared with the simulations. We expect this to originate primarily from the approximations involved in the simulation models. Therefore, we applied the post-manufacturing tuning to bring the axial ratio minimum frequency closer to the targeted 915 MHz. This was achieved by changing the spacing of the L-slots from x = 2.6 mm to x = 3 mm. The tuned sample provided the axial ratio value of 2.1 dB at 917 MHz when it was worn at the nominal location in the upper back. Among all the tested locations, the maximum frequency-shift in the axial ratio was only 5 MHz and, in all cases, the minimum frequency remained within the UHF RFID band (902…928 MHz). Moreover, in all cases the minimum value of the axial ratio was approximately 2 dB.

The numerically predicted and measured attainable read range of the tag is shown in Fig. 11. From the simulations, the peak read range is between 4.5 m and 5.1 m and from the direction z-axis (see Fig. 2) between 4 m and 4.5 m. The measured value from the direction of z-axis was 5.8 meters when the tag was attached to the upper back of a person on a T-shirt and it ranged between 5.5 m and 6 meters in the four different body-worn configurations. This verifies that even though the upper back was considered the nominal location of the tag when the antenna was optimized using the numerical body models, in practice, it maintains stable performance at various other locations on body. This is of major importance for practical applications.

When the reader antenna is linearly polarized, the attainable read range varies depending on the mutual rotation angle between the reader and the tag antennas. In this case, we can characterize the tag in terms of its minimum and maximum d_{tag}

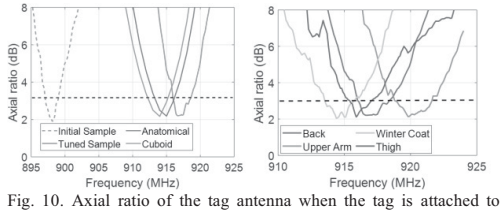

Fig. 10. Axial ratio of the tag antenna when the tag is attached to person's back (left) and at different parts of the body (right). The figure on the right contains only measured results.

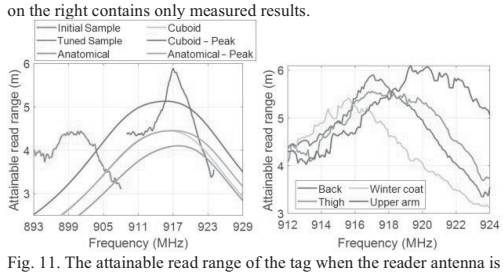

Fig. 11. The attainable read range of the tag when the reader antenna is RHCP and the tag is attached to person's back (left) and at different parts of the body (right). The figure on the right contains only measured results.

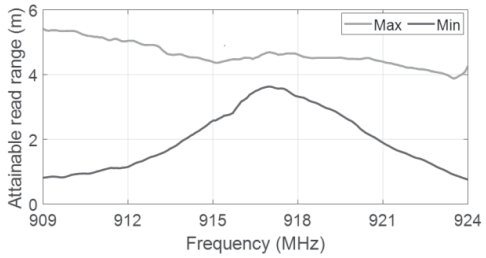

Fig. 12. The measured attainable read range of the tag (tuned sample) when it is attached to a person's back and the reader antenna is linearly polarized.

at each frequency, corresponding with the minimum (Γ_{-LIN}) and maximum (Γ_{+LIN}) polarization efficiency. As shown in Fig. 12, in this case d_{tag} varies between 3.8 m and to 4.5 m at the axial ratio minimum frequency, depending on the antennas' mutual rotation angle. This means that despite being circularly polarized, the tag can yet be detected at reasonable distance in an RFID system where linearly polarized reader antennas were deployed.

Finally, our proposed tag is compared with previous works on circularly polarized passive UHF RFID tags in Table I. As can be seen, the tag antenna gain, and the tag read range from research [30] and [32] is notably high in comparison with other works. However, also the size of the tag in these works is large, making it only wearable at the front or back of the torso. The circular footprint of the tag from research [31] is comparable with our proposed tag, but as a single-layered antenna without a ground plane, its performance is limited by the antenna-body coupling. Overall, compared with the previous works, our tag strikes a favorable balance between the size and performance and is small enough to be worn at various locations on body.

TABLE I.
COMPARISON WITH THE CONTEMPORARY RESEARCH WORK.

Ref.	Antenna type	3-dB AR BW (MHz)	Read range (m)	Gain (dBi)	Antenna size (mm)
[29]	Patch	6	2.8	−7	70 × 70 × 1.6
[20]	Dipole on AMC	40	15.7	5	215 × 215 × 6
[31]	Split ring	23	2	−9.6	$\pi \times 22^2 \times 3$
[32]	Patch	6	8.5	N/A	149.5 × 148 × 5
This work	Patch	3	5.8	−7.1	50 × 50 × 4.5

III. CONCLUSION

Wearable antennas are the core technology for modern wireless body-area systems that enable important future applications. We presented a circularly polarized antenna for wearable passive UHF RFID tags. It features a low axial ratio value in various body-worn configurations and has a small size of 5-by-5 cm on a low-permittivity textile substrate that enables seamless cloth-integration. Simultaneously with the CP radiation, the antenna geometry provides good complex conjugate impedance matching between the antenna and an RFID integrated circuit that exhibits low-resistance and capacitive impedance similar with many RF energy harvesting systems. Numerical simulations showed that the wearable tag antenna provides a broad radiation beam with the peak directivity of over 5 dBi which enables good detection reliability of the tag also when the user is not perfectly aligned with the reader. The peak of measured attainable read range of the implemented tag was 5.8 meters with an RHCP reader antenna and ranged between 3.8 m and 4.5 m for a linearly polarized reader antenna.

REFERENCES

[1] P. Van Daele, I. Moerman, and P. Demeester, "Wireless body area networks: status and opportunities," in *URSI General Assembly and Scientific Symposium*, Beijing, China, Aug. 2014, 4 pages.

[2] Y.-L. Zheng, X.-R. Ding, C. C. Y. Poon, B. P. L. Lo, H. Zhang, X.-L. Zhou, G.-Z. Yang, N. Zhao, and Y.-T. Zhang, "Unobtrusive sensing and wearable devices for health informatics," *IEEE Trans. Biomed. Eng.*, vol. 61, no. 5, pp. 1538–1554, May 2014.

[3] S. Movassaghi, M. Abolhasan, J. Lipman, D. Smith, and A. Jamalipour, "Wireless body area networks: a survey," *IEEE Commun. Surveys Tuts.*, vol. 16, no. 3, pp. 1658–1686, Jan. 2014.

[4] A. Sani, M. Rajab, R. Forster, and Y. Hao, "Antennas and propagation of implanted RFIDs for pervasive healthcare applications," *Proc. IEEE*, vol. 98, no. 9, pp. 1648–1655, Sep. 2010.

[5] J. Grosinger, "Feasibility of backscatter RFID system on the human body," *EURASIP J. Embedded Syst.*, vol. 2013, no. 2, 10 pages, Mar. 2013.

[6] W. Mongan, E. Anday, G. Dion, A. Fontecchio, K. Joyce, T. Kurzweg, Y. Liu, O. Montgomery, I. Rasheed, C. Sahin, S. Vora, and K. Dandekar, "A multi-disciplinary framework for continuous biomedical monitoring using low-power passive RFID-based wireless wearable sensors," in *IEEE International Conference on Smart Computing*, St. Louis, MO, USA, May 2016, 6 pages.

[7] S. Milici, S. Amendola, and A. Bianco, "Epidermal RFID passive sensor for body temperature measurements," in *IEEE RFID technology and applications conference (RFID-TA)*, Tampere, Finland, Sep. 2014, pp. 140–144.

[8] P. V. Nikitin, "Antennas and propagation in UHF RFID systems," in *IEEE International Conference on RFID*, Las Vegas, NV, USA, Apr. 2008, pp. 277–288.

[9] H. H. Tran, S. X. Ta, and I. Park, "A compact circularly polarized crossed-dipole antenna for an RFID tag," *IEEE Antennas Wireless Propag. Lett.*, vol. 14, pp. 674–677, Dec. 2010.

[10] H. D. Chen , C. H. Tsai, and C. Y. Kuo, "Circularly polarized loop tag antenna for long reading range RFID applications," *IEEE Antennas Wireless Propag. Lett.*, vol. 12, pp. 1460–1463, Nov. 2013.

[11] J. H. Lu and B. S. Chang, "Planar compact square-ring tag antenna with circular polarization for UHF RFID applications," *IEEE Trans. Antennas Propag.*, vol. 65, no. 2, pp. 432–441, Nov. 2016.

[12] A. S. M. Sayem, D. Le, R. B. V. B. Simorangir, T. Björninen, K. P. Esselle, R. M. Hasmi, and M. Zhadobov, "Optically transparent flexible robust circularly polarized antenna for UHF RFID tags," *IEEE Antennas Wireless Propag. Lett.*, vol. 19, no. 12, pp. 2334–2338.

[13] G. Marrocco, "The art of UHF RFID antenna design: impedance-matching and size-reduction techniques," *IEEE Antennas Propag. Mag.,* vol. 50, no. 1, pp. 66–79, Mar. 2008.

[14] E. Perret, S. Tedjini, and R. S. Nair, "Design of antennas for UHF RFID tags," *Proc. IEEE*, vol. 100, no. 7, pp. 2330–2340, July 2012.

[15] T. Mäkinen and T. Kellomäki, "Body effects on thin single-layer slot, self-complementary, and wire antennas," *IEEE Trans. Antennas Propag.*, vol. 62, no. 1, pp. 385–392, Nov. 2013.

[16] T. Björninen, "Comparison of three body models of different complexities in modelling of equal-sized dipole and folded dipole wearable passive UHF RFID tags," *Appl. Computational Electromagn. Soc. J.*, vol. 33, no. 6, pp. 706–709, May. 2018.

[17] E. K. Kaivanto, M. Berg, E. Salonen, and P. de Maagt, "Wearable circularly polarized antenna for personal satellite communication and navigation," *IEEE Trans. Antennas Propag.*, vol. 59, no. 12, pp. 4490–4496, Dec. 2011.

[18] M. Joler and M. Boljkovac, "A sleeve-badge circularly polarized textile antenna," *IEEE Trans. Antennas Propag.*, vol. 66, no. 3, pp. 1576–1579, Mar. 2018.

[19] J. Li, Y. Jiang, and X. Zhao, "Circularly polarized wearable antenna based on NinjaFlex-embedded conductive fabric," *Intl. J. Antennas Propag.*, vol. 2019, article ID 3059480, 8 pages, Sep. 2019.

[20] C. W. Chiu and J. H. Hong, "Circularly polarized tag antenna on an AMC substrate for wearable UHF RFID applications," in *IEEE-APS Topical Conference on Antennas and Propagation in Wireless Communications*, Verona, Italaly, Sep. 2017, pp. 71–74.

[21] D. Le, L. Ukkonen, and T. Björninen, "Circularly polarized corner-truncated and slotted microstrip patch antenna on textile substrate for wearable passive UHF RFID tags," in *European Conference on Antennas and Propagation*, Copenhagen, Denmark, Mar. 2020, 5 pages.

[22] T. Björninen, L. Sydänheimo, and L. Ukkonen, "Development and validation of an equivalent circuit model for UHF RFID IC based on

wireless tag measurements," in *Antenna Measurement Techniques Association Symposium*, Bellevue, WA, USA, Oct. 2012, pp. 21–26.

[23] T. Ali and R. C. Biradar, "A miniaturized circularly polarized coaxial fed superstrate slot antenna for L-band application," *Internet Technol. Lett.*, vol. 6, no. 1, 7 pages, Nov. 2018.

[24] D. Le, Y. Kuang, L. Ukkonen, and T. Björninen, "Microstrip transmission line model fitting approach for characterization of textile materials as dielectrics and conductors for wearable electronics," *Intl. J. Numerical Modelling Electronic Netw. Dev. Fields*, vol. 32, no. 6, 10 pages, Feb. 2019.

[25] S. Gabriel, R. W. Lau, and C. Gabriel, "The dielectric properties of biological tissues: III. Parametric models for the dielectric spectrum of tissues," *Phys. Med. Biol.*, vol. 41, no. 11, pp. 2271–2293, Nov. 1996.

[26] IT'IS Foundation, Tissue Properties [Online]. Available: https://www.itis.ethz.ch/virtual-population/tissue-properties/downloads

[27] Thomas A. Milligan, Modern Antenna Design, 2nd ed., vol. 2. John-Wiley & Sons, Inc., pp. 18–24.

[28] Voyantic, Ltd., Espoo, Finland: http://www.voyantic.com/

[29] H. D. Chen, W. S. Chen, and S. H. Kuo, "CP RFID tag design for metal surface mount," in *Cross Strait Quad-Regional Radio Science and Wireless Technology Conference*, Harbin, China, July 2011, pp. 491–493.

[30] S. Ma, L. Ukkonen, L. Sydänheimo, and T. Björninen, "Dual-Layer circularly polarized split ring resonator inspired antenna for wearable UHF RFID tag," in *IEEE International Symposium on Antennas and Propagation*, Boston, MA, USA, July 2018, pp. 683–684.

[31] Y. Kuang, S. Ma, L. Ukkonen, J. Virkki, and T. Björninen, "Circularly polarized textile tag antenna for wearable passive UHF RFID systems", in *International Applied Computational Electromagnetics Society Symposium-China*, Beijing, China, July 2018, 2 pages.